# Quantification of the Gating Charge in $K^+$ and $Na^+$ Ion Channels by Use of eGFP Fluorescence

Dissertation

zur

Erlangung der naturwissenschaftlichen Doktorwürde
(Dr. sc. nat.)

vorgelegt der

Mathematisch–naturwissenschaftlichen Fakultät

der

Universität Zürich

von

Dominik Grögler

aus Deutschland

Promotionskomitee

Prof. Dr. Hans–Werner Fink (Vorsitz)
Prof. Dr. Klaus Greeff (Leitung der Dissertation)
Dr. Peter Robmann

Zürich, 2009

Gutachter

Dr. Thomas Zimmer
Universität Jena

# Zusammenfassung

Ionenkanäle sind lebensnotwendige Elemente beinahe jeglicher uns bekannten Lebensformen. Diese komplexen makromolekularen Proteine sind in die Zellmembran eingelagert und regulieren die Ionenleitfähigkeit der Membran durch das Öffnen und Schliessen einer Ionenpore, die durch mechanische, chemische oder elektrische Reize stimuliert werden kann.

In Nervenzellen generieren spannungsgesteuerte Ionenkanäle elektrische Signale und leiten diese von einer Zelle zur nächsten weiter. Einige Aminosäurenreste der Kanalproteine sind elektrisch geladen und können sich aufgrund von Änderungen der Membranspannung durch diese hindurch bewegen. Diese Ladungen werden *gating Ladungen* genannt. Die Bewegung der gating Ladungen führt zu einer Veränderung der dreidimensionalen Proteinstruktur, die das Öffnen und Schliessen der Pore nach sich zieht. Das Wechselspiel zwischen Natrium– und Kalium–selektiven Kanälen ($Na^+$ und $K^+$ Kanäle) führt in Nervenzellen das sogenannte Aktionspotential herbei. Die Wahrscheinlichkeit, mit welcher die Kanäle ihre Ionenpore öffnen, ist in einem so hohen Ausmass spannungsabhängig, dass eine Spannungsveränderung von nur 10 mV diese Wahrscheinlichkeit um das hundertfünfzigfache erhöhen kann.

Die Größe der gating Ladung von *Shaker* $K^+$ Kanälen wird in der Fachliteratur konsistent und wiederholt auf 13 Elementarladungen festgelegt. Im Gegensatz dazu schwanken die angegebenen Werte für $Na^+$ Kanäle zwischen 4 und 16 Elementarladungen. Die Ursache des gating Stroms liegt in der Bewegung der gating Ladungen im elektrischen Feld entlang der Ionenpore. Ein einzelner Ionenkanal verursacht gating Ströme im pA–Bereich, und ist deshalb zu klein, um in einem komplexen biologischen System nachgewiesen werden zu können. In der vorliegenden Studie wurden die gating Ladungen von $K^+$ und $Na^+$ Ionenkanälen mittels der kontrollierten elektrischen Stimulierung von Zellen bestimmt, in deren Membran sich $10^8$–$10^{10}$ Kanalproteine befanden. Die Anzahl der Kanäle wurde dabei mit einer neuartigen Methode abgeschätzt, die auf Fluoreszenzmessungen genetisch veränderter Ionenkanäle beruht, die mit *grün fluoreszierenden Proteinen* (eGFP) markiert wurden. Ausgehend von der bekannten Größe der gating Ladung von $K^+$ Kanälen konnte der entsprechende Wert für den rBIIA $Na^+$ Kanal auf $5.2 \pm 0.3$ Elementarladungen festgesetzt werden.

Die vorliegende Arbeit besteht aus drei Teilen: 1) ein einleitendes Kapitel über spannungsgesteuerte Ionenkanäle, 2) ein experimenteller Abschnitt über die Bestimmung der gating Ladung von *Shaker* $K^+$ und rBIIA $Na^+$ Kanälen, sowie ein Vergleich beider gating Ladungen, und 3) ein Kapitel über die Verwendung optischer Fasern, um fluoreszente Moleküle lokal anzuregen und deren Emissionslicht zu detektieren.

Der einleitende Teil bietet einen Überblick über die biologische Relevanz, die Funktion sowie die molekulare Struktur spannungsgesteuerter Ionenkanäle in lebenden Organismen. Das Verhältnis zwischen Struktur und Funktion dieser Proteine wird im Rahmen einer Diskussion der wichtigsten Publikationen der letzten zwanzig Jahre behandelt. In der Absicht die notwendige Wissensgrundlage in Hinblick auf das zweite Kapitel zu schaffen, konzentriert sich dieser Abschnitt vorrangig auf den gating Prozeß und dessen Implikationen in Bezug auf die Struktur von Ionenkanälen.

Im zweiten Kapitel werden die Experimente vorgestellt, die sich mit der Quantifizierung der gating Ladung von *Shaker* $K^+$ und rBIIA $Na^+$ Kanälen auseinander setzen. Die gating Ladung einer grossen Anzahl von $K^+$ und $Na^+$ Kanälen wurde bestimmt und die Anzahl der Kanalproteine mit Hilfe von Intensitätsmessungen der Fluoreszenzemission abgeschätzt. Die hier besprochenen Experimente sind Gegenstand der Publikation *More gating charges are needed to open a* Shaker *$K^+$ channel than are needed to open a rBIIA $Na^+$ channel*, Biophysical Journal, 95(3):1165–1175, 2008.

Die hohe Eigenfluoreszenz der Zellen hat die im zweiten Kapitel vorgestellten Fluoreszenzmessungen stark beeinträchtigt. Mit dem Ziel, das Anregungsvolumen – und somit auch das Eigenfluoreszenzsignal – einzuschränken, wurde eine Apparatur entwickelt, welche optische Fasern verwendet, um fluoreszente Moleküle sowohl zur Fluoreszenz anzuregen, als auch deren Fluoreszenzemission zu detektieren. Im dritten Kapitel wird dieses faseroptische System sowie einige vorbereitende Experimente in Bezug auf die Fluoreszenzeigenschaften von grün fluoreszierenden Proteinen vorgestellt.

# Abstract

Ion channels are vital for nearly every form of life as we know it. Embedded in the cellular membrane, these complex macromolecular proteins control ionic conductivity by opening or closing an ionic pore upon mechanical, chemical or electrical stimuli.

In nerve cells, voltage gated ion channels generate and mediate the transduction of electrical signals from one cell to the next. Some residues of the channel structure are electrically charged and can move through the membrane in response to changes in the transmembrane voltage. These charges are called *gating charges*. As a consequence of their movement, the three–dimensional conformation of the protein changes and triggers the opening or closing of the ionic pore. The interplay of sodium– and potassium–selective ion channels ($Na^+$ and $K^+$ channels) in nerve cells gives rise to the so–called action potential. The voltage dependence of the probability of channels to open their ionic pore is so steep that a change of the transmembrane voltage of as little as 10 mV can increase this probability by a factor of 150.

For *Shaker* type $K^+$ channels, the gating charge has consistently been reported to be of the size of 13 elementary charges. However, for $Na^+$ channels corresponding findings vary between 4 and 16 elementary charges. The gating current is the current due to the movement of the gating charges in the electric field along the ionic pore. For a single voltage gated ion channel the gating current is in the order of pA and therefore below detection threshold in complex biological systems. In the present study, the gating charges of $K^+$ and $Na^+$ ion channels have been determined by the controlled electrical stimulation of cells containing $\simeq 10^8$–$10^{10}$ channel proteins. The number of channels was quantified by a novel approach based on fluorescence intensity measurements of genetically modified ion channels labeled with *enhanced green fluorescent proteins* (eGFP). On the basis of the known value for the gating charge of the $K^+$ channel, it has been possible to determine that the size of the gating charge in the rBIIA $Na^+$ channel is of $5.2 \pm 0.3$ elementary charges.

The present thesis is structured in three parts: 1) An introductory chapter on voltage gated ion channels, 2) an experimental part dealing with the determination of the gating charge of the *Shaker* $K^+$ channel and of the rBIIA $Na^+$ channel, including a comparison of both gating charges and 3) a chapter on the use of optical fibers to locally excite fluorescent proteins and detect their fluorescence emission light.

The introductory part is intended for the reader to get a brief overview about the biological significance of voltage gated ion channels for living organisms, about their function and their molecular structure. The relation between the structure and the function of voltage gated ion channels is discussed in the context of the most important publications of the last 20 years. In order to provide the necessary background for the second chapter, the primary focus was laid on the gating process of voltage gated ion channels and its structural implications.

The second chapter deals with experiments on the quantification of the gating charge in *Shaker* $K^+$ channels and rBIIA $Na^+$ channels. The gating charge of a large number of $K^+$ and $Na^+$ channels was determined and the number of channels was estimated by fluorescence intensity measurements. The experiments presented in this chapter have led to the publication *More gating charges are needed to open a* Shaker *$K^+$ channel than are needed to open a rBIIA $Na^+$ channel*, Biophysical Journal, 95(3):1165–1175, 2008.

The strong autofluorescence of the specimen handicapped the fluorescence intensity measurements in the preceding experiments. To limit the excitation volume – and thereby reduce the autofluorescence signal – a system was developed that uses optical fibers both to excite fluorophores and to detect their fluorescence emission. In the third chapter this fiber optical system is introduced and preliminary experiments on the fluorescence properties of enhanced green fluorescent proteins are presented.

# Contents

# List of Figures

# 1 Introduction on voltage gated ion channels

The idea that electrical phenomena play a crucial role in living organisms is more than 200 years old. The debate over *"animal electricity"* was already widely discussed and speculated about when in 1771 Luigi Galvani made his famous observation on frog legs, published in 1791 [1]:

> *"While one of those who were assisting me touched lightly, and by chance, the point of his scalpel to the internal crural nerves of the frog, suddenly all the muscles of its limbs were seen to be so contracted that they seemed to have fallen into tonic convulsions."*

Galvani was not the first one to discover that living or dead animals could be stimulated electrically to contract their muscles, but he was first in systematically designing experiments and analyzing their results [2]. However, it was not until the 1950's that Alan Hodgkin and Andrew Huxley presented a mathematical model describing the exchange of charged particles through the cellular membrane [3]. And yet another 20 years passed until the modern view on ion channels as membrane bound proteins emerged.

## Biological Function

Ion channels are complex macromolecules with a length of $\simeq 500-2000$ amino acids and a weight of $\simeq 50-220\,\mathrm{kD}$. The fundamental role of ion channels in living organisms is the control of ion flow through the cellular membrane. By opening or closing a pore – in response to changes in temperature or to electrical, chemical or mechanical stimuli – they regulate the conductivity for certain ions with astonishingly high selectivity. The permeability of $Na^+$ channels to $Na^+$ ions is $\simeq 30$ times larger than for $K^+$ ions while the channel pore is virtually impermeable for $Ca^{2+}$ ions. The permeability of $K^+$ channels to $K^+$ ions is even $\simeq 100$ times larger than its permeability to $Na^+$ ions. Ion channels are located in the membrane of nerve and muscle cells, both before and after the synaptic gap. Opening and closing

can be performed in times as short as milliseconds and at rates up to kilohertz. Depending on the geometry and the composition of the cell, the speed of the generated signals is in the range of 0.5 – 100 m/s. Even though there is a wide variety of channel proteins, they all show a remarkable similarity throughout the different species. For example the gene of the *Shaker* $K^+$ channel of the fruit fly *Drosophila melanogaster*[1] has been found – with only slight variations – in the genome of plants, amphibians and humans.

The most prominent manifestation of ion channels is the generation of the so–called action potential, which is a consequence of the interplay between $K^+$ channels, which are selective only for $K^+$ ions, and $Na^+$ channels, which are selective only for $Na^+$ ions (see figure 1.1). In a simple approach, an axon (or nerve cell) may be seen as a cylinder whose surface consists of an electrically insulating lipid bilayer of a few nm thickness into which the channel proteins are embedded. The interior and exterior are filled with aqueous solution, which reveals a high concentration of $K^+$ ions inside and a high concentration of $Na^+$ ions outside of the cell (see table 1.1, page 21 for typical ion concentrations). The typical channel density on the cell surface reaches about 10 to 200 channels/$\mu m^2$. Both $K^+$ and $Na^+$ channels are *voltage* gated ion channels: they change their three–dimensional conformation in response to changes of the electric field they are exposed to. This conformational change can lead to the opening or closing of the ion pore.

Preceding an action potential, all channels are in their closed or non–conducting conformation (referred to as the *resting state*). In the resting state, all $Na^+$ channels are closed while a few $K^+$ channels are conductive, which leads to a potential difference between the inside and the outside of the cell in the order of $\simeq -80$ mV. If at some point the cell is depolarized[2] to a potential difference of $\simeq -50$ mV (see roman I in figure 1.1), some of the $Na^+$ channels – whose response is faster than that of $K^+$ channels – will open their pore and $Na^+$ ions will flow from the outside to the inside of the cell, driven by the ionic concentration gradient and the electric force. This flow of positive charges raises the potential difference

[1] The *Shaker* $K^+$ channel is a mutation of a channel found in the fruit fly *Drosophila melanogaster*. It is widely used in biological research, and is one of the best known channel proteins. It was first sequenced and cloned by Tempel et al. in 1987 [4]. This mutated $K^+$ channel can not repolarize the membrane as fast as the original channel can during an action potential (see next paragraph and figure 1.1), which triggers the release of vast amounts of neurotransmitters in the post–synaptic gap. As a consequence, the fly constantly shakes its legs when anesthetized with ether.

[2] In electrophysiology, it has become common practice to call a cell *polarized* if its transmembrane voltage is near the resting state (at $\simeq -80$ mV), and *depolarized* if the transmembrane voltage is higher (more positive) than at the resting state. At voltages below the resting state, the cell is said to be *hyperpolarized*.

Accordingly, pulses that increase the transmembrane voltage are called *depolarizing pulses*, pulses that reestablish the resting state are called *repolarizing pulses* and pulses lowering the voltage beyond the resting state are called *hyperpolarizing pulses*.

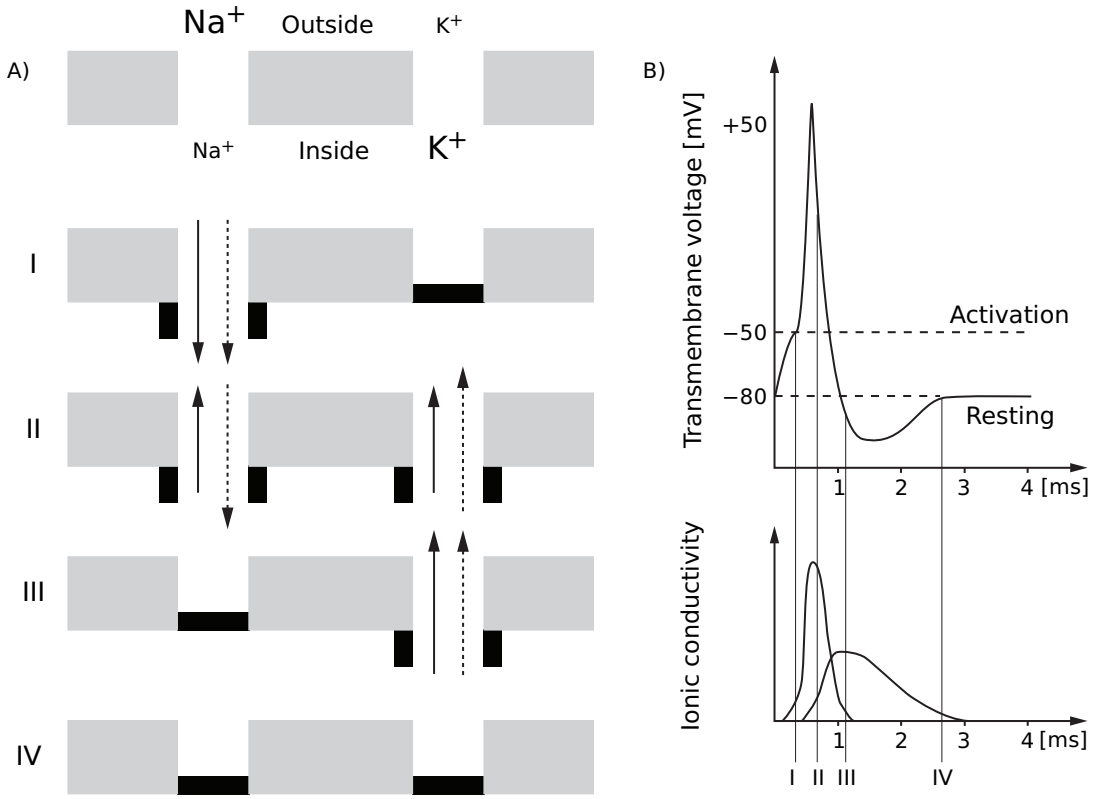


Figure 1.1: Generation of an action potential. A) Schematic representation of a $K^+$ and a $Na^+$ channel. The grey area is the cellular membrane as seen from the side. The two white spaces are a $Na^+$ and a $K^+$ channel which can open or close their ion pore (black bars). Solid arrows depict electrical forces that act upon the positively charged ions and dashed arrows depict diffusional forces. The concentration of $Na^+$ ions is higher outside and the concentration of $K^+$ ions is higher on the inside of the cell. B) The action potential and the ionic conductivity of $K^+$ and $Na^+$ channels during an action potential.
The sequential steps of the channels indicated with roman numbers in figure A correspond to the times indicated with roman numbers in figure B. It should be noted that in the resting state a few $K^+$ channels are still open to maintain the resting potential diefference.

across the membrane even more, increases the probability of neighboring $Na^+$ channels to also open their pore. As a consequence, the amount of positive ions flowing to the inside of the cell rises as well. As the inside of the cell gets more and more positive, the flow of ions will diminish and eventually stop when the electric forces compensate the diffusional forces. The absolute concentrations of $Na^+$ and $K^+$ ions are barely altered during the action potential (depending on the size of the cell by as little as 0.001%), therefore the diffusional force stays nearly constant during an action potential. At this point, $K^+$ channels will begin to open their pore (see roman II in figure 1.1). Because the concentration of $K^+$ ions is larger inside compared to the outside of the cell, positive $K^+$ ions, driven by the electric and diffusional forces, now start to move towards the outside, decreasing the potential difference across the membrane. Now the membrane becomes non–conductive to $Na^+$ ions:

the $Na^+$ channels change to an *inactivated* state[3]. The $K^+$ channels remain open for a few more ms, which leads to an undershoot (for a short time the potential difference reaches values even lower than the resting potential difference) before the resting state is reinstated (see roman III in figure 1.1). As soon as inactivation is removed, the $Na^+$ channels close their pore and are ready to open again in response to the next depolarization of the cell (see roman IV in figure 1.1).

In this manner, the action potential is generated and travels along the axon, eventually reaching the synaptic terminal of the cell, where the rise of the potential difference triggers the release of neurotransmitters, or ligands, which diffuse through the 20–40 nm wide synaptic gap to the post–synaptic axon. Here they can bind to ligand gated ion channels, that respond by opening their pore. Ions that now start to flow activate the surrounding voltage gated channels and another action potential is generated. Finally, the signal may reach muscle cells which generate another action potential that triggers the contraction of the muscle.

In summary, voltage gated ion channels are necessary to generate specific electrical signals and transduce them along the neuron. To bridge the electrically insulating barrier between one neuron and the next, ligand gated channels come into play. While the former opens and closes via electrical stimuli, the latter's opening and closing is triggered by the binding of neurotransmitters. In both channel types, ions flow along their concentration gradients from the inside to the outside of the cell or vice versa. Only a very small relative amount of ions actually flows during the action potential. Still, at some point, ions have to be actively transported from one side of the cell to the other in order to maintain the ionic concentration differences. This function is carried out by so called ion–pumps[4].

[3] The inactivation gate blocks the pore shortly after it has opened. In this state the channel in non–conductive, and even an additional depolarizing pulse does not increase its ionic conductivity. For the channel to be able to open its pore again, it first has to be inactivated. Inactivation is a relatively slow process which occurs in a time frame of $\simeq 10$ ms. The channel can also be inactivated by hyperpolarizing the cell.

[4] Ion pumps are specialized membrane proteins that bind to ions with high affinity. By conformational changes, they translocate ions through the cellular membrane from one side of the cell to the other. For this reason they are also called *transporters*.

## 1.1 The structure of $K^+$ and $Na^+$ channels

Although a huge variety of $K^+$ and $Na^+$ channels exists, the majority of them show a high degree of similarity. This section will focus on the channel structure of the *Shaker* type $K^+$ channel and on eukaryotic $Na^+$ channels.

### 1.1.1 The $K^+$ channel

The $K^+$ channel is a tetramer of four identical subunits. Each of the four subunits consists of six transmembrane spanning segments S1–S6 (see figure 1.2 for a schematic of a $K^+$ channel subunit and figure 1.6 for the crystal structure of a $K^+$ channel). All segments are $\alpha$– helices[5] that are connected by intra– and extracellular loops. Segments S1–S4 are electrically charged and constitute the so–called *voltage sensing domain* (VSD). This part of the protein moves in response to changes of the transmembrane voltage and triggers the opening and closing of the ionic pore. Segments S3 and S4 play the most important role in voltage sensing, because they carry most of the charge (see section 1.3.1 for a more detailed discussion about voltage sensing). The highest charge density is found on the fourth segment S4: here, every third residue is either one of the amino acids arginine or lysine, which are both positively charged. For this reason, S4 is sometimes called the *voltage sensor*. The pore itself is formed by the segments S5, S6 and the extracellular loop that connects the two segments. The four subunits form a highly symmetrical structure with the pore at the center and the voltage sensing domain at the four corners around the pore (see figure 1.6, page 26).

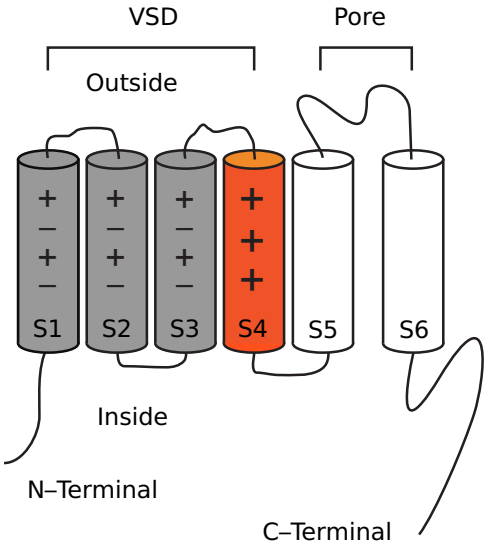


Figure 1.2: The $K^+$ channel structure. Only one of the four identical subunits of a $K^+$ channel is shown. Each subunit consists of six transmembrane spanning $\alpha$–helical segments S1–S6. Segments S1–S4 constitute the voltage sensing domain (VSD); in red the voltage sensor S4; in white S5 and S6 which constitute the pore domain. The charge symbols reflect the approximate distribution of charges on the VSD.

[5]The $\alpha$–helix is a very common motif of the secondary structure of proteins. It is a right– or left handed coil of amino acids with about 3.6 amino acids per turn. Each turn corresponds to a length of $\simeq 5.4$Å along the axis of the helix. See figure 1.5, page 24 for a schematic of an $\alpha$–helix.

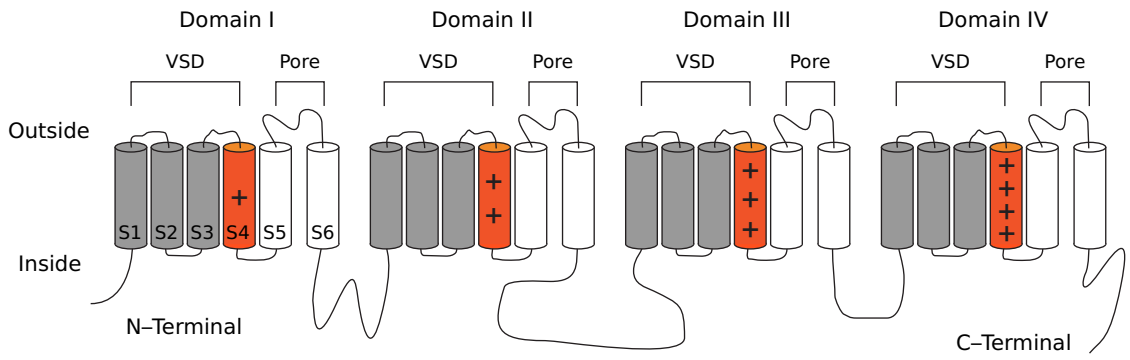


Figure 1.3: The $Na^+$ channel structure. The four covalently bound domains of the $Na^+$ channel, each consisting of six $\alpha$–helical membrane spanning segments S1–S6 (only indicated for the first domain). Segments S1–S4 constitute the voltage sensing domain (VSD); in red the voltage sensor S4; in white S5 and S6 which constitute the pore domain. The charge symbols reflect the approximate distribution of charges on the VSD.

### 1.1.2 The $Na^+$ channel

The $Na^+$ channel consists of four homologous domains DI–DIV which are covalently bound to each other (see figure 1.3). Each of the four domains consists of six transmembrane spanning segments S1–S6 of $\alpha$–helical structure. As in the $K^+$ channel, segments S1–S4 form the voltage sensing domain with S4 being of primary importance: in $Na^+$ channels too, every third amino acid of the S4 sequence is a positively charged arginine or lysine residue. The hydrophobic part between S5 and S6 constitutes the ion pore. The inactivation gate, that blocks the pore a few ms after the channel has opened its pore, and inhibits the channel from opening its pore again before it first has inactivated, is formed by the intracellular linker between domains III and IV.

## 1.2 Ionic conductivity

The ability of voltage gated ion channels to change their ionic conductivity in response to changes in the transmembrane voltage allows them to control the flow of electrical currents across the cellular membrane. Because the ionic concentration of ions is different inside and outside the cell, a net current of ions will flow until the electrical forces counterbalance the diffusional forces. The potential difference that will be reached in thermodynamic equilibrium is somewhat unprecisely called the *resting* or *Nernst potential*. Even though the Nernst equation is a simplifying model of the diffusion processes in biological membranes, it is nevertheless a useful tool to describe the resting state of a nerve cell.

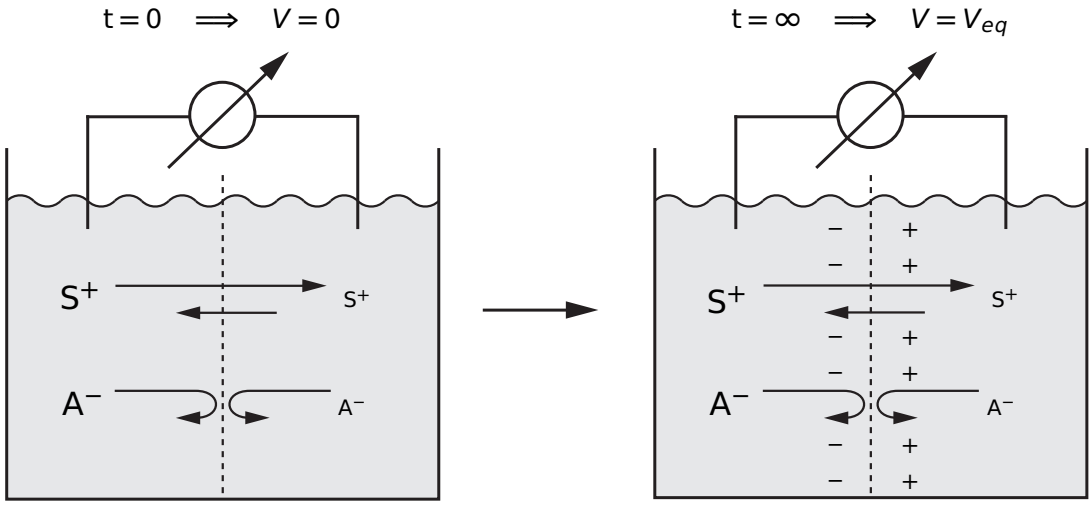


Figure 1.4: The diffusion potential. A reservoir which is separated into two compartments by a semipermeable membrane is filled with water. The membrane is permeable for positively charged $S^+$ cations but impermeable for the negatively charged $A^-$ anions of a salt SA. An electrometer measures the potential difference between the two compartments. At time $t = 0$, when a high concentration of the salt SA is poured into the left compartment and a low concentration of SA is poured into the right compartment, the potential difference between the two compartments is 0 V. Then the positively charged cations start to diffuse to the right side along the concentration gradient. When the system has reached thermodynamic equilibrium at time $t = \infty$, the potential difference between the two compartments reaches the equilibrium or resting potential difference $V_{eq}$ (also referred to as the *Nernst potential*).

### 1.2.1 The Nernst equation

For a system in thermodynamic equilibrium with $j$ possible energy states $u_j$, the Maxwell–Boltzmann probability distribution describes the probability $p_j$ to find a particle with the energy $u_j$ in the state $j$:

$$p_j = \frac{1}{Z} \exp\left[-\frac{u_j}{k_B T}\right] \qquad \text{with } Z := \sum_i e^{\frac{u_i}{k_B T}} \tag{1.1}$$

where $k_B$ is the Boltzmann constant, $T$ the absolute temperature and $Z$ the partition function. Since ion channels are highly selective for specific ions, a cellular membrane with incorporated ion channels can be looked at as a semipermeable membrane (assuming that the ion channels are in their open configuration). If the two sides the ion can be located in are referred to as the possible states the ion can occupy, the system channel–membrane can be described as a two–state system. By convention, a particle inside the cell is said to occupy state one and a particle outside the cell is said to occupy state two. With these presumptions and the Maxwell–Boltzmann equation 1.1, the ratio of the probabilities for an

ion to be inside or outside the cell is given by:

$$\frac{p_{out}}{p_{in}} = \exp\left[-\frac{u_{out} - u_{in}}{k_B T}\right] \tag{1.2}$$

If $c_{in}$ and $c_{out}$ are the concentrations of particles with energies $u_{in}$ and $u_{out}$, the probability to find a particle in a particular state is directly proportional to the concentration of particles in this state. If the particle energies are replaced by their respective molar energies, equation 1.2 can be rewritten:

$$\frac{c_{out}}{c_{in}} = \exp\left[-\frac{u_{out} - u_{in}}{N_A k_B T}\right]$$

where $N_A$ is Avogadro's number. It directly follows:

$$u_{in} - u_{out} = N_A k_B T \ln\frac{c_{out}}{c_{in}} \tag{1.3}$$

If $E_{in}$ and $E_{out}$ are the respective electric potentials inside and outside the cell, the molar energy difference can also be formulated as:

$$u_{in} - u_{out} = z_i N_A e\,(E_{in} - E_{out})$$

where $z_i$ is the valence of the ion and $e$ the elementary charge. Together with equation 1.3, this leads to the potential difference across the cellular membrane in thermodynamic equilibrium:

$$V_{eq} = E_{in} - E_{out} = \frac{k_B T}{z_i e}\ln\frac{c_{out}}{c_{in}} \tag{1.4}$$

Equation 1.4 is called the *Nernst equation*. If the ion channels are in their open configuration, the transmembrane voltage is a linear function of temperature and depends logarithmically on the concentration ratio of the ions. Such a system will approach the equilibrium potential difference and the ionic current will approach zero. If on the other hand the voltage across the membrane is held at a constant level, then a constant current will flow as long as the concentration difference between the two sides of the membrane can be maintained. This relation is of great importance in voltage clamp experiments that will be presented in section 2.2.1. Table 1.1 lists equilibrium potential differences of $Na^+$ and $K^+$ ions in mammalian skeletal muscle cells.

| Ion | Concentration [mM] | | $\frac{c_{out}}{c_{in}}$ | $V_{eq}$ [mV] |
|---|---|---|---|---|
| | Extracellular | Intracellular | | |
| $Na^+$ | 145 | 12 | 12 | +67 |
| $K^+$ | 4 | 155 | 0.026 | −98 |

Table 1.1: Ion concentrations and resting potentials of $Na^+$ and $K^+$ ions in mammalian skeletal muscle cells according to [5]. $c_{in}$ and $c_{out}$ are the ion concentrations inside and outside the cell. $V_{eq}$ is the potential difference across the membrane in thermodynamic equilibrium as calculated with equation 1.4 at 37 °C.

However, this model is correct only if the respective solution contains just one type of ion. The Goldman–Hodgkin–Katz equation provides a more general description of the ionic flow through the pores of ion channels. It makes use of the constant–field theory developed by David Goldman, Alan Hodgkin and Bernard Katz in the 1940's.

### 1.2.2 The Goldman–Hodgkin–Katz equation

To find a more general description of the potential difference across the membrane of a cell in thermodynamic equilibrium that allows for the presence of more than one type of ion, the ionic flux can be described by the Nernst–Planck equation. In the following, it is assumed that the pore of length $L$ spans along the $x$–axis which runs from the inside to the outside of the cell perpendicular to the membrane surface. In that case the ionic flux $J_i$ is equal to:

$$j_i = D_i \left[ -\frac{\mathrm{d}c_i}{\mathrm{d}x} + z_i \mu E_m c_i \right] \qquad \text{with } \mu := \frac{N_A e}{RT} \tag{1.5}$$

where $D_i$ is the diffusion coefficient of the ion, $c_i$ the molar concentration of the ion and $E_m$ the electric field along the membrane. The left part of equation 1.5 is Fick's law of diffusion according to which the ionic flux is dependent on the change of ion concentration, the right part is the flux due to the electric forces which is linearly dependent on the electric field. Assuming that the electric field along the ionic pore is constant, the electric field $E_m$ is equal to $E_m = V_m/L$, and rearrangement, variable separation and integration of equation 1.5 leads to:

$$L = \int_0^L \mathrm{d}x = \int_{c_{in}}^{c_{out}} \frac{1}{-\frac{j_i}{D_i} + \frac{z_i \mu V_m}{L} c_i} \mathrm{d}c_i = \frac{L}{z_i \mu V_m} \ln\left( -\frac{j_i}{D_i} + \frac{z_i \mu V_m}{L} c_i \right) \Bigg|_{c_{in}}^{c_{out}} \tag{1.6}$$

where $c_{in}$ and $c_{out}$ are the ionic concentrations inside the cell at $x = 0$ and outside the cell at $x = L$. Expansion and rearrangement of equation 1.6 yields:

$$z_i \mu V_m = \ln\left(\frac{D_i z_i \mu V_m c_{out} - j_i L}{D_i z_i \mu V_m c_{in} - j_i L}\right)$$

This equation can easily be reordered and leads to the Goldman–Hodgkin–Katz current equation:

$$j_i = \frac{D_i z_i \mu V_m}{L} \; \frac{c_{in} - c_{out} e^{z_i \mu V_m}}{1 - e^{z_i \mu V_m}}$$

In thermodynamic equilibrium no net current is flowing. In this case, the sum of all ionic currents has to be zero. Therefore, if $K^+$ and $Na^+$ ions only are present in the intra– and extracellular volume it must hold true:

$$0 = j_K + j_{Na} = \frac{\mu V_m}{L} \; \frac{D_K [K]_{in} - D_K [K]_{out} e^{\mu V_m} + D_{Na} [Na]_{in} - D_{Na} [Na]_{out} e^{\mu V_m}}{1 - e^{\mu V_m}} \tag{1.7}$$

where $[K]_{in,out}$ and $[Na]_{in,out}$ are the concentrations of $K^+$ and $Na^+$ ions at the inside and at the outside of the cell, respectively. Equation 1.7 can be satisfied if its numerator becomes zero:

$$D_K [K]_{in} - D_K [K]_{out} e^{\mu V_m} + D_{Na} [Na]_{in} - D_{Na} [Na]_{out} e^{\mu V_m} = 0$$

and rearranging this term leads to the potential difference across the membrane in thermodynamic equilibrium:

$$V_m = \frac{R T}{N_A e} \; \ln\left(\frac{D_K [K]_{in} + D_{Na} [Na]_{in}}{D_K [K]_{out} + D_{Na} [Na]_{out}}\right) \tag{1.8}$$

Two assumptions have been made to derive this equation: 1) The flux of ions is linearly dependent on the concentration gradient without ever saturating – in other words, the ions in the pore do not interact with each other –, and 2) the electric field along the pore of an ion channel is constant. Strictly speaking, neither assumption is correct. However, equation 1.8 is in very good agreement with the observation.

It should be noted that in the resting state of a nerve cell, the potential difference is $\simeq -80\,\mathrm{mV}$ which is close to the equilibrium potential difference as determined by the Nernst equation 1.4 for $K^+$ ions. This is because in the resting state, a few $K^+$ channels are open while all $Na^+$ channels are closed.

## 1.3 Gating of ion channels

Even though in 1952 the knowledge about the molecular structure of the cellular membrane was very limited, and ion channels as separate entities were not discovered yet, Hodgkin and Huxley already formulated the key concept that explains the steep voltage dependence of ionic conductivity in a nerve cell [3]:

> *"A different form of hypothesis is to suppose that sodium movement depends on the distribution of charged particles which do not act as carriers in the usual sense, but which allow sodium to pass through the membrane when they occupy particular sites in the membrane."*

The *charged particles* are what today is referred to as *gating charges*: electrically charged residues of the channel protein which move in response to changes of the transmembrane voltage. In the subsequent six decades of research and thanks to an extraordinary technological progress, our knowledge about ion channels has tremendously expanded.

Two outstanding achievements with respect to the gating process in ion channels were the direct measurement of the gating charge by Armstrong and Bezanilla in 1973 [6] and the measurement of ionic currents through single channels by Neher and Sakmann in 1976 [7]. In the 1980's, the discovery of the $Na^+$ channel protein by Agnew et al. [8] and Beneski et al. [9] and the first expression of functional sodium channels from cloned cDNA by Noda and colleagues [10] paved the way for a molecular understanding of the functioning of ion channels. Enormous advancements in the field of molecular biology and genetical engineering beginning in the 1970's led to the determination of the primary structure[6] of many channel proteins, and later on to the determination of the secondary structure by analysis of X–ray diffraction patterns of crystallized proteins.

All of these findings and developments significantly contributed to our knowledge about the molecular structure of ion channel proteins as well as the origin of their unique and vital ability to mediate the generation and transduction of nerve signals. In the last 20 years, the ability to mutate channel proteins at arbitrary positions and the availability of X–ray structures of channel proteins have led to a vast amount of publications and to ever more

[6] The primary structure of a protein is its sequence of amino acids. The sequences fold to structures such as $\alpha$–helices or $\beta$–sheets which are found in many different proteins. This is called the *secondary structure*. The *tertiary structure* describes how the secondary structures, which are loosely attached to each other by random coils, arrange themselves relatively to each other. Changes of the tertiary structure are referred to as *conformational changes*.

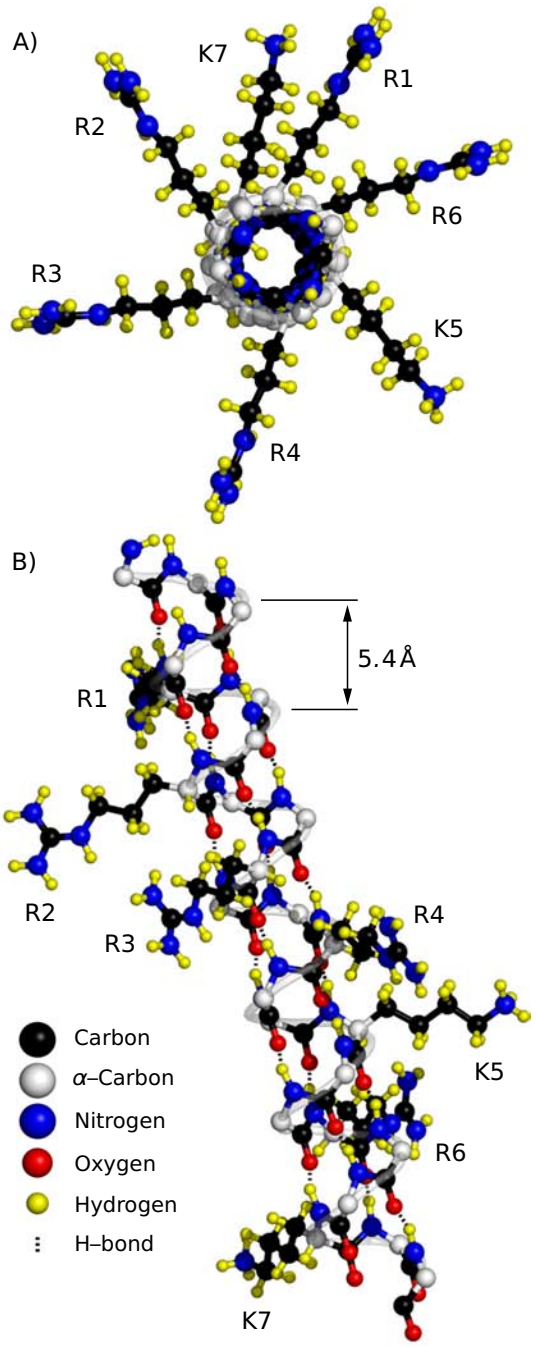


Figure 1.5: $\alpha$–helix of the voltage sensing segment S4 of a *Shaker* $K^+$ channel. A) Top view. B) Side view.
Every third amino acid residue is shown. R1–R4 and R6 are positively charged arginines, K5 and K7 are lysine residues which are also positively charged. The backbone is represented by the coil in white. The omitted residues are electrically neutral.

detailed information about the structure and function of voltage gated ion channels. The next section will focus primarily on $K^+$ channels as they are the ones most often studied.

### 1.3.1 Molecular basis of gating

Direct evidence that the fourth transmembrane spanning segment S4 of an ion channel plays an important role in gating came from the first cloning of an electric eel $Na^+$ channel in 1984 by Noda and colleagues [11]. The sequence revealed that the positively charged amino acids arginine and lysine are located primarily on S4 and to a lesser extent on S1–S3, while the rest of the channel consists of uncharged amino acids (see figures 1.2, 1.3 and 1.5). Every third position in S4 is occupied by either arginine or lysine, separated by electrically neutral amino acids. This structure (and even the three–dimensional orientation of the protein in the membrane) of the fourth segment of the protein is highly conserved: differences between bacterial and mammalian channels a remarkably small[7].

Yang and colleagues exchanged an arginine of a skeletal muscle $Na^+$ channel on segment S4 with an uncharged cysteine residue [12]. The original arginine was lo-

[7]This observation brings further evidence to the evolutionary theory of the common ancestry of the different species.

cated on the S4 segment close to the extracellular volume. Methanethiolsulfonate reagents have a high cysteine affinity and change the channel kinetics upon binding. This mutation was used to test whether or not the changed position of the arginine was accessible from the outside of the cell. Yang et al. found a strong voltage dependence of accessibility which increased with increasing transmembrane voltages. This indicates that segment S4 moves outward during activation. Mannuzzu et al. performed a similar study on the *Shaker* $K^+$ channel and came to similar conclusions [13].

These studies show that the outermost section of S4 changes its position when the channel activates. Larsson and colleagues expanded the aforementioned method in two respects [14]: 1) they tested a whole range of channel mutations, each having the cysteine at a different position, and 2) they tested internal as well as external accessibility of the cysteine. On the basis of a detailed comparison of all the channel constructs, they concluded that a part of S4 is buried in the membrane when the channel is closed. The segment then changes its position in such way that both ends stick out of the membrane when the channel is open. It has to be pointed out however, that the alteration of charged residues in the channel protein may significantly change the three–dimensional conformation of the protein, and that the observed positions of S4 during gating might not reflect the ones of the original channel protein.

In 1952, Hodgkin and Huxley published the first estimation of the size of the gating charge [3]. They proposed that 4–6 charges move fully across the membrane to open a $Na^+$ channel. A detailed discussion about the quantification of the gating charge will follow in the second chapter. By now it is well established that segment S4 is the primary location of the gating charge and that it moves in correspondence to changes in transmembrane voltage (see for example [12–14, 16–20]).

The first X–ray structure of a bacterial $K^+$ channel by Doyle and colleagues in 1998 [21], of the KvAP $K^+$ channel from the bacterium *Aeropyrum pernix* by Jiang and colleagues in 2003 [19, 22] and of a mammalian *Shaker* family $K^+$ channel by Long and colleagues in 2005 [23] have dramatically changed the way we see ion channels: indeed, for the first time, three–dimensional representations of channel proteins were available and gave rise to new speculations about their functioning. The two most discussed and rivaling models of channel gating are the *paddle model* and the *helical screw model*.

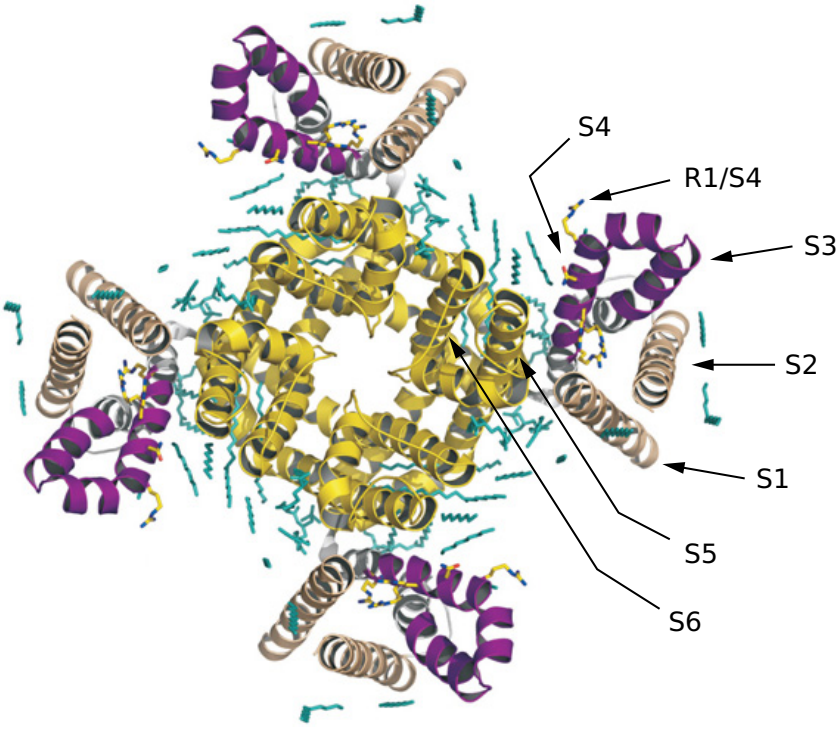


Figure 1.6: Crystal structure of a *Shaker* family $K^+$ channel as seen from the extracellular side [15] (Protein Data Bank entry: 2r9r). The spiral–like shapes represent the $\alpha$–helical structure of the segments S1–S6. In the middle of the structure is the ion pore consisting of segments S5 and S6 of each subunit. R1/S4 denotes the outer most arginine residue of segment S4.

### 1.3.2 The helical screw model

In the helical screw model, S4 is tilted with respect to the plane of the membrane and is in direct contact with the protein environment (see figure 1.7, A). When the channel switches from the closed to the open state, S4 moves by a length of $\simeq 13$ Å towards the outside of the membrane. The position of S4 is thought to be defined by the interaction between the positively charged residues in S4 and negatively charged regions of the rest of the protein. Based on these assumptions, the movement is thought to occur in steps where in each step one arginine residue of S4 moves to the position of the previous one. Because S4 is an $\alpha$–helix, S4 rotates around its axis while moving (see figure 1.5).

When Tombola and colleagues changed the first arginine (R1) of S4 of the *Shaker* $K^+$ channel to the smaller, uncharged, hydrophobic amino acid cysteine (R1C), they saw that the ionic conduction in the resting state increased when compared to the normal channel [24, 25]. Because the channels are closed in the resting state, another pathway for ionic

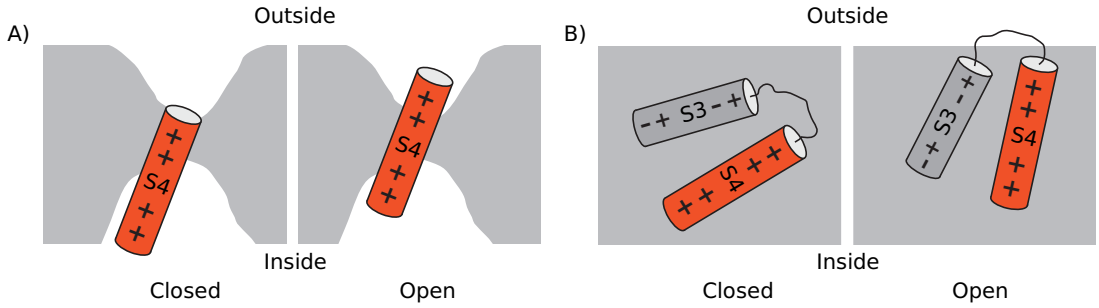


Figure 1.7: The paddle and the helical screw models of gating. The position of S4 in the closed and open states of the channel are indicated. Note that the ionic pore is not shown. The grey area denotes lipid. A) The helical screw model. The white areas above and beneath the voltage sensor S4 indicate water crevices that extend into the cellular membrane. B) The paddle model.

flow must exist in these channels. This current was termed *omega current*[8]. Based on further examination of the permeation of different ions, the authors came to the conclusion that the replacement of R1 with a smaller amino acid opens a pathway between two water–filled vestibules on either side of R1. If R1 were embedded in the hydrophobic lipid membrane – as predicted by the paddle model (see section 1.3.3) –, the reason why the omega current is dependent on mutations of R1 and why it only appears in the resting state would remain unexplained.

### 1.3.3 The paddle model

After Jiang and colleagues had solved the crystal structure of the KvAP channel, they proposed the paddle model in which segments S3 and S4 of $K^+$ channels are thought to move in a paddle–like manner through the membrane when the channel activates (see figure 1.7, B). Because the crystal structure is only a static representation of the channel (most likely in the open configuration due to the absence of electrical fields), they additionally tested whether biotinylated cysteine residues on S4 bind to avidin[9] from either side of the membrane and whether the binding is dependent on transmembrane voltage [19]. First they showed that that a channel without biotin does not alter its functioning when subject to avidin and then that movement of S4 of the modified channel can be inhibited by the binding to avidin. By varying the linker–lengths with which the biotin molecules were attached

[8]The ionic current that flows upon the depolarization of a cell is called *alpha current* and the pore through which this current flows *alpha pore*. By analogy, the new ionic pathway is called the *omega pore* and the current *omega current*.

[9]The protein avidin has an extraordinary high affinity to biotin (association constant $K_a \simeq 10^{15}$) and both avidin and biotin can be attached to other biomolecules. For this reason, the avidin/biotin complex allows to mark locations in biological systems with very high selectivity.

to the cysteine residues they could test how long the linker has to be to still have an effect on channel gating. Based on these observations, they concluded that the voltage–sensor of the KvAP $K^+$ channel moves $\simeq 20$Å within the lipid membrane when it switches from the closed to the open state.

In the last 10 years, a number of publications have tried to answer the question of which model best describes voltage–sensor movement, or whether a whole new model has to be developed to explain channel gating on the molecular level. The most important studies will be discussed in the following.

In 2005, Ruta and colleagues [20] made a very similar experiment as Jiang [19] – again probing distances by biotin/avidin binding reactions on the KvAP $K^+$ channel. In agreement with Jiang, they concluded that S4 moves 15–20Å through the membrane when the channel switches from the closed to the open state.

Ahern and Horn changed R1 in S4 of a *Shaker* $K^+$ channel by a cysteine residue and brought the channel protein in contact with cysteine–reactive probes that had positively charged molecules attached to them with varying linker–lengths [26]. They measured the gating charge as a function of linker–length and compared it to the unaltered channel. They found that the gating charge is identical to the gating charge of the original channel for very short linkers, and that it decreases with linker–length up to a length of 4Å. Based on this finding, they reasoned that the attached charge is not dragged into the electric field in case the linker is longer than 4Å, and therefore that the voltage drop across the membrane must occur within 4Å. Because the thickness of the lipid bilayer is $\simeq 30$Å they suggested the existence of water crevices in the channel protein in the region of R1, and consequently that S4 moves in protein environment.

The existence of a separate *"channel"* in the protein through which S4 moves during activation was originally proposed by Yang et al. in 1996 [12]. They tested the accessibility of all seven arginines R1–R7 on S4 of the human skeletal muscle $K^+$ channel hSkM1. They found that R2–R7 are accessible from the inside when the cell is hyperpolarized, while in a depolarized state R1–R3 are accessible from the outside and R4–R7 only from the inside. Since only residues R2 and R3 change the side from which they are accessible when the voltage sensor moves, the authors suggested a pathway for the movement of S4 that is within the rest of the channel protein and separates the extracellular from the intracellular volume by less than 11Å.

In 2005, Posson and colleagues used fluorescence resonance energy transfer (FRET) to estimate how far segment S4 moves when the *Shaker* $K^+$ channel changes its conformation when it switches from the closed to the open state [27]. They attached donor fluorophores to various positions of S4 and acceptor fluorophores onto a pore–blocking toxin. They then measured the distance between donor and acceptor as a function of the activation state of the channel. They estimated that the distance the voltage sensor moves is as little as 2 Å.

Another FRET study was taken out by Chanda and colleagues in which they reported a *"limited transmembrane S4 movement"* of the *Shaker* $K^+$ channel [28]. They attached donor molecules at various positions of segment S4 and positioned acceptor molecules at either side of the membrane. It seems reasonable to assume that the FRET signal changes when segment S4 moves through the membrane during channel activation. However, they did not observe any signal changes. Although they did not quantify the distance of the movement, they concluded that S4 moves only a small distance and certainly does not translocate over the whole thickness of the membrane.

The distance between the voltage–sensor paddle of a Kv2.1 $K^+$ channel and the outer membrane surface was estimated to be shorter than 8 Å in a study by Phillips and colleagues in 2005 [29]. They used hanatoxin, which is a neurotoxin that blocks $K^+$ channels by binding to the voltage sensor [30]. When it binds to the voltage sensor it stabilizes the channel in the resting state and closely follows the movement of the voltage sensor during activation. Fluorescence of a tryptophan residue on the toxin could be quenched by bromide introduced in the membrane at various depths. The tendency of hanatoxin to bind to the voltage sensor in lipid and the fact that the binding surface faces lipid [31], indicate that the voltage sensor moves along the protein–lipid interface.

Ahern and Horn replaced charged residues of S4 in a *Shaker* $K^+$ channel, reintroduced the lost charges by attaching charged molecules at various positions, determined the gating charge and then compared it to the unaltered channel [32]. Interestingly, the full gating charge of the original channel could be restored only if the charges were attached to the exact same positions of the original ariginine residues. In lipid, the interaction between charges and the relatively homogeneous and hydrophobic volume could not be expected to be so strongly dependent on the exact position of the charges. For this reason, the observations by Ahern and Horn strongly indicate that segment S4 moves in a protein environment.

The paddle model predicts a movement of the voltage sensor in the order of ≃ 20 Å while in the helical screw model, this distance is expected to be about half that value. The large differences in the movement of the voltage sensor – as determined by the aforementioned studies –, ranging from 2–20 Å, are striking. How can they be explained? One reason might lie in structural differences of the channels that were studied (the bacterial channel KvAP, the mammalian channels Kv2.1 and *Shaker*). These structural differences reasonably explain the disparities in the distance measurements in part, but not totally. Indeed, gating properties as well as the primary structure of the voltage sensor of bacterial and eucariotic channels are extremely similar.

The interaction between hanatoxin which is embedded in the membrane and charged residues on the voltage sensor S4 is electrostatic and therefore acts over relatively large distances. For this reason, the 8 Å obtained by Phillips et al. [29] are probably a lower limit and could still be in agreement with the 15–20 Å obtained by Ruta et al. [20] and Jiang et al. [19]. Even the 4 Å from the study by Ahern and Horn [26] may be compatible with the other findings if the proposed water crevices above and below the voltage sensor S4 are deep enough. Only the very low value of 2 Å obtained by Posson et al. [27] seems not to fit into the picture. However, the coupling between donor and acceptor in fluorescence energy resonance transfer is strongly orientation dependent. It can thus be speculated whether the 2 Å significantly underestimate the distance over which the voltage sensor moves during activation.

While the distance measurements could still be compatible with both models, studies targeting the environment in which the voltage sensor moves clearly imply that S4 is in direct contact with the rest of the channel protein [12, 24, 32]. For the time being the helical screw model describes the available data to a much larger extent with no obvious contradictions (see also the review by Chanda and Bezanilla which focuses on a discussion about the voltage sensor pore [33]).

Very recently Bezanilla and colleagues in 2008 proposed the existence of a third state – which they called the *relaxed state* – that the voltage sensor S4 occupies between the activated and the resting state [34]. They studied the gating mechanism of the voltage dependent phosphatase Ci–VSP, which is not an ion channel but reveals primary and secondary structures very similar to the ones found in voltage gated ion channels. The authors

propose that the secondary structure of S4 is a $3_{10}$–helix[10] which switches to an $\alpha$–helix when the channel conforms to the relaxed state. This could account for some discrepancies in the distance measurements discussed in the preceding paragraphs.

[10] A $3_{10}$–helix is a rarely found type of secondary structure. As the $\alpha$–helix it is a coil of amino acids but it has only three residues per turn (as opposed to 3.6 in the $\alpha$–helix).

# 2 The size of the gating charge in $K^+$ and $Na^+$ ion channels

The question of how many elementary charges contribute to the gating process of voltage gated ion channels has been at the core of many studies. The most direct approach to answer this question would be to directly measure the gating current of a single ion channel, for example by patch–clamping. However, while the ionic current through an ion channel is in the order of pA – and can be resolved even for single channels –, the corresponding gating current is three orders of magnitude smaller, which is a signal hardly detectable in a biological sample. The common approach to increase the signal is to use samples with large numbers of channels ($10^8$–$10^{10}$ channels per sample) and then find a method to quantify the corresponding number of ion channels. While the determination of the gating charge of large channel populations is fairly straightforward (the two electrode voltage clamp technique and patch–clamping are reliable standard procedures in electrophysiology), the estimation of the number of channels still poses a source of considerable uncertainty.

The present study compares the size of the gating charge of two voltage gated ion channels: the *Shaker* $K^+$ channel and the rat brain IIA (rBIIA) $Na^+$ channel. Both channels were specifically labeled with genetically encoded *enhanced green fluorescent proteins* (GFP), which allowed to estimate the number of channels by a novel approach based on fluorescence intensity measurements (see section 2.3.3, page 56 and section *Autofluorescence* of the manuscript, page 64). This approach is designed to determine a relative measure of the number of channel proteins in the sample: it allows to compare the sizes of gating charges of different channel types. The gating currents were determined by the two electrode voltage clamp technique which will be presented and discussed in section 2.2.1 on page 43.

It was found that the gating charge of a single *Shaker* $K^+$ ion channel is $2.5 \pm 0.4$ times larger than that of a rBIIa $Na^+$ channel. While $K^+$ channels have been extensively studied in the past, this finding is of particular interest in relation to the lesser known $Na^+$ channel. Based on the literature about $K^+$ channels, an absolute value of the size of the gating charge of the rBIIa $Na^+$ channel could be derived. Very consistently throughout the various studies, the size of the gating charge of the *Shaker* $K^+$ channel was found to be of $\simeq 13$ elementary charges, which leads to $\simeq 5.2 \pm 0.3$ elementary charges for the size of the gating charge of the rBIIa $Na^+$ channel.

Further studies, which will be discussed later in this section, quantified the size of the charge which moves in the electric field in the membrane during the gating process. The two most often used methods involved in the estimation of the gating charge shall briefly be outlined: *variance analysis* and the *limiting–slope method*. While the latter directly reveals the gating charge of a channel protein, the first only provides with an estimation of the number of ion channels in the sample. Together with the separately determined gating charge of all channels in the sample, the gating charge of a single channel can be calculated.

## The limiting–slope method

Both the number of open channels $\#_o$ and their ionic conductivity $g$ depend on the transmembrane voltage $V$. It seems reasonable to further assume that the number of open channels is proportional to the total ionic membrane conductivity:

$$\#_o(V) = c_1\, g(V) \qquad \Longrightarrow \qquad \#_{tot} = \#_o(V \gg V_r) = c_1\, g_{max}$$

where $c_1$ is the proportionality factor between the ionic conductivity and the number of open channels, $\#_{tot}$ is the total number of channels, $V_r$ is the voltage at the resting state of the ion channel and $g_{max}$ the conductivity, when all channels are in their open configuration. The ratio between the number of open and closed channels can then be written as:

$$\frac{\#_o}{\#_c} = \frac{\#_o}{\#_{tot} - \#_o} = \frac{g}{g_{max} - g} = \left(\frac{g_{max}}{g} - 1\right)^{-1} \tag{2.1}$$

If the channel protein is characterized by being either open or closed, this ratio can also

be expressed by the Maxwell–Boltzmann statistics for a two–state system:

$$\frac{\#_o}{\#_c} = \exp\left(-\frac{u_o - u_c}{k_B T}\right) \tag{2.2}$$

where $u_o$ and $u_c$ are the energies of an open or closed channel, $k_B$ is Boltzmann's constant and $T$ the absolute temperature. The energy difference between the open and closed states $u_o - u_c$ is the sum of the change in energy associated with the conformational change of the protein and the energy associated with the movement of electric charges through the electric field along the membrane. While the former is independent of the electric field $\epsilon$, the latter is equal to $-zeV$, where $z$ is the valence of the gating charge, $e$ the elementary charge, and $V$ the potential difference across the membrane. Then equation 2.2 transforms to:

$$\frac{\#_o}{\#_c} = \exp\left(-\frac{\epsilon - zeV}{k_B T}\right) = c_2 \exp\left(\frac{zeV}{k_B T}\right) \qquad \text{with } c_2 := \exp\left(-\frac{\epsilon}{k_B T}\right) \tag{2.3}$$

For very negative potentials ($g \ll g_{max}$) equation 2.1 simplifies to:

$$\frac{\#_o}{\#_c} = \frac{g}{g_{max}} \qquad \text{if } g \ll g_{max}$$

and together with equation 2.3 the ionic conductivity can now be expressed as:

$$g = c_3 \exp\left(\frac{zeV}{k_B T}\right) \qquad \text{with } c_3 := c_2 g_{max} \tag{2.4}$$

which demonstrates that the ionic conductivity exponentially depends on the membrane potential if the transmembrane voltage is sufficiently small.

For practical purposes, the *logarithmic potential sensitivity* (LPS) is defined as the derivative of the logarithm of the ionic conductivity as formulated in equation 2.4:

$$\text{LPS} := \frac{\mathrm{d}}{\mathrm{d}V}(\ln g) = \frac{\mathrm{d}}{\mathrm{d}V}\left(\ln c_2 + \frac{zeV}{k_B T}\right) = z\frac{e}{k_B T} \tag{2.5}$$

The LPS is directly proportional to the valence of the gating charge. If the ionic conductivity is plotted on a logarithmic scale as a function of the transmembrane voltage, the slope of the curve at very negative voltages corresponds to the gating charge of a single channel (hence the term *limiting–slope*).

On a logarithmic scale, the conductivity increases the fastest near the resting potential difference. When the transmembrane voltage is reduced progressively toward the resting potential difference, more and more channels will close their pore until at some point the ionic current will be below detection threshold. For this reason, the ionic conductivity of an ion channel cannot be determined at arbitrarily small voltages, and therefore only a lower limit of the number of gating charges per channel protein can be determined with the limiting–slope method.

In the preceding section it was assumed that the gating process can be described as a two–state system. However, this most likely does not describe the gating process to its full extent. The channel probably undergoes various states associated with conformational changes of the protein, while not being conductive to ions. The same argumentation applies to the open state: possibly different open states exist which give rise to gating currents but which are indistinguishable by analyzing the ionic currents. Appendix A discusses this problem more generally via the introduction of multi–state models.

## Variance analysis

For a system with a single ion channel the mean current $<I>$ is the product of the ionic current through the channel $i$ and the probability $p$ that the channel is in its open state:

$$<I>= ip \tag{2.6}$$

The variance of the ionic current is the sum of the squared deviations from the mean current, each multiplied with its respective probability. Because the channel is either open (with probability $p$ and current $i$) or closed (with probability $(1-p)$ and zero current), this leads to:

$$\sigma_I^2 = (1-p)(0-ip)^2 + p(i-ip)^2 = i^2p - i^2p^2 \tag{2.7}$$

For a system with $N$ ion channels that function independently, equations 2.6 and 2.7 change to:

$$<I>= Nip \tag{2.8}$$

$$\sigma_I^2 = Ni^2p - Ni^2p^2 \tag{2.9}$$

The mean current and the variance become $N$ times larger. Furthermore, the variance vanishes if all channels are closed ($p = 0$) or if all channels are open ($p = 1$). Applying equation 2.8 to equation 2.9 leads to:

$$\sigma_I^2 = i < I > - \frac{< I >^2}{N} \qquad \Longrightarrow \qquad \frac{\mathrm{d}\sigma_I^2}{\mathrm{d} < I >} = i - \frac{2 < I >}{N}$$

Now the variance $\sigma_I^2$ can be expressed as a function of the mean current $< I >$. $\sigma_I^2$ is a parabola which has its maximum at $< I >_{\mathrm{max}} = iN/2$. For very small values of $< I >$ the slope of the parabola is equal to the single channel current $i$. With this information, the number of channels can be calculated as:

$$N = \frac{2 < I >_{\mathrm{max}}}{i} \tag{2.10}$$

Recapitulating, the ionic current of a population of ion channels is measured at different transmembrane voltages (which correspond to certain probabilities for the channels to be open). For each current trace the variance of the signal is calculated and plotted as a function of the ionic current. The slope of the resulting curve at very low voltages reveals the gating current of a single ion channel. Together with the current at the maximum of the curve, the number of channels can be determined by applying equation 2.10. Details of this method and an explanation of its application to ion channels can be found in [35–38].

In the following, an overview about the most important studies of the last decades on the quantification of gating charges of ion channels shall be given. With regard to the manuscript which compares the gating charges of $K^+$ and $Na^+$ channels, this overview is separated into sections dealing with $K^+$ and $Na^+$ channels.

## $K^+$ channels

In 1992, Schoppa et al. published the first estimates of the size of the gating charge for the *Shaker* $K^+$ channel [39]. They investigated the wild–type (wT) *Shaker* $K^+$ channel and a mutation of the channel that does not inactivate [40]. They expressed[1] the channels

[1] *Gene expression* refers to the process of assembling a protein out of a gene (a specific sequence of DNA which encodes for the protein and stores the information on how to assemble it) and occurs in two steps: 1) The nucleotide sequence of the DNA is copied to RNA, this is termed *transcription*, 2) The RNA is used to direct protein synthesis which is known as *translation*. If a certain protein (e.g. an ion channel) is to be studied, the corresponding RNA is genetically engineered and injected into a cell (in this case *Xenopus laevis* oocytes) where the protein is assembled. Even though only translation is involved, this process is also called expression. The cell in which the translation occurs is called the *expression system*.

in *Xenopus laevis* oocytes and determined the single gating charge by both the limiting–slope method and by fluctuation analysis. For the wT channel they obtained values of $9.5 \pm 1.2$ and $12.4 \pm 1.2$ elementary charges per channel with the limiting–slope method and with variance analysis, respectively. The same measurements performed on the non–inactivating channel revealed $5.5 \pm 0.5$ and $12.2 \pm 2.1$ elementary charges. As expected, values determined by the limiting–slope method are lower, because this method only allows to determine a lower limit. Interestingly, fluctuation analysis reveals the same value for both channel types. This indicates that inactivation does not necessarily have an effect on the size of gating currents.

Zagotta and colleagues also studied the non–inactivating *Shaker* $K^+$ channel [41]. They expressed the channel proteins in *Xenopus laevis* oocytes, determined the ionic currents by patch clamping the cells, and used the limiting–slope method to determine the number of channels in the oocyte membrane. They found that a charge of the size of 12 – 16 elementary charges contributes to the gating process.

In 1996, Noceti and colleagues used a mutation of the *Shaker* $K^+$ channel with inactivation removed [42]. They patch–clamped channels which were expressed in *Xenopus laevis* oocytes. With the limiting–slope method and variance analysis they found that a charge of the size of $12.79 \pm 0.26$ and $13.62 \pm 0.63$ elementary charges contributes to the gating process, respectively. The gating charge was determined after adding tetraethylammonium[2] (TEA) to the interior of the cells in order to block ionic currents.

Aggarwal and MacKinnon determined the size of the gating charge of the *Shaker* $K^+$ channel [43]. As an expression system they used *Xenopus laevis* oocytes and determined the gating charge of the channel population by two electrode voltage clamp. They used agitoxin[3] to suppress ionic currents. Because the toxin was radiolabeled they could estimate the number of channels that were expressed in the oocyte by determining the decay rate as a function of toxin concentration. They found the *Shaker* $K^+$ channel to have a gating charge equivalent to 13.6 elementary charges.

In 1999, Islas and Sigworth also studied the *Shaker* $K^+$ channel and came to the conclusion that a charge of the size of 13 elementary charges are involved in the gating process

[2] TEA is a neurotoxin which blocks $K^+$ channels. In an organism subject to poisoning with TEA, repolarization of the cell is strongly suppressed during an action potential. As a consequence, the action potential is prolonged and the neuronal activity is disrupted, which can lead to uncontrollable repetitive muscular contractions (tetany).

[3] Agitoxin is another neurotoxin found in the venom of certain scorpions. It selectively blocks the $K^+$ channel pore with a stoichiometry of one to one.

| Channel type | Gating charge [$e$] | Notes | |
|---|---|---|---|
| ***Shaker* $K^+$** | **12.2±2.1** | [39], 1992 | a |
| ***Shaker* $K^+$** | **12.4±1.2** | [39], 1992 | b |
| ***Shaker* $K^+$** | **12–16** | [41], 1994 | a |
| ***Shaker* $K^+$** | **13.62±0.63** | [42], 1996 | a |
| ***Shaker* $K^+$** | **13.6** | [43], 1999 | |
| ***Shaker* $K^+$** | **13** | [44], 1999 | |
| Kv2.1 $K^+$ | 12.5 | [44], 1999 | |
| Mammalian $K^+$ | 7.2 | [45], 1991 | |
| **rBIIA $Na^+$** | **4.6–6.9** | [46], 1989 | |
| Squid giant axon $Na^+$ | $\geq 4-6$ | [3], 1952 | |
| Rat skeletal muscle $Na^+$ | $\geq 12$ | [47], 1995 | c |
| hH1a $Na^+$ | $\geq 5.2$ | [48], 2005 | |
| NaChBac $Na^+$ | 16 | [49], 2004 | d |

[a] Inactivation removed. [b] Wild–type *Shaker* $K^+$ channel.
[c] Fast inactivation removed. [d] This channel differs in so many properties from the rBIIA $Na^+$ channel that it can hardly be compared to it (see text for details).

Table 2.1: The number of gating charges of a variety of $K^+$ and $Na^+$ ion channels. Channel types that are identical or very similar to the ones used in the present study, are bold printed.

[44]. They determined the gating charge with patch–clamp recordings on channels expressed in *Xenopus laevis* oocytes and estimated the number of channels by the limiting–slope method. In the same study they determined the size of the gating charge of the mammalian $K^+$ channel Kv2.1 to be of 12.5 elementary charges.

## $Na^+$ channels

As already mentioned in section 1.3, Hodgkin and Huxley were the first to introduce the concept of gating charges (which they termed *activation particles*) as early as 1952 [3]. They determined the voltage dependence of the ionic current of $Na^+$ channels with voltage–clamp measurements and then derived the number of activation particles purely by mathematical concepts, for which they just assumed that they had a physical meaning[4]. For the $Na^+$ channel of the squid giant axon they postulated, that at least 4–6 elementary charges have to be associated with the activation particles.

The work of Conti and Stühmer from 1989 is of special interest, because it is the only study that used the same $Na^+$ channel as in the present study [46]. Their expression

[4] It turned out however that they came surprisingly close to the modern view about ion channels.

system was the *Xenopus laevis* oocyte on which they performed patch–clamping of macro–patches. Channel pores were blocked by the neurotoxin tetrodotoxin[5] (TTX). Variance analysis of the gating current signals allowed them to determine the gating charge of a single channel. They concluded that the activation of the rat brain type IIA (rBIIA) $Na^+$ channel occurs in two to three successive steps, each associated with the movement of a charge equivalent to $\simeq 2.3$ elementary charges. Because the $Na^+$ channel has four subunits this adds up to a total charge of the size of 4.6–6.9 elementary charges per channel.

Six years later, Hirschberg and colleagues found that the gating charge of the rat skeletal muscle $Na^+$ channel with fast inactivation removed has to be at least of the size of 12 elementary charges [47]. They expressed the channels in *Xenopus laevis* oocytes and used the limiting–slope method to estimate the number of channels. They were able to measure the open probability of the channels down to $\simeq 10^{-7}$ (which was unusually low at the time) and noticed that in this very region the open probability increases very fast with transmembrane voltage, which explains the rather high number of 12 elementary charges.

The human cardiac $Na^+$ channel hH1a has a gating charge equivalent to at least 5.2 elementary charges [48]. In 2005, Sheets and Hanck mutated one of the charged residues in the subunit S4 of domain IV (S4DIV) of the hH1a channel to an uncharged one, which reduces the total gating charge measured by voltage clamp by $\simeq 20\,\%$. The exposure of the sample to the positively charged methyl thiosulfonate ethylammonium (MTSEA) reagent fully restored the gating charge. Because the binding of MTSEA can add at the most one elementary charge (see [48]) to the gating charge of a single channel, Sheets and Hanck could calculate a lower limit of the size of the gating charge.

Kuzmenkin and colleagues investigated the NaChBac $Na^+$ channel from *Bacillus halodurans*, and found that a charge of the size of 16 elementary charges moves when the channel opens [49]. However, the NaChBac $Na^+$ channel is a rather untypical $Na^+$ channel for several reasons: 1) It is a homotetramer of one domain containing six transmembrane spanning segments, which is a structure similar to $K^+$ channels, 2) its pore structure very much resembles the $Ca^{2+}$ channel pore structure, 3) it is insensitive to TTX and 4) current kinetics are 10–100× slower than for other $Na^+$ channels. Furthermore, the expression system in this study consisted of COS–1 cells, which is a cell line derived from the kidney

[5] TTX is one of the strongest non–protein neurotoxins ($LD_{50} \simeq 10\,\mu g/kg$) which selectively blocks $Na^+$ channels. Among other species it occurs naturally in the pufferfish and was isolated for the first time in the 1950's [50]. In an organism, the blocking of $Na^+$ channels leads to the suppression of action potentials and as a consequence to paralysis.

of the African green monkey. For all these reasons, this channel can hardly be compared to the rBIIa channel and has only been listed for reasons of completeness.

The *Shaker* $K^+$ channel is one of the most extensively studied channel types (see table 2.1). Considering the different techniques that were used to determine the gating charge of a single channel, it is striking that the results lie so close to each other at around 13 elementary charges per *Shaker* $K^+$ channel.

Only one study investigated the rBIIA $Na^+$ channel, which was also used in the present study. The other three studies – neglecting the NaChBac $Na^+$ channel for the above–mentioned reasons – inconsistently report lower limits of 4.5, 12 and 5.5 elementary charges, respectively. However, this might be due to differences in channel structures.

## 2.1 The expression system

In the present study, oocytes (immature egg cells) of the African clawed frog *Xenopus laevis* were used to express $K^+$ and $Na^+$ ion channels (see figure 2.1). A pigment layer underneath the cellular membrane of the oocytes is responsible for the dark coloration on one half of the oocyte, the so–called *animal pole*[6]. This has a profound impact on fluorescence intensity measurements, because the autofluorescence due to various cytoplasmatic compounds is greatly reduced in this region (see section *Autofluorescence* of the manuscript, page 64).

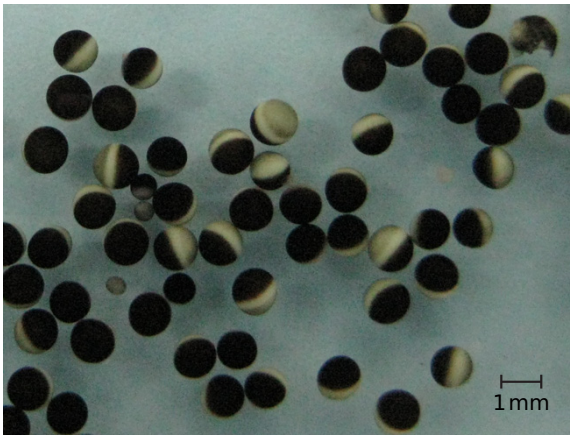


Figure 2.1: *Xenopus laevis* oocytes. The dark coloration of one half of the oocyte is due to a pigment layer underneath the membrane.

After extraction of the oocytes from the frogs by means of a small operation[7], RNA coding for ion channels was microinjected into the oocytes, where the corresponding channel proteins are synthesized. Quite remarkably, the channel proteins even move to the cel-

[6] In the wild, fertilized oocytes float in the water with the animal pole facing upwards while the embryos are developing. In this way, they are less easily spotted by predators from either side: from the top they blend in with the dark coloration of a pond or a lake; from the bottom, they blend in with the lighter background of the sky.

[7] The operation is a small incision at the lower abdomen of the anesthetized frog. After extraction of a few hundred oocytes, the wound is restitched and completely heals within a few weeks.

lular membrane which incorporates them. These processes take place in the same manner as in the organism the RNA originally stems from [51, 52]. This makes *Xenopus laevis* oocytes such a powerful tool for cell biologists and it is one of the reasons for its widespread use in research[8].

Because of their biological function to harvest embryos and promote their development, oocytes have the ability to synthesize proteins at high rates during and before fertilization, which is of particular importance because unfertilized oocytes were used. *Xenopus laevis* oocytes contain more ribosomes – the place where RNA is synthesized into proteins – than somatic cells by several orders of magnitude [53]. Therefore, they can efficiently translate not only endogenous[9], but also exogenous RNA into proteins (e.g., ion channels) [54]. In 1971 Gurdon and colleagues were among the first to show that foreign RNA could be expressed in *Xenopus laevis* oocytes [55].

In their natural environment, oocytes have to be self–sufficient to survive. For this reason, all nutrients and substrates necessary to translate and express proteins are embedded in the membrane and in the intracellular volume of the oocyte. Therefore, they express only a small number of endogenous membrane transporter systems which could potentially interfere with the function of exogenously expressed ion channels or obstruct measurements thereof [56, 57].

The frogs continuously produce oocytes, irrespective of seasonal changes. Oocytes of all stages[10] are thus available at any given point in time. Only unfertilized oocytes of stage VI were chosen for the experiments, because they are the most developed ones. Therefore expression can be expected to progress fast. These cells have a typical size of about 0.8–1.3 mm (see figure 2.1), which allows easy handling and manipulation (microinjection of RNA, preparation for voltage–clamp, moving and rotating the oocyte to arbitrary positions).

[8] Another reason is the fact that *Xenopus laevis* frogs were used for pregnancy tests during a long time: female frogs ovulate when they are injected with human chorionic gonadotropin, a hormone present in the urine of pregnant women.

[9] *Endogenous* RNA is RNA that occurs naturally in a given organism. By contrast, *exogenous* RNA is RNA that is foreign to the organism in which the protein is eventually expressed.

[10] Dumont introduced a system to classify oocytes according to their level of development. This system is still widely in use. It distinguishes six stages, stage I being the first and least developed stage and stage VI being the last and most developed stage [58].

## 2.2 Determination of the gating charge

As mentioned before, a large number of ion channels has to be present in a sample to make the gating current detectable. This number can be regulated in two ways: 1) by the amount of RNA injected into the cell (within a certain range, the number of expressed channels increases linearly with the amount of injected RNA) and 2) by varying the time between RNA injection and the start of the experiment (after injection, the number of expressed channels typically increases for the first few days linearly, increases further but at a slower rate for the next few days, and reaches a constant level before the cell disintegrates after about 10−15 days).

Additionally, gating currents can only be measured in the absence of ionic currents. The *Shaker* $K^+$ channel that was used in this study is a mutation with a blocked ion pore, therefore this channel is completely impermeable to ions. Up to now no such mutation that leaves the channel function unaltered was found for the rBIIA $Na^+$ channel. In the present case, ionic currents were suppressed by TTX.

A variety of techniques exist to stimulate a cell electrically and to measure the subsequent ionic flow or the rearrangement of charged residues. In the present study, the two electrode voltage clamp technique was used.

### 2.2.1 The two electrode voltage clamp technique

The electrical properties of a cell with membrane bound ion channels can be represented with a simple electrical circuit as illustrated in figure 2.2, A. In this figure, the capacitance of the membrane is represented by $C_m$ and leakage currents flow through the resistor $R_l$. The resistance of the ionic pore is represented by the variable resistor $R_m$ which changes its resistivity depending on whether the ion channel is in its open or closed state. The series resistor $R_s$ is not part of the membrane and is comprised mainly of the resistance of the voltage electrode $E_v$ (see figure 2.2, B).

To measure the ionic conductivity of ion channel proteins, or more generally to measure the currents, that flow through the cellular membrane, principally two methods are possible: 1) Passing a constant current through the system and recording the changes of the electrical potential difference or 2) setting the transmembrane voltage to a certain value and recording the current that is needed to maintain that voltage. The latter method is ap-

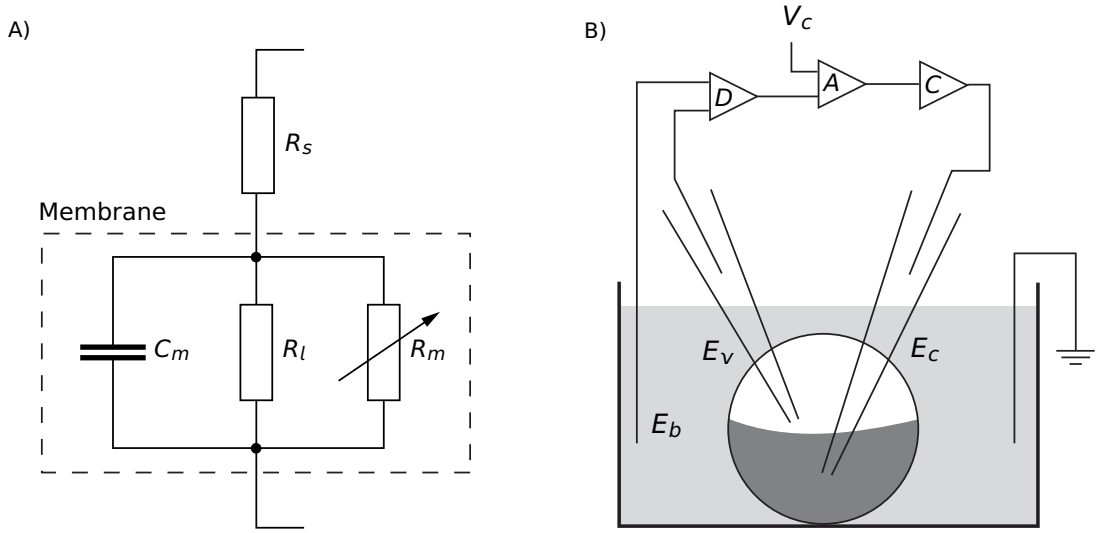


Figure 2.2: Equivalent circuit of the membrane and two electrode voltage clamp setup. A) Equivalent circuit of the membrane. $C_m$ is the capacitance of the membrane, $R_l$ represents the branch through which leakage currents flow, $R_m$ is a variable resistor representing the varying conductivity of the ion channels and $R_s$ represents the series resistance of the voltage clamp. B) The potential difference between the inside and the outside of the cell is measured by the operational amplifier $D$ whose inputs are the voltage electrode $E_v$ and the bath electrode $E_b$. The output of $D$ is compared with the command voltage $V_c$ by the differential amplifier $A$. The operational amplifier $C$ generates a current that is proportional to the output signal of $A$. This current is injected into the cell through the current injecting electrode $E_c$.

plied in the two electrode voltage clamp technique (TEVC). The basic principle underlying this method is a negative feedback circuit as illustrated in figure 2.2, B. This circuit allows to measure the current that flows through the membrane to maintain an arbitrarily set potential difference between the inside and the outside of a cell. The potential difference between the interior of the cell and the bath solution is measured by the voltage recording electrode $E_v$ and the bath electrode $E_b$ which is held at ground level. This signal is then fed into the operational amplifier $D$ whose output is compared with the command voltage $V_c$ in the differential operational amplifier $A$. Here, a signal proportional to the difference of the membrane voltage and the command voltage is generated. In the operational amplifier $C$ a current is generated and injected into the cell through the current injecting electrode $E_c$ such as to minimize the difference signal generated in $A$. As a consequence, the voltage across the membrane is forced to the value set by $V_c$ (the cell is *clamped* to $V_c$) and, if the system is fast enough, the injected current exactly counter balances the ionic and gating currents that flow through the membrane. In TEVC this current is recorded as a function of the command voltage $V_c$. Errors are introduced in the measurement mainly by means of the *series resistance* $R_s$, by means of the membrane capacitance $C_m$ and by so–called *space clamp* errors.

Ideally, the voltage electrode $E_V$ measures the voltage drop across the membrane. However, the fine electrodes that are used have a rather high resistance ($\simeq 100-200\,\mathrm{k}\Omega$) which is in series with the membrane resistance $R_m$. For this reason, the measured voltage reflects the sum of the voltage drops across the membrane and across the electrode's resistance. When a current $I$ flows through the electrode the series error is equal to $IR_s$, which usually is too high to be acceptable. The series resistance error can be compensated for by adding a voltage signal to the command voltage that is proportional to the current generated by the operational amplifier $D$. This procedure allows to compensate $\simeq 90\,\%$ of the error.

Ion channel kinetics are in the order of ms. However, because the capacitive currents are much larger than the gating currents, during the time the membrane is charged, gating currents cannot be resolved. The time constants involved in charging the membrane capacity are about two orders of magnitude larger than the channel kinetics. To overcome this problem, simultaneously with the change of the command voltage $V_c$, a much larger current than needed for compensation is generated and injected into the cell through the current injecting electrode $E_c$. This procedure allows to speed up the charging process to fractions of ms which allows to study channel kinetics at the ms level.

If single channel properties are to be deduced from the superposition of signals of a large number of ion channels, it is important that all channels are exposed to the same electrical conditions at the same time. Space clamp errors appear when different locations on the cellular membrane are charged up with different time constants. One reason for this to happen can be varying conductivities of the cytoplasmatic solution. Another reason can be the asymmetrical positioning of the current injecting electrode. While the former can usually be neglected, the latter has to be taken great care of. Depending on where the two electrodes are positioned, the measured transmembrane voltage will reflect only the voltage drop at a certain position and, as a consequence, the injected current will not reflect the true ionic or gating current that is elicited by this specific voltage. This phenomenon is of primary importance when working with large cells as *Xenopus laevis* oocytes. Space clamp errors can readily be minimized by placing the current injecting electrode $E_i$ in the center of the oocyte. A discussion of space clamp errors and methods to reduce them can be found in [59].

## Microelectrodes

The electrodes which are impaled into the oocyte are glass pipettes, that are filled with a concentrated 3 M KCl solution. They are fabricated by pulling a glass cylinder at both ends, while heating the middle part. As the glass melts, the typical conical form of a pipette emerges. The tip of the pipette is then broken to provide with sharp edges in order to minimally damage the oocyte when the pipettes are impaled. The front opening of the pipette is filled with agarose gel[11] to prevent the KCl solution from flowing into the cell. An AgCl coated silver wire is inserted into the back end of the pipette to apply the electrical contact to the aqueous solution of the intracellular volume of the cell. To find the optimum dimensions for the pipettes, two properties have to be balanced against each other:

1) The point at which the pipettes impale the cellular membrane can be a source of large leakage currents. The membrane can even be damaged so badly that the cytoplasm flows in the extracellular space, at which point an experiment is no longer possible. Therefore, the pipettes should be designed as thin as possible.

2) The resistance of the pipettes should be as small as possible, because the resistance affects the speed and accuracy of the voltage clamp. This is particularly important for the current injecting electrode $E_C$, and may be achieved by enlarging the diameter of the pipette.

Typically, the electrode $E_V$ – which measures the transmembrane voltage – has a diameter of $\simeq 8$–$12\,\mu$m, and $E_C$ has a diameter of $\simeq 4$–$8\,\mu$m. Resistances of the electrodes were in the range of $\simeq 100$–$200\,\mathrm{k}\Omega$.

## Pulse protocols

If it were possible to measure the gating current of a single channel, it would be quite simple to determine the gating charge (assuming that a channel has only one open and one closed state, which strictly speaking is not correct). Indeed, if the channel opened at some pulse height, integration of the gating current would directly reveal the gating charge, independently of the size of the applied pulse. In other words, integration of the current would either be zero (in which case the experiment would have to be repeated with a higher pulse) or of some constant value.

[11] Agarose is a polysaccharide which is used as a salt–bridge between the salt solution of the pipette and the intracellular volume.

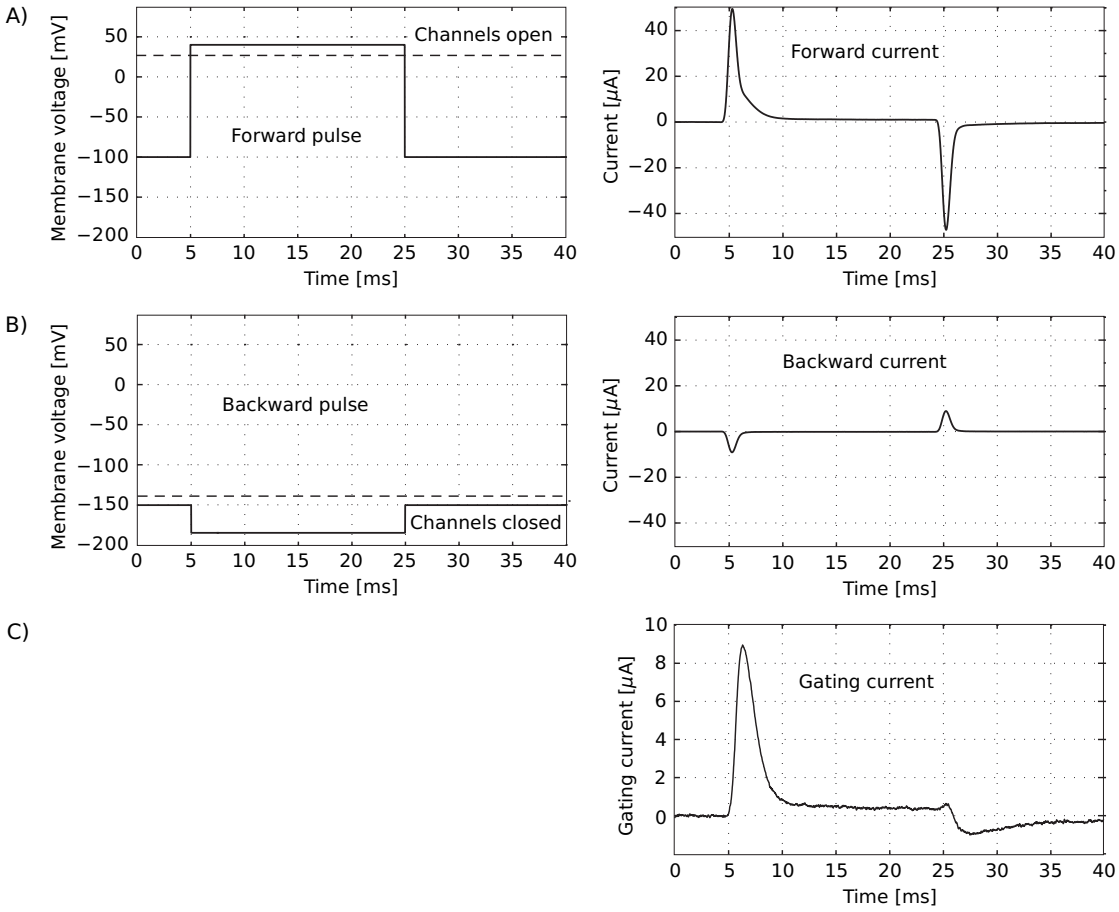


Figure 2.3: Two electrode voltage clamp pulse protocols to determine the gating charge of a population of ion channels. A) Forward pulse from the resting potential to a region where most of the channels are in their open conformation ($-100 \rightarrow +40\,\mathrm{mV}$; pulse height $V_f = 140\,\mathrm{mV}$). The measured current $I_\mathrm{f}$ is shown on the right side. At voltages above the dashed line all channels are open. B) Backward pulse in the hyperpolarized region, where channels are in their closed conformation ($-150 \rightarrow -180\,\mathrm{mV}$; pulse height $V_f = -30\,\mathrm{mV}$). The measured current $I_\mathrm{b}$ is shown on the right side. At voltages below the dashed line all channels are closed. C) Gating current $I_g = I_\mathrm{f} - k \cdot I_\mathrm{b}$, with $k = V_f/V_b = -14/3$. See text for details.

However, in the context of the present study, the total charge associated with the conformational change of a large population of channel proteins was to be determined. In such case the state of the population has to be characterized by a probability distribution. A current at a certain transmembrane voltage then only reflects the fraction of channels that are open at a point in time. Consequently, it has to be ensured that the voltages to which the oocyte is clamped start around the resting state of the channels (where the vast majority of channels are closed) and then step to a region, where the probability of the channels to be in their open configuration approaches unity.

Figure 2.3 illustrates a standard pulse protocol to achieve this. Initially, the oocyte is clamped to a potential difference of $-100\,\mathrm{mV}$. In this region, most of the ion channels are in their closed conformation. Then a step pulse of 20 ms duration to $+40\,\mathrm{mV}$ (forward

pulse) is applied, leading to the opening and the successive closing of the majority of the channels. The current $I_f$ (forward current) that is measured during this pulse is comprised of a capacitive current $I_{f_c}$, a linear leak current $I_{f_l}$ and the gating current $I_g$:

$$I_f = I_{f_c} + I_{f_l} + I_g \tag{2.11}$$

The capacitive current $I_{f_c}$ and the linear leak current $I_{f_l}$ are linearly dependent on the pulse height $V_f$:

$$\left.\begin{aligned} I_{f_c} &= k_1 V_f \\ I_{f_l} &= k_2 V_f \end{aligned}\right\} \quad \Longrightarrow \quad I_{f_c} + I_{f_l} = (k_1 + k_2) V_f$$

where $k_1$ and $k_2$ are the proportionality factors. Together with equation 2.11 the gating current takes on this simple form:

$$I_g = I_f - (k_1 + k_2) V_f \tag{2.12}$$

After application of the backward pulse, the oocyte is clamped to $-150\,\mathrm{mV}$ and a pulse of the same duration to $-180\,\mathrm{mV}$ is applied (backward pulse). In this region, the ion channels are in their closed state and the measured current $I_b$ (backward current) is the sum of capacitive and leak currents:

$$I_b = I_{b_c} + I_{b_l} = (k_1 + k_2) V_b \quad \Longrightarrow \quad (k_1 + k_2) = \frac{I_b}{V_b}$$

where $I_{b_c}$ and $I_{b_l}$ are the capacitive and leak currents during the backward pulse. Together with equation 2.11 the gating current can be expressed as the difference between the forward and the backward current, where the latter is scaled by the ratio between the pulse heights of the forward and backward pulses:

$$I_g = I_f - I_b \frac{V_f}{V_b} \quad \Longrightarrow \quad Q = \int I_g \,\mathrm{d}t$$

where $Q$ is the sum of the gating charges of all channels and simply follows by integrating the gating current $I_g$. All gating current measurements of the present study have been performed with this or a very similar pulse protocol. A detailed description can be found in the manuscript under *Gating charge measurements* on page 63.

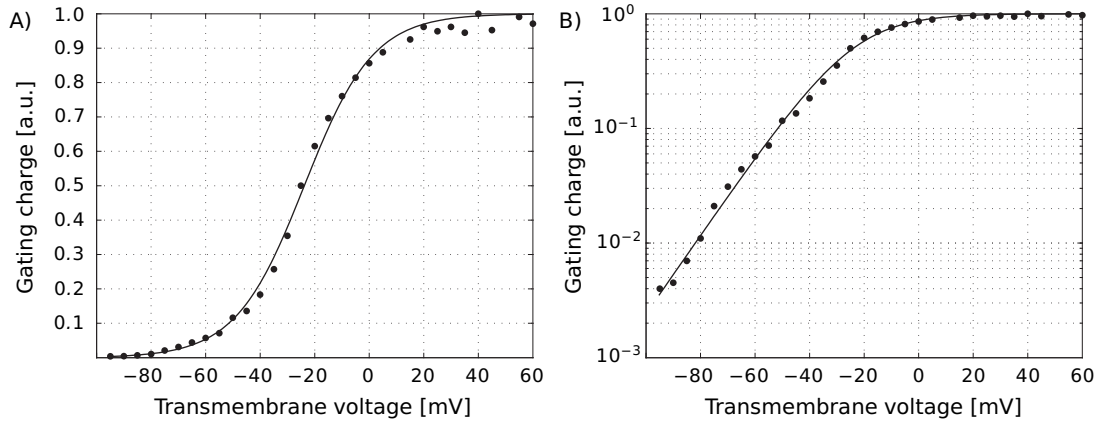


Figure 2.4: A) The gating charge of a large population of $Na^+$ channels as a function of transmembrane voltage. B) Same as in A with logarithmic scaling.

Figure 2.4 illustrates the voltage dependence of the gating charge. The gating current of a large population of $Na^+$ channels was determined by the method explained in the preceding section. The typical steep voltage dependence with its steepest region around $-20\,\mathrm{mV}$ can be seen.

## 2.3 Determination of the number of expressed channels

In order to estimate the number of channels that were expressed in the oocyte's membrane, a novel approach was developed: The channel proteins were marked with a certain number of fluorophores in order to use fluorescence intensity as a measure of the number of channels. Enhanced green fluorescent proteins (eGFP) were genetically encoded and inserted into the channel protein, guaranteeing specific marking of the channel. Because this method is essentially based on the phenomenon of fluorescence and the technique of fluorescence microscopy, an overview of the two subjects will be given in the next section. Thereby, the properties of GFP and eGFP will be discussed in greater detail.

### 2.3.1 Fluorescence microscopy

Fluorescence microscopy is a powerful tool to examine biological samples. It allows – unlike many other microscopic methods – to observe samples in their natural environments in aqueous solution or even in vivo. Many biological samples are optically transparent

and are therefore not directly detectable by conventional light microscopes[12]. By staining these samples with fluorescent labels, the corresponding binding sites act as sources of light, which can readily be detected. Fluorescence facilitates a tremendous range of applications, among them distance measurements between binding sites of proteins by fluorescence resonance energy transfer (FRET), the exploration of interactions between solvent molecules and fluorophores, or the determination of diffusional properties of labeled solvents. In all of these methods, the fluorescence signal acts as a reporter of site–specific reactions in biological systems. In the last decade, this concept has greatly been expanded by the possibility to detect the fluorescence emission of single fluorophores. This provides new insights into the structure and the properties of complex biomolecules on the molecular level. In conjunction with fs– to ps–pulsed lasers, time resolved measurements can be performed with high precision which allows to gain information about the structure and flexibility of a molecule. For a comprehensive review on fluorescence and its various forms of implementation see [60].

## Fluorescence

The various processes involved in the absorption and emission of photons in a fluorophore can be illustrated in a Jablonski diagram (see figure 2.5). An electronic state of the fluorophore is characterized by its main quantum number $n$ and whether it is in a singlet ($S$) or triplet ($T$) configuration. In each main quantum state an electron can occupy one of the closely spaced vibrational states.

At room temperature the electrons occupy the ground state $S_0$. Within femtoseconds the absorption of a photon $\gamma_{ex}$ can raise an electron into one of the excited singlet states ($S_0 + \gamma_{ex} \rightarrow S_n; n = 1, 2, \ldots$). With photon energies of a few eV – which is the energy of a photon in the visible part of the spectrum –, this means in most cases a transition to $S_1$ or $S_2$. Two processes or a combination of both can now occur: by internal conversion the electron can fall from a higher to a lower singlet state ($S_m \rightarrow S_n; m > n \geq 1$) or it can relax to the lowest vibrational state within an excited state by vibrational relaxation. Both of these processes are non–radiative and take place within $10^{-14}$ – $10^{-11}$ s. The excess energy is transferred to surrounding molecules as vibrational energy. As soon as the electron is in

[12] However, regions of varying refractivity may be imaged for example by *phase contrast microscopy* or *differential interference contrast microscopy*.

the lowest vibrational state of the first excited state, it can fall back to the ground state within $10^{-9}$ – $10^{-7}$s to one of the vibrational ground states by the emission of a photon $\gamma_{em}$ ($S_1 + \gamma_{em} \rightarrow S_0$). This process is called *fluorescence*.

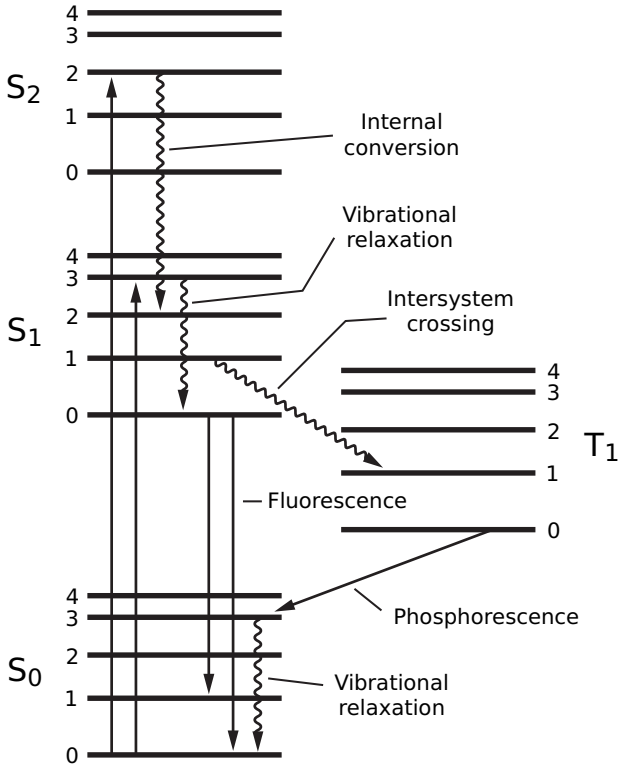


Figure 2.5: Jablonski diagram. Four principal energy states of a hypothetical fluorophore, and their respective vibrational states: three singlet states $S_0, S_1, S_2$ and one triplet state $T_1$. Solid arrows denote transitions accompanied by the absorption or emission of a photon, while wavy arrows denote non–radiative transitions. For the sake of clarity, rotational energy states are disregarded in this diagram.

Because the lifetime of the excited state (the time the electron spends in the lowest vibrational energy level of $S_1$) is longer than the times involved in internal conversion and vibrational relaxation by several orders of magnitude, the final transition to the ground state almost always starts from the lowest vibrational state of $S_1$. Therefore, the fluorescence emission spectrum[13] reflects the vibrational states of the ground state $S_0$. Since the energy spacings of the vibrational states of the singlet states $S_0$ and $S_1$ are very similar, the excitation spectrum of a fluorophore often looks like a mirror image of the emission spectrum (see figure 2.7A and B). Differences arise primarily from the fact that electrons are not solely raised to the first but also to the second excited state. In honor to Sir G. G. Stokes who discovered this phenomenon in 1852 [61], the energy difference between the excitation and the emission maximum is called *Stokes shift*. This difference allows to separate the emission and excitation light by optical filters and represents the basic principle involved in fluorescence microscopy.

Alternatively, the electron can undergo the non–radiative spin converting transition to

[13]The excitation spectrum is the relative fluorescence emission intensity as a function of the wavelength of the excitation light; the emission spectrum is the spectrum of the fluorescence emission, when the fluorophore is excited at the wavelength of the maximum of the excitation spectrum. Unfortunately, this procedure is not always followed and while in most cases the emission spectrum is rather independent of the excitation wavelength, in some cases substantial differences can occur.

the metastable triplet state ($S_1 \rightarrow T_1$) and finally down to one of the vibrational ground states ($T_1 + \gamma_{ph} \rightarrow S_0$). The latter is again accompanied by the emission of a photon $\gamma_{ph}$ and is termed *phosphorescence*. Because this transition is forbidden by the selection rules for optical transitions, fluorescence usually is favored over phosphorescence by several orders of magnitude. Time scales for phosphorescence range from milliseconds to hours.

### Fluorescence microscopy setup

A standard fluorescence microscopy setup is shown in figure 2.6. A mercury lamp provides the excitation light which is collimated and directed onto the excitation filter. This filter selects the part of the spectrum that overlaps maximally with the excitation maximum of the fluorophore under investigation, while minimally overlapping with the emission spectrum. The light is then reflected at the surface of the dichroic mirror, passes the microscope objective and excites the sample. The fluorescence light travels back through the microscope objective and passes the dichroic mirror which is nearly transparent for the redshifted fluorescence light (for the transmission spectra of the filters see figure 2.7). The emission filter blocks the remaining emission light (mainly reflections inside the microscope) before illuminating the CCD chip. Selection of the optimal filters is crucial to maximize detection efficiency and to minimize crosstalk.

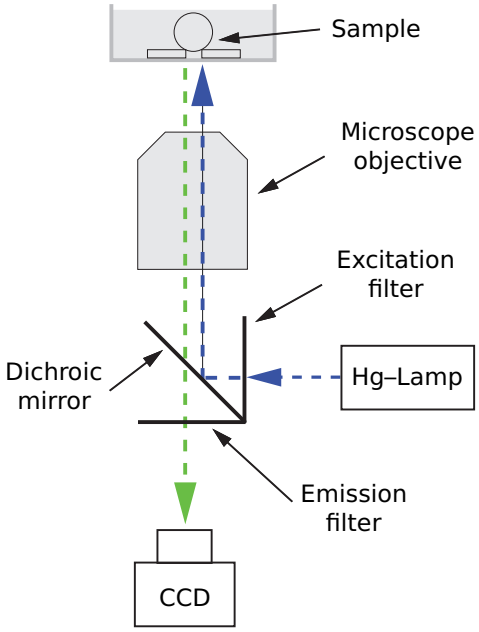


Figure 2.6: Fluorescence microscopy setup.

## 2.3.2 The green fluorescent protein

The *green fluorescent protein* (GFP) is a fluorophore of 238 amino acids which occurs naturally in the jellyfish *Aequorea victoria* and which was discovered in 1962 by Shimomura and colleagues [62]. In the following years, the emission spectrum of GFP was characterized by Johnson and colleagues [63] in 1962, the excitation spectrum and the fluorescence quantum yield by Morise and colleagues in 1974 [64] and the molecular weight by Prendergast in 1978 [65].

One of the most important steps with respect to the usefulness of GFP as a fluorescent marker in the biological sciences was the cloning and sequencing of the GFP gene by Prasher and colleagues in 1992 [66]. This led to the expression of GFP in *Escherichia coli* by Inouye and Tsuji in 1994 [67] and by Chalfie et al. in 1994 [68], clearly demonstrating that the expressed gene can function in organisms other than *Aequorea victoria*.

In 1970, Werner Arber, Daniel Nathans and Hamilton Smith won the Nobel prize in medicine *"for the discovery of restriction enzymes and their application to problems of molecular genetic"* [69], and in 1973 Cohen and colleagues expressed a *plasmid*[14] in bacteria [70]. This was the advent of recombinant DNA technology which allows for high replication rates of DNA: 1) The DNA of the gene of interest is isolated and inserted into the plasmid, 2) the plasmid is inserted into a cell where it replicates and 3) the cells containing the modified plasmids are selected. Furthermore, multiple strands of DNA – each coding for a different protein – can now be constructed and replicated. For the current study, fusion constructs consisting of an ion channel and a varying number of eGFP proteins were produced. Unlike conventional staining methods – which always suffer from a certain extent of unspecific bindings – this procedure allows to target a precise position in the primary structure of a protein.

### wtGFP and eGFP properties

The naturally occurring *wild type GFP* (wtGFP) has two excitation peaks. One at 395 nm and one at 475 nm, the latter being about three times smaller than the first one (see figure 2.7, A). Excitation at 395 nm leads to an emission peak at 508 nm, while excitation at 475 nm gives rise to an emission peak at 503 nm [71].

The emission spectrum reflects the energy differences of the vibrational states of the ground state $S_0$ – and hence is independent of the excitation wavelength. This indicates the presence of two chemically distinct forms of wtGFP. When excited at 488 nm over a time span of one hour, the emission peak of wtGFP at 395 nm decreases by 18 %, while the one at 475 nm increases by 40 % [72]. This photoconversion of the fluorophore can severely complicate the data analysis.

[14] A plasmid is a circular strand of DNA found in bacteria or yeast cells which contains all genetic information to direct DNA replication.

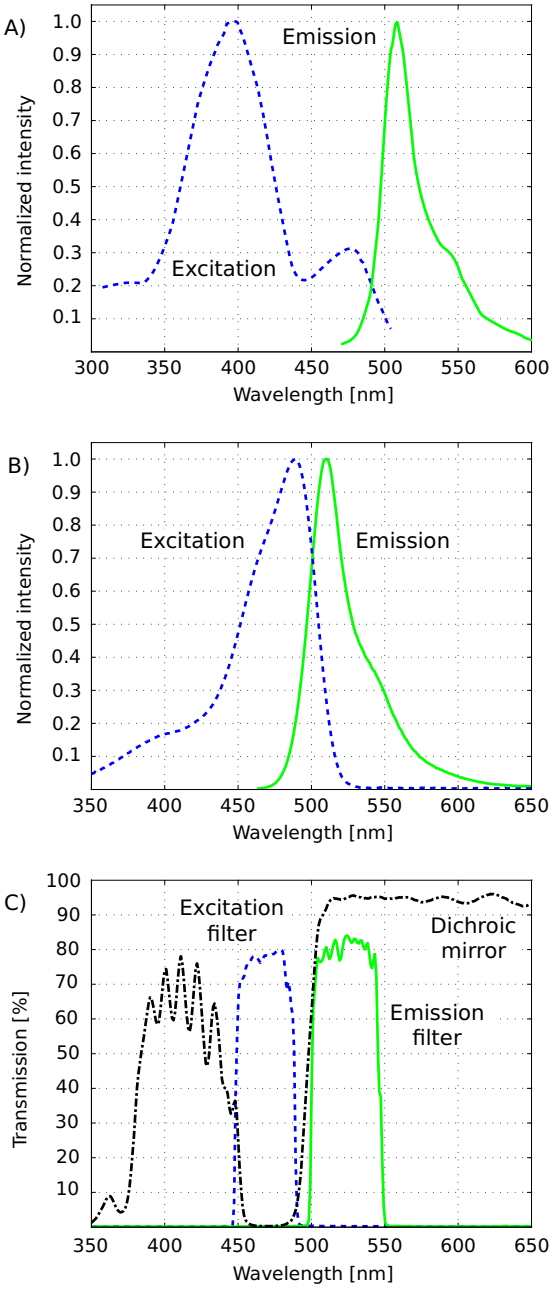


Figure 2.7: GFP spectra and filter transmission. A) Excitation and emission spectrum of wild type GFP (taken from [73]). B) Excitation and emission spectrum of eGFP [72]. C) Transmission of the filters of the eGFP filter block #41017 from Chroma Technologies, USA.

In 1995, Heim and colleagues [74] constructed a point mutation, where they changed the serine of the primary protein structure of wtGFP to threonine (S65T). This mutant shows only one peak in the excitation and in the emission spectrum, respectively. Peak excitation is located at 490 nm and emission has its maximum at 510 nm. Besides these simple spectral properties, this mutant has another major advantage over wtGFP: the molar extinction coefficient of the S65T mutant at 490 nm is about 5.5 times higher than the one of wtGFP at 475 nm and about two times higher than that of wtGFP at 395 nm. Since the fluorescence quantum yield is about the same (0.77 for wtGFP and 0.68 for S65T GFP), this results in about five times larger fluorescence signals. With an additional point mutation, where the original amino acid phenylalanine at position 64 was changed to leucine (F64L/S65T) by Yang et al. [75], another property of GFP could be optimized. The correct protein folding of this GFP variant during expression seems to be rather independent of temperature: while the efficiency of correct folding at 28°C was identical for both mutants, S65T had a three times lower folding efficiency at 28°C when compared to F64L/S65T [72]. For its superior properties this construct was named *enhanced GFP* (eGFP, see figure 2.7, B) and has rapidly become a standard tool in the studies of biological samples. Incorrectly, the S65T mutation is sometimes also referred to as eGFP.

While fluorescence emission of wtGFP is very stable for pH 6–8, the emission of eGFP drops from 100 % at pH 8 to 85 % at pH 7 and down to 75 % at pH 6. At pH 4 both of the GFP variants exhibit less than 20 % of their original emission. Even though in most applications it is desirable to have high absorption coefficients and emission light yields independently from the surrounding medium, the pH–dependence of eGFP allows to use it as a pH probe (see for example [76–78]).

Photobleaching is the irreversible photoinduced destruction of a fluorophore. This is an important parameter that needs to be taken into account for correct data interpretation. Most fluorophores (among them eGFP) show a single exponential decay of fluorescence intensity over time. In contrast to this behavior, when a confined volume of wtGFP is excited at 488 nm, fluorescence intensity initially increases, reaches a maximum after about 8 min and then also decreases. The initial increase is a consequence of the photoconversion of one to another fluorescent state as discussed earlier. Again, this behavior can make quantitative interpretation of data difficult, while a single exponential can easily be taken into account. Although there is quite some disagreement over the exact process underlying photobleaching, it has been repeatedly proposed that the triplet state $T_1$ or a higher order triplet state ($T_n; n > 1$) lies at its origin [80–83].

An interesting procedure to reduce the time a fluorophore spends in the triplet state $T_1$ was suggested by Mondal [84]: if, after a first excitation pulse, a depletion pulse is applied that depletes the triplet state $T_1$ and thereby repopulates the ground state $S_0$, the second excitation pulse can excite fluorophores that would otherwise still be in the triplet state $T_1$. Therefore, not only the extent of photodamage is reduced (in case the $T_1$ state is the origin of photodamage), but also fluorescence light yield is increased. This is of particular importance in single mol-

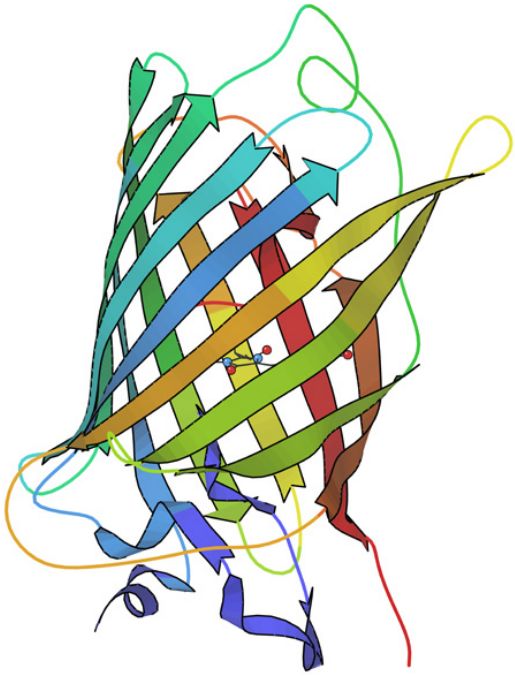

Figure 2.8: Structure of a GFP protein with mutations at positions F64L, S65T, F99S, M153T and V163A [79] (Protein Data Bank entry: 2b3q). The fluorophore is at position 64/65/66 and is located in the center of the barrel–like structure of the protein.

ecule experiments since the fluorescence signal completely vanishes while the fluorophore is in the triplet state (a phenomenon called *blinking*).

While in most applications bleaching poses an inherent limitation, other techniques have been developed that make use of the bleaching properties to gain information about the kinetics of a fluorophore or of biomolecules attached to it. For example, bleaching can be used to determine diffusion constants and the mobility of fluorophores in solution or to measure the binding and dissociation rates between biomolecules [85–87].

The triplet state $T_1$ of eGFP can also be the cause of damage to the surrounding structures because *singlet oxygen*[15] is produced by energy transfer from the triplet state of eGFP [88, 89]. Singlet oxygen is very reactive and damages primarily cysteine, histidine, methionine and tryptophan residues of proteins [90].

The crystal structure of wtGFP was solved independently by two labs in 1996 [91, 92]. The fluorophore of wtGFP is formed by the amino acids serine, tyrosine and glycine at positions 65/66/67. It is embedded in a barrel–like structure inside the protein, that protects it from collisional quenching (see figure 2.8).

### 2.3.3 Finding a measure of the number of expressed channels

Channels tagged with fluorophores provide a straightforward method to approximate the number of expressed channels by quantifying the fluorescence intensity of excited fluorophores. If the number of fluorophores per channel protein is constant, fluorescence intensity is linearly dependent on the number of channels (as long as the excitation intensity is below the saturation threshold of the fluorophore). Channel mutants which have fluorescent proteins genetically encoded in their structure are perfectly suitable for this task, because the stoichiometry between channel proteins and fluorophores is always at a fixed value[16].

Figure 1 of the manuscript on page 62 illustrates the constructs that were used in the present study. Because the $K^+$ channel is a homotetramer [93], the insertion of the coding sequence of an eGFP protein leads to the expression of four eGFP molecules per channel, while only one eGFP molecule per channel will be present in the $Na^+$ channel. By analogy,

[15] Singlet oxygen is the first excited state of molecular oxygen $^1O_2$. Contrary to most other organic compounds, the ground state of molecular oxygen is a triplet state and the first two excited states are singlet states.

[16] Obviously, this is true only if both the channel protein and the fluorophore are still fully functional. This aspect is dealt with in the section *Discussion* of the manuscript on page 69.

the insertion of $n$ eGFP coding sequences leads to $4n$ eGFP proteins in a $K^+$ channel and to $n$ eGFP proteins in a $Na^+$ channel. $K^+$ channels with up to 12 eGFP molecules and $Na^+$ channel with up to 4 eGFP molecules were used. The eGFP molecules were inserted at the C–terminal of the respective channels to minimize interference with the normal functioning of the channel.

After expression of the channel proteins in the oocytes, the oocytes were excited and imaged on the fluorescence microscope described in section 2.3.1 and the corresponding image was recorded by a CCD camera. After this, the total gating charge was determined by two electrode voltage clamp.

Substantial difficulties arose from the large autofluorescence of the oocytes (see figure 5 of the manuscript on page 66) and from the large volume of the oocytes ($\varnothing \simeq 1\,\mathrm{mm}$). Fortunately, certain regions of the oocyte are relatively free from contamination by autofluorescent substances. A MatLab routine was developed that identifies these regions on the CCD image and limits data analysis to them alone. This procedure allows to determine a measure for the number of ion channels that are expressed in the oocyte. The manuscript covers this method in full detail and discusses the principal sources of autofluorescence (see section *Autofluorescence* on page 64).

## 2.4 Manuscript: Gating charge of $K^+$ and $Na^+$ ion channels

The following pages are a reprint of the article:

**More gating charges are needed to open a *Shaker* $K^+$ channel than are needed to open a rBIIA $Na^+$ channel**

By Tamer M. Gamal El–Din*, Dominik Grögler*,
Claudia Lehmann, Hansjakob Heldstab and Nikolaus G. Greeff

Biophysical Journal, 95(3):1165–1175, 2008

* Dominik Grögler and Tamer M. Gamal El–Din contributed equally to this work.

Biophysical Journal Volume 95 August 2008 1165–1175 

# More Gating Charges are Needed to Open a *Shaker* $K^+$ Channel than are Needed to Open an rBIIA $Na^+$ Channel

Tamer M. Gamal El-Din, Dominik Grögler, Claudia Lehmann, Hansjakob Heldstab, and Nikolaus G. Greeff
University of Zürich, Institute of Physiology, 8057 Zürich, Switzerland

ABSTRACT This study presents what is, to our knowledge, a novel technique by means of which the ratio of the single gating charges of voltage-gated rat brain IIA (rBIIA) sodium and *Shaker* potassium ion channels was estimated. In the experiment, multiple tandems of enhanced green fluorescent protein were constructed and inserted into the C-terminals of $Na^+$ and $K^+$ ion channels. cRNA of $Na^+$ and $K^+$ ion channels was injected and expressed in *Xenopus laevis* oocytes. The two electrode voltage-clamp technique allowed us to determine the total gating charge of sodium and potassium ion channels, while a relative measure of the amount of expressed channels could be established on the basis of the quantification of the fluorescence intensity of membrane-bound channels marked by enhanced green fluorescent proteins. As a result, gating charge and fluorescence intensity were found to be positively correlated. A relative comparison of the single gating charges of voltage-gated sodium and potassium ion channels could thus be established: the ratio of the single gating charges of the *Shaker* potassium channel and the rBIIA sodium channel was found to be $2.5 \pm 0.4$. Assuming the single channel gating charge of the *Shaker* $K^+$ channel to be $\sim$13 elementary charges (well supported by other studies), this leads to approximately six elementary charges for the rBIIA sodium channel, which includes a fraction of gating charge that is missed during inactivation.

## INTRODUCTION

Voltage-gated ion channels are the elementary units underlying the generation and propagation of biological electrical signals. The voltage sensitivity of voltage-gated ion channels depends mainly on the number of gating charges that move along the electric field of the membrane. Estimation and comparison of the number of gating charges of different voltage-gated ion channels were of interest in many articles. Hodgkin and Huxley (1) had originally proposed that at least 4.5–6 elementary charges fully move across the membrane electric field to open a sodium channel. More recent methods give values at $\sim$13 elementary charges for the *Shaker* $K^+$ channel and 5–16 for different types of $Na^+$ channels.

Among these voltage-gated channels, the $K^+$ channels which, due to their simpler structure and kinetics are more easily studied, received most attention. Many studies estimated the number of ion channels in a given sample and correlated it with the total gating charge to determine how many charges move per channel during the gating process. Different techniques were used to measure the number of channels. Aggarwal and MacKinnon (2) expressed *Shaker* $K^+$ channels in *Xenopus laevis* oocytes and used a radiolabeled $\alpha$-KTx scorpion toxin that blocks the channel pore with a stoichiometry of 1:1. Division of the total radioactivity by the specific activity of the radiolabeled toxin allowed them to estimate the number of channels. They correlated this number with the total gating charge measured by the two-electrode voltage-clamp technique from the same oocyte, and thus calculated the number of gating charges per channel, which was found to be 13.6 elementary charges. Noceti et al. (3) estimated the number of gating charges per channel by using the limiting slope analysis of the conductance-voltage relationship and by variance analysis. They found that 13 elementary charges are involved in the gating process of the *Shaker* $K^+$ channel and 8.6 elementary charges in the $Ca^{2+}$ channel. Using the same method, Zagotta et al. (4) estimated 12–16 elementary charges for the *Shaker* $K^+$ channel, whereas Schoppa et al. (5) and Islas and Sigworth (6) estimated this number to be 12.5.

$Na^+$ channels are less often studied and the presently available data show a large spread for the estimated single gating charge. Conti and Stühmer (7) found that the activation of a single rBIIA sodium channel occurs in two-to-three brief packets, each carrying an equivalent of $\simeq$2.3 elementary charges. This is still in the range of the original figure given by Hodgkin and Huxley (1). Sheets and Hanck (8) estimated the lower limit of the gating charge per channel of the human cardiac $Na^+$ channel hH1a to be 5.2 elementary charges. Single channel recordings of the skeletal muscle $Na^+$ channel enabled Hirschberg et al. (9) to estimate that at least 12 elementary charges are involved in the gating process. They measured the open probability as a function of membrane potential, which gave them a quantitative indication of the number of gating charges that move through the electric field when the channel switches from the closed to the open state. The measurements done by Kuzmenkin et al. (10) have indicated that the bacterial sodium channel NaChBac needs 16 elementary charges for activation.

The aim of this study is the direct comparison of the single channel gating charge of the *Shaker* $K^+$ and the rBIIA $Na^+$

*Submitted February 21, 2008, and accepted for publication March 26, 2008.*

Tamer M. Gamal El-Din and Dominik Grögler contributed equally to this work.

Address reprint requests to Nikolaus G. Greeff, E-mail: greeff@physiol.unizh.ch.

Editor: Dorothy A. Hanck.


0006-3495/08/08/1165/11 $2.00

doi: 10.1529/biophysj.108.130765

channels and to derive an estimate for the single channel gating charge from the better known $K^+$ to the $Na^+$ channels by a new approach. To do so, enhanced green fluorescent protein (eGFP) was inserted into the C-terminal of $K^+$ and $Na^+$ channels on the cDNA level and the resulting channels were studied in *Xenopus laevis* oocytes. Because the $K^+$ channel is a homotetramer, it has four identical nonlinked subunits, each with one C-terminal, whereas the $Na^+$ channel has four homologous and covalently linked domains (DI–DIV) and only one C-terminal. As a consequence, insertion of the coding sequence of one eGFP molecule into the C-terminal coding sequence of a $K^+$ channel will result in the expression of four eGFP molecules per $K^+$ channel (one per each domain), whereas the analogous insertion into the $Na^+$ channel will lead to the expression of only one eGFP molecule per channel (see Fig. 1). Multiple eGFP tandems were constructed and inserted into the C-terminal of the $Na^+$ and $K^+$ channels. The fluorescence intensity of the incorporated eGFP molecules was measured and correlated with the gating charge obtained from the same oocyte. This correlation allows for the comparison of the relative size of the single gating charge between *Shaker* $K^+$ and rBIIA $Na^+$ channels. Preliminary work has been done and presented in the literature (11–13).

## METHODS

### Molecular biology

The cDNA coding for the nonconducting (W434F) *Shaker* $K^+$ channel with normal inactivation and for the rBIIA $Na^+$ channel was used. All were embedded in the high expression vector pBSTA providing flanking *Xenopus* $\beta$-globin and a T7 RNA promoter (14). The cDNA coding for the eGFP constructs was introduced into the C-terminal, for the $K^+$ channel at the existing *Spe*I-site at amino-acid (AA) 503/4 (following (15)), and for the $Na^+$ channel a new *Spe*I-site was introduced after AA1970 by changing the next bases T,C at 5910/11 to A,G. For expression in *Xenopus* oocytes, cRNA was obtained from linearized cDNA (*Not*I) by in vitro transcription and capping using T7-polymerase (mMessage mMachine Kit, Ambion, Austin, TX). The RNA concentration was checked spectroscopically and the integrity by RNase-free agarose gel electrophoresis.

For the construction of multiple tandem repeats of eGFP, the following strategy was developed and used. The basic cDNA for eGFP was obtained from a commercially available vector (Genbank # U76561, Clontech Laboratories, Mountain View, CA), which was modified by changing the start and end to *Spe*I-sites (5′-a/ctagtgtgag- - - -eGFP- - - -gtaca/ctagt-3′), i.e., adding 717 basepairs (bps) when inserted into a host frame. A special 14-AA linker was used to join multiple tandem eGFPs with a protease-resistant AA sequence (RHGTGSTGSGSSGS, based on information for a 12 AA linker from (16)), where the 5′-end was an *Xba*I overhang (CTAGA, AGA coding for the R) and the 3′-end was an *Xba*I overhang (TCTAG, TCT coding for the last S). In addition, the *Xba*I site on the 3′-end was capped by a short stretch of bases with a blunt end, such that, in the next ligation step, the linker would only bind with its 5′-end to eGFP; this cap was removed later by *Xba*I. This linker was ligated to the 3′-end of the eGFP, generating a hybrid *Spe*I/*Xba*I connection; this was achieved by mass ligation of eGFP and linker DNA (the linker not phosphorylated). Then the resulting dimers (linker-eGFP-eGFP-linker) were separated from a preparative gel and cut with *Spe*I, which resulted in an eGFP-linker pool where 50% had the correct orientation. These fragments (759 bps) were inserted into a vector, and from the clones, the correct combination was identified by sequencing, and used as the element for the multiple tandem ligations, as follows. The elements were mass-ligated, and then cut by *Spe*I and *Xba*I. Only the desired hybrid connections of the linker 3′-end *Xba*I to the next eGFP 5′-end *Spe*I were preserved, and the unwanted *Spe*I or *Xba*I connections cut. Fig. 2 shows the preparative gel with the mono-, di-, tri-, etc., tandem repeats of the eGFP-linker as well as the ring forms of the mono- and probably the di-sequence. The tandems were stored in a bluescript vector prepared with *Spe*I and *Xba*I for later use in the channel cDNA. (For further verification of the tandem inserts in the channel cDNA, see Results.)

### Oocyte extraction and RNA microinjection

Large frogs (Nasco, Fort Atkinson, WI) were anesthetized in 2 g/l MS-222 (ethyl 3-aminobenzoate methanesulfonate salt; cat. No. A5040-100G, Sigma, St. Louis, MO) for 10–15 min and then operated to extract the oocytes. The extracted stage V–VI oocytes were put into calcium-free OR II (2 mM KCl, 1 mM $MgCl_2$, 82.5 mM NaCl, 20.0 mM HEPES, and titrated with 0.5 M Tris base to reach pH 7.3) to which 50 $\mu$g/ml gentamicine sulfate and 5 $\mu$g/ml doxycycline hydrochloride were added. The oocytes stayed there for $\simeq$30 min until the end of the operation. To remove follicular cells, the oocytes were then put in a solution of calcium-free OR II and collagenase (No. C-9891, 2 mg/ml, Sigma) until approximately half of the follicular cells were

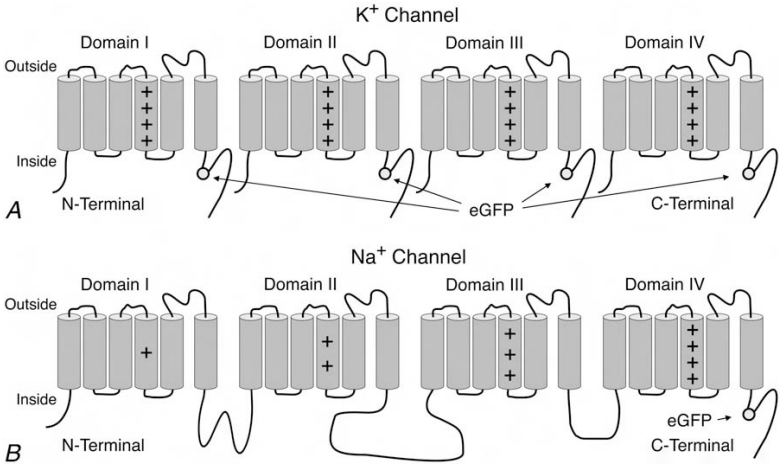


FIGURE 1 (*A*) $K^+$ channel construct with one eGFP molecule at the C-terminal of each domain (KG1). The eGFP is inserted at the existing *Spe*I site (AA 503/4). (*B*) $Na^+$ channel construct with one eGFP molecule at the C-terminal (NaG1). The eGFP is inserted at a newly created *Spe*I site, which was introduced after AA 1970 by changing the next bases T,C at 5910/11 to A,G. The charge symbols do not reflect the actual number of positive charges in each S4, but the approximate proportional distribution instead.

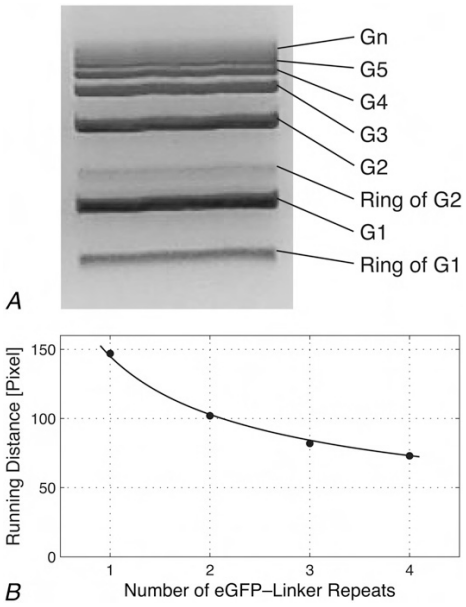


FIGURE 2 (*A*) Preparative agarose gel and analysis of the multiple tandem repeats of the element /*Spe*I-eGFP-*Spe*I//*Xba*I-Linker-*Xba*I/ after mass ligation of this element and recutting by *Spe*I and *Xba*I: Linear forms G1–G4 were prepared for later use; ring forms and larger tandems were discarded. (*B*) Plot of running distances of G1–G4 measured in pixels from the gel photo versus the number of ligated tandem repeats. The solid line is a power fit to the data.

digested (after ≃60 min). To remove all of the leftover collagenase after defolliculation, oocytes were washed two times in OR II and two times in modified Barth's solution (MBS: 88 mM NaCl, 1 mM KCl, 2.4 mM $NaHCO_3$, 0.82 mM $MgSO_4$, 0.33 mM $Ca(NO_3)_2$, 0.41 mM $CaCl_2$, 20.0 mM HEPES and titrated with 0.5 M Tris base to reach pH 7.3) to which 50 $\mu$g/ml gentamicine sulfate and 5 $\mu$g/ml doxycycline hydrochloride were added. Oocytes were then kept in MBS at 18°C. Twenty-four hours later, each oocyte was microinjected with 50 nl solution, which contained 30–50 ng cRNA. After injection, oocytes were kept at 18°C in MBS, which was changed daily. In this way, the oocytes stayed intact for 10–14 days.

## Gating charge measurements

Five-to-ten days past injection, gating currents were recorded using two-electrode voltage-clamp (DAGAN CA-1, Minneapolis, MN and Turbo-Tec05, NPI-Electronics, Tamm, Germany), and filtered at 5 kHz with an eight-pole Bessel filter. Intracellular agarose cushion electrodes (17) were filled with 3 M KCl solution, and had a resistance between 100 and 200 k$\Omega$. To measure $K^+$ gating currents, oocytes were clamped to a holding potential of −100 mV at temperatures ranging from 12 to 15°C in MBS (pH 7.3). A pulse protocol was applied to the clamped oocytes as follows: Depolarizing pulses from −100 to +60 mV in steps of 20 mV and a hyperpolarizing pulse from −150 to −180 mV. $Na^+$ gating currents were measured by clamping the oocyte to −100 mV. Depolarizing pulses ranged from −100 to +60 mV and the hyperpolarizing pulse went from −120 to −150 mV. For measurements on $K^+$ as well as on $Na^+$ channels, the hyperpolarizing pulses had the same duration as the depolarizing pulses. Linear capacitance and linear leak currents were removed by subtracting scaled-up versions of the currents that resulted from the hyperpolarizing pulses from the currents that resulted from the depolarizing pulses as described earlier (14).

In case of measuring $Na^+$ gating currents, suppression of ionic currents was achieved by adding tetrodotoxin to the bath solution to reach a concentration of 2 $\mu$M. Examples of measured gating currents of different constructs are shown in Fig. 3. Note that even the $K^+$ channel construct with 12 eGFP molecules per channel shows normal gating currents, indicating that the functionality of the channel protein is kept intact despite the inserted eGFP molecules.

## Fluorescence microscopy setup

To get a relative measure of the number of ion channels that were incorporated in the membrane of the oocyte, the intensity of eGFP emission was quantified. Two conventional fluorescence microscopy setups with filter blocks optimized for eGFP were used for all fluorescence measurements:

Setup 1. Model No. IX71 with a UPlanFI 4× objective (NA = 0.13), from Olympus, Tokyo, Japan; and filter set model No. 41017

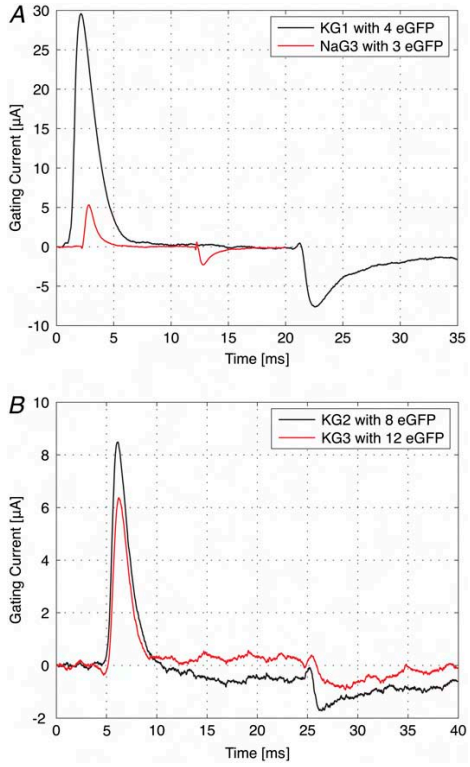


FIGURE 3 Gating currents of various channel constructs. (*A*) Gating current of a $K^+$ channel with four eGFP molecules per channel (KG1) and a $Na^+$ channel with three eGFP molecules per channel. Because of the higher expression level of $K^+$ channels, the corresponding gating current is approximately six times larger in amplitude than that of the $Na^+$ channel. Considering the slower kinetics of $K^+$ channels, the charge is ≃20 times larger. Pulse protocols: For KG1, holding potential is −100 mV; depolarizing pulse is from −100 to + 60 mV; and hyperpolarizing pulse is from −150 to −180 mV. For NaG3, holding potential is −100 mV; depolarizing pulse is from −100 to + 65 mV; and hyperpolarizing pulse is from −120 to −150 mV. (*B*) Gating currents of $K^+$ channels with eight and twelve eGFP molecules per channel (KG2 and KG3). Both channel constructs are still fully functional despite the insertion of eight and twelve eGFP molecules per channel, respectively. Pulse protocols were for both KG2 and KG3: Holding potential is –100 mV, depolarizing pulse is from −100 to + 60 mV, and hyperpolarizing pulse is from −150 to −180 mV. All applied pulses are sufficient to collect the full gating charge.

(excitation bandpass of 450–488 nm, transition wavelength of dichroic mirror of 498 nm; emission bandpass of 501–547 nm), from Chroma Technology, Rockingham, VT.

Setup 2. Model No. IM 35 with a Plan 6.3× objective (NA = 0.16), from Zeiss, Jena, Germany; a custom made lens at the camera port to demagnify the image; and filter set model No. XF100 (excitation bandpass: 456–489 nm, transition wavelength of dichroic mirror: 500 nm, emission bandpass: 519–560 nm) from Omega Optical, Brattleboro, VT.

The illumination source was a 100 W mercury lamp.

Images were acquired with a 12-bit charge-coupled device (CCD) camera (model No. A102f, Basler, Ahrensburg, Germany) with a pixel size of 6.45 × 6.45 $\mu m^2$ and an internal gain, which was controlled by a self-developed software to enable exposure times in a range from 1 ms to 4 s in steps of 1 ms. The internal gain was held as low as possible to maximize the signal/noise ratio. The camera offset was $\simeq$17 counts. All data are offset-corrected. The background was determined for every image and subtracted from the pixel counts.

## RESULTS

### Verification of tandem constructs

As mentioned in Methods, the single element of the eGFP-linker construct inserted into a bluescript vector was fully sequenced. For the multiple repeat tandems, sequencing is not easily possible, since a good sequencing run covers up to ~900 bps and the sequencing primer has to be outside the tandem region to prime only once. Thus, the following two tests were done for checking the multiple repeats for correct number and direction of insertion, although the way of construction already optimized the outcome.

Fig. 4 *A* shows one test for the plasmids pG1 to pG4 containing the tandem repeats and also the $K^+$ channel constructs KG1 to KG3. These constructs were cut with *Bsr*GI, which cuts near the 3′-end of eGFP at position 712 from 759. It can easily be seen that pG1 and KG1 would just be linearized giving the long band of 3711 or 5944, respectively (seen in the gel of Fig. 4 *A*). For higher tandems pGn or KGn, additional bands of 759 bps appeared with an intensity growing relative to the long band in proportion $n - 1$. Note that an inverted eGFP would create bands of 2 × 47 and 2 × 712. Fig. 4 *B* shows clearly that the intensity ratios increase linearly as expected and more steeply for pGn than for KGn. For this test, the intensities of the bands have been measured from a photo of the gel taken with the Basler CCD camera, which provided a linear range over 12-bit resolution. Fig. 4 *C* shows a second test on a gel for the NaG1–NaG4 constructs. The cDNA was cut with *Spe*I and *Sac*II close to either side of the tandem repeat. The lengths of the inserts were as expected. As shown in Fig. 4 *D*, the running distance increased according to the expected length of fragments, which confirms the number of tandem repeats.

### Fluorescence intensity measurements

Two intrinsic properties of the oocytes potentially make these measurements difficult: The oocytes show a strong cytoplasmic autofluorescence; and the distribution of channels over the surface is inhomogeneous.

### Autofluorescence

Autofluorescence is mainly caused by flavins within the cytoplasm (18). One-half of the oocyte is naturally covered with a dark pigment layer, which lies underneath the cellular membrane and masks the autofluorescence to a large extent (animal pole). On the other half of the oocyte, which is not pigmented (vegetative pole), autofluorescence is so high that it can hardly be distinguished from eGFP emission (see Fig. 5). However, a comparison of the intensity profiles of images of a noninjected control cell and an oocyte injected with $Na^+$ channel cRNA shows that, in the detection region, the cytoplasmatic contribution to the fluorescence signal is small in comparison to the signal originating from membrane-bound eGFP molecules. The difference is most striking on the animal pole, where the fluorescence signal in the border region of the control cell is as low as the background. In contrast to this, the fluorescence signal of the $Na^+$-injected oocyte shows a sharp peak. In the border region of the vegetative pole, the difference is not as obvious, but still substantial (see *inset* of Fig. 5).

Assuming a uniform distribution of fluorophores over the surface of the oocyte, the intensity of the fluorescence signal will be highest near the outermost part of the oocyte and decrease toward the center. The reason for this lies in the curvature of the oocyte: in an area near the circumference of the oocyte (see Fig. 6), a larger fraction of the surface will be projected onto a unit area of the CCD chip than it will be the case in an area near the center. Even though the cells have a nearly spherical shape, on the micrometer scale, the cellular membrane is characterized by a microvilous structure that extends toward the outside of the cell. Various studies report the length of these microvilli to be ~1 $\mu$m (19,20), 3–4 $\mu$m (21), and up to 10 $\mu$m (22,23). The confocal image in Fig. 6 clearly shows that the fluorescing region extends over a length of $\simeq$13 $\mu$m (full width at half-maximum). Therefore, a method based on a MatLab routine (The MathWorks, Natick, MA) was developed that detects the circumference of the oocyte and analyzes the fluorescence signal in a concentric ring of a width of 13 $\mu$m. This corresponds to a length of $\simeq$8.1 pixels on the Olympus microscope and to a length of $\simeq$6.6 pixels on the Zeiss microscope. This concentric ring is the projection of a spherical layer onto the CCD chip. Thereby the detectable signal originating from eGFP molecules bound to ion channels is maximized, while the contribution from autofluorescence is minimized (see Fig. 6 for details). With the diameter $D$ of the oocyte, the surface $A$ of this spherical layer can be calculated ($A = \pi \times D \times \sqrt{d \times (D - d)}$, where $d$ is the width of the concentric ring). With a typical diameter of 1.2 mm, this amounts to $\simeq$10% of the whole cell surface. Based on this fraction of the cell surface, the total of the measured pixel counts was extrapolated to the whole cell surface to allow for a quantitative comparison between oocytes. Note that for the relative comparison of the fluorescence intensity of two cells, it is not necessary to calculate the cell surface absolutely (including the enlargement by mi-

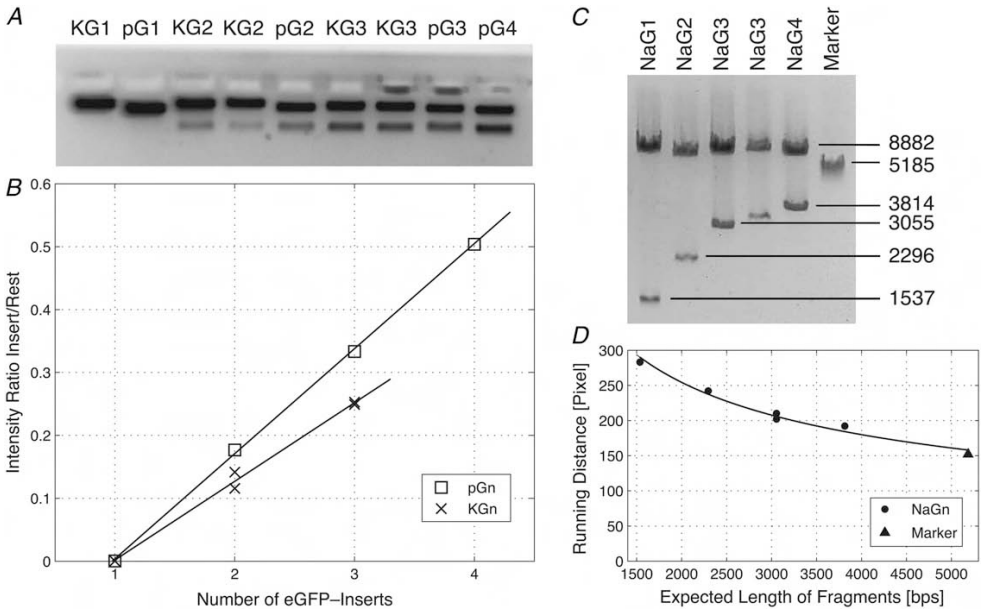


FIGURE 4 Gel analysis of plasmid- and channel-cDNA containing multiple tandem repeats inserted. (*A* and *B*) Gel and analysis of pG1–pG4 and KG1–KG3, as indicated (for KG2, two preparations of the same clone were tested; for KG3, two clones produced in parallel were tested which gave superimposing crosses in panel *B*; for NaG3, results from two subclones are shown). The constructs were cut with *Bsr*GI and analyzed as described in the text. Note that the gel shown was taken with a CCD camera with $\gamma = 0.5$, which enhances the weak bands, but the gel was also photographed with the Basler camera providing a linear ($\gamma = 1$) 12-bit resolution for the quantitative analysis shown in panel *B*. (*C* and *D*) Gel and analysis of NaG1–NaG4. DNA was cut with *Spe*I and *Sac*II, which cut close to either end of the tandem repeats. The expected lengths for the fragments with the insert are 1537, 2296, 3055, and 3814 bps for G1–G4 and for the remaining fragment 8882 bps; the last band is a linearized $K^+$ channel plasmid used for comparison (marker, 5185 bps). The solid line is a power fit to the data.

crovilli), but rather to ensure that all fluorescence originating from the marked ion channels is collected and reflects a relative measure of the total fluorescence intensity.

### Inhomogeneous distribution of channels

Because the distribution of channels over the surface of the oocyte is inhomogeneous, fluorescence intensities differ very much depending on the imaged area. To quantify the fluorescence from the whole cell—and thus get a relative measure of the number of expressed channels—the oocyte has to be imaged from several sides. With a ring width of 13 $\mu$m, the cell would have to be rotated by 24° between successive images to allow for the coverage of the whole cell surface, adding up to a total of 15 images per oocyte. Because the handling of the oocytes is quite delicate and because it is hard to achieve rotation in a precise and reproducible way, it is preferable to make as few images as possible while still getting a measure of the fluorescence intensity from the whole cell. Furthermore, because the exposure time of each image is between 0.5 and 4 s (depending on the expression level), photobleaching increasingly becomes an issue as more pictures are taken.

Various tests were made taking three, four, five or seven pictures per oocyte, rotating them by 120°, 90°, 72°, and 52° in-between images, respectively (see Fig. 6). For each set of images, the mean pixel count per image was calculated. When the same set of images was evaluated repeatedly, the measured mean pixel counts did not vary >10–15%, regardless of how many pictures were taken. For even numbers, the images can be reordered in such a way, that they are pairs of images taken from opposite sides (the second picture of each pair is taken after a rotation of 180°). Because these pairs image a similar area of the oocyte, it is advisable to take an odd number of images. As it turned out, taking only three images is better than taking four pictures, and the fluctuation of the mean pixel counts is ~10% (three images) as opposed to 15% (four images).

Fluorescence intensity was therefore quantified by taking three pictures per oocyte with a rotation of 120° in-between successive images for all subsequent measurements. These three images cover ≃30% of the whole cell surface.

### Illumination and detection properties

To account for a slow change in power of the Hg lamp, the lamp power at 488 nm was measured before each image acquisition. Images were then corrected for changes in illumination intensity. Furthermore, the properties of the CCD camera were characterized with respect to the shutter time and the internal gain. This allowed for a normalization of each image to a shutter time of 1 s and an internal camera gain of one. All data points were normalized in this way.

Because two setups were used for measuring the fluorescence intensity, an additional normalization factor was in-

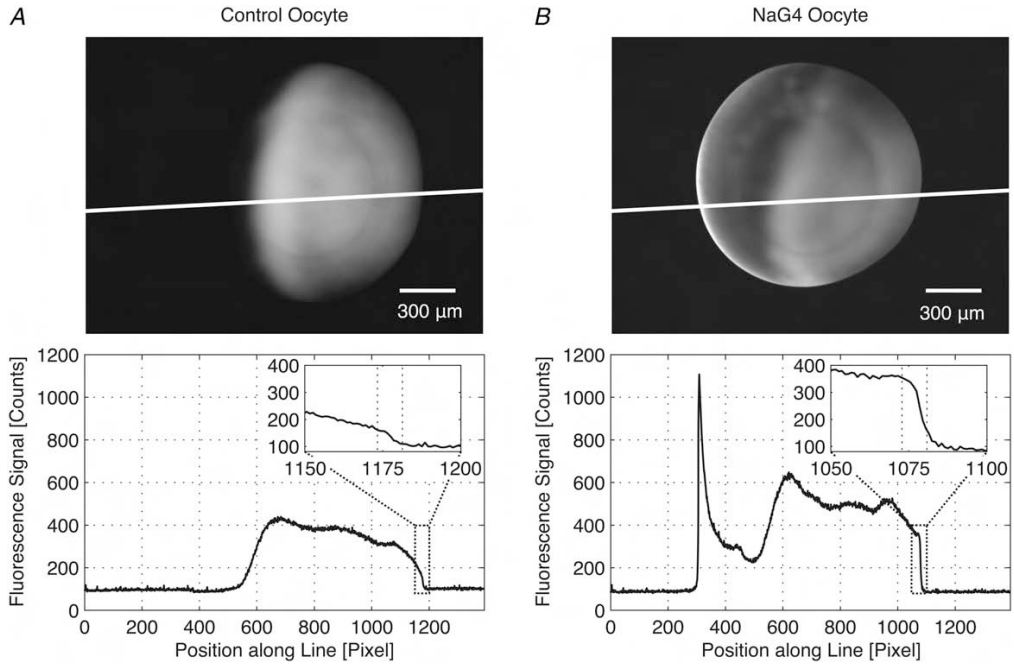


FIGURE 5 Comparison between a noninjected control oocyte and an oocyte injected with $Na^+$ channel cRNA (NaG4). The length of one pixel on the image corresponds to a length of $\simeq$1.6 $\mu$m on the sample. (*A*) The animal pole of the control oocyte (*left side* of the oocyte), which is covered with a dark pigment layer shows no fluorescence whereas the vegetative pole (*right side* of the oocyte) shows strong autofluorescence. (*B*) On the vegetative pole (*right side* of the oocyte), the autofluorescence intensity of the $Na^+$ injected oocyte is similar to the one of the control oocyte. At the edge of the animal pole (*left side* of the oocyte), however, a strong peak appears, which indicates the presence of channels in the cellular membrane. The insets show the border region of the two oocytes on the vegetative side. The two lines specify the width of the ring which is used for data analysis. The fluorescence intensity of membrane-bound channels leads to a sharp rise on top of the autofluorescence of the cytoplasm that disappears toward the border of the oocyte. Oocytes were placed on a glass slide into which a hole with a diameter of $\simeq$0.8 mm was drilled. This allowed for precise positioning of the oocytes. The edge of the hole can be seen as a circular shape in the inner part of the oocyte. Images are normalized to account for different illumination and imaging conditions. Normalization allows for a direct quantitative comparison between the two images.

troduced. To account for the different optics (objectives, filters and optical path), $\simeq$10 oocytes were imaged and their fluorescence intensity was measured on both setups. This comparison revealed that the Olympus setup yields $1.5 \pm 0.2$ times more counts than the Zeiss setup for an identical sample. All following data are normalized by this factor.

## Capturing the total gating charge

To be able to compare the gating charge per channel of $Na^+$ and $K^+$ ion channels, capturing the total gating charge of these channels was of prime importance. One method to measure gating charge is by integrating the total displacement current that results from applied pulses (see (2)). This yields a charge versus voltage ($Q$–$V$) plot which shows the linear (capacitive) and nonlinear (gating) components of the displaced charges (see Fig. 7). The nonlinear component of this plot is the gating charge. The voltage at which the charge starts to deviate from linearity indicates the beginning of gating charge movement. To find the potential at which this deviation occurs, many linear fittings were made in different voltage ranges at hyperpolarized potentials. Investigation of the residuals of these fittings lead to the conclusion that, in the voltage range from $-150$ to $-200$ mV, the charge movement for $K^+$ channels is purely capacitive and linear, without any contribution from gating charges.

On the basis of these findings, a conventional pulse protocol used for gating current experiments was adapted to the appropriate region of the hyperpolarizing pulse. The holding potential was set at $-100$ mV and pulses ranged from $-100$ to $+60$ mV in steps of 20 mV. Hyperpolarizing pulses ranged from $-100$ to $-130$ mV in a first experiment, from $-130$ to $-160$ mV in a second one and from $-150$ to $-180$ mV in a final experiment. Current traces resulting from the hyperpolarizing pulses were inverted, scaled-up according to the pulse height of the depolarizing pulses and subtracted from the current traces that resulted from depolarizing pulses. The difference trace is then due only to the movement of gating charges and integration reveals the total gating charge.

Compared to the first method, the measured gating charge was 10% lower with a hyperpolarizing pulse from $-100$ to $-130$ mV and 5% lower with a hyperpolarizing pulse from

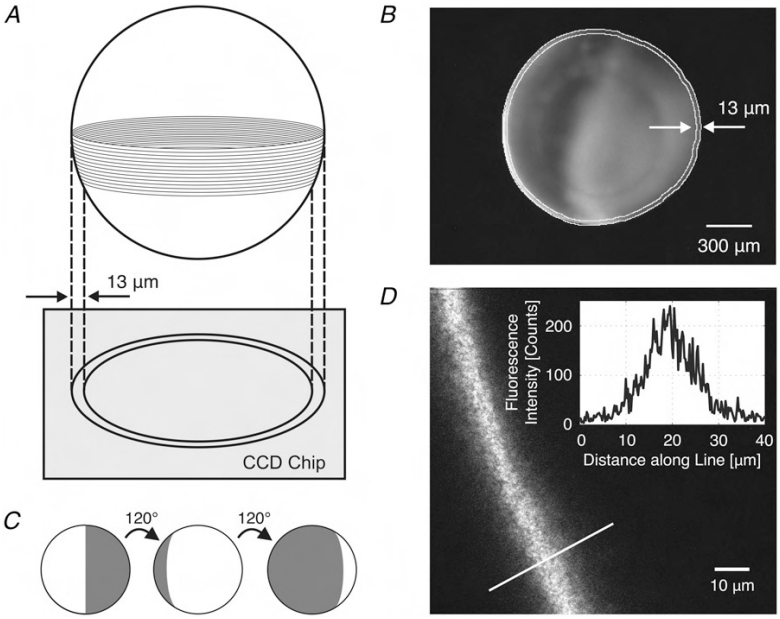


FIGURE 6 Data analysis of images of channel expressing oocytes. (*A*) Illustration of the projection of a small band along the circumference of an oocyte onto the CCD chip. (*B*) Image of an oocyte expressing $K^+$ channels. Only fluorescence light originating from the area in-between the two concentric rings is taken into account for data analysis. (*C*) Between successive images, the oocyte is rotated by 120°. (*D*) Confocal image of the membrane of an oocyte. The membrane shows fluorescence over a width of $\simeq$13 $\mu$m (full width at half-maximum).

−130 to −160 mV. As expected, the gating charge was the same when a hyperpolarizing pulse from −150 to −180 mV was applied, because, in this region, charge movement is purely linear. This pulse protocol with a hyperpolarizing pulse from −150 to −180 mV was used for all subsequent measurements of $K^+$ channel gating currents.

For the $Na^+$ channels, a hyperpolarizing pulse from −120 to −150 mV was sufficient, because $Na^+$ channels do not show voltage-dependent steps at these hyperpolarizing potentials. Holding the membrane at −120 mV for 20 min was adequate to bring all voltage sensors down to the resting state position and to recover all channels from the slow inactivation known for $Na^+$ channels (see, for example, (24)).

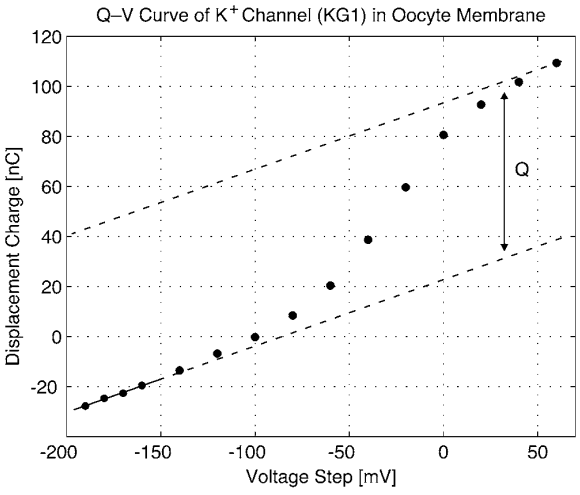


FIGURE 7 Displacement charge (capacitive and gating charge) as a function of applied voltage steps of a $K^+$ channel. The holding potential was at −100 mV. A fit illustrates the linearity in the region from −200 to −150 mV (*lower dashed line*). The extrapolation of the fit in the region from −150 to + 60 mV shows the deviation from linearity (i.e., movement of gating charges). The distance between the two dashed lines corresponds to the total gating charge $Q$.

## Correlation of gating charge and fluorescence intensity

The plots in Fig. 8 show the fluorescence intensity as a function of the gating charge. For all constructs, fluorescence intensity and gating charge are positively correlated. When normalized to the slope of KG1, the slope of KG2 is approximately twice as high and the slope of KG3 is three times as high as the slope of KG1 ($S_{KG2}/S_{KG1} \simeq 2.3; S_{KG3}/S_{KG1} \simeq 3.0$), as can be expected. The slope of NaG4 is only $\simeq$1.1 times higher than that of NaG3.

Further analysis of these data was based on the following assumptions. The fluorescence intensity $F$ is proportional to the total number of channels $N$ times the number of eGFP molecules per channel of the construct # $eGFP_{K,\,Na}$, and the total gating charge $Q$ is equal to the total number of channels $N$ times the single gating charge $q_{K,\,Na}$,

$$F = c \times N \times \#\,\mathrm{eGFP}_{K,Na}$$
$$Q = N \times q_{K,Na}, \quad (1)$$

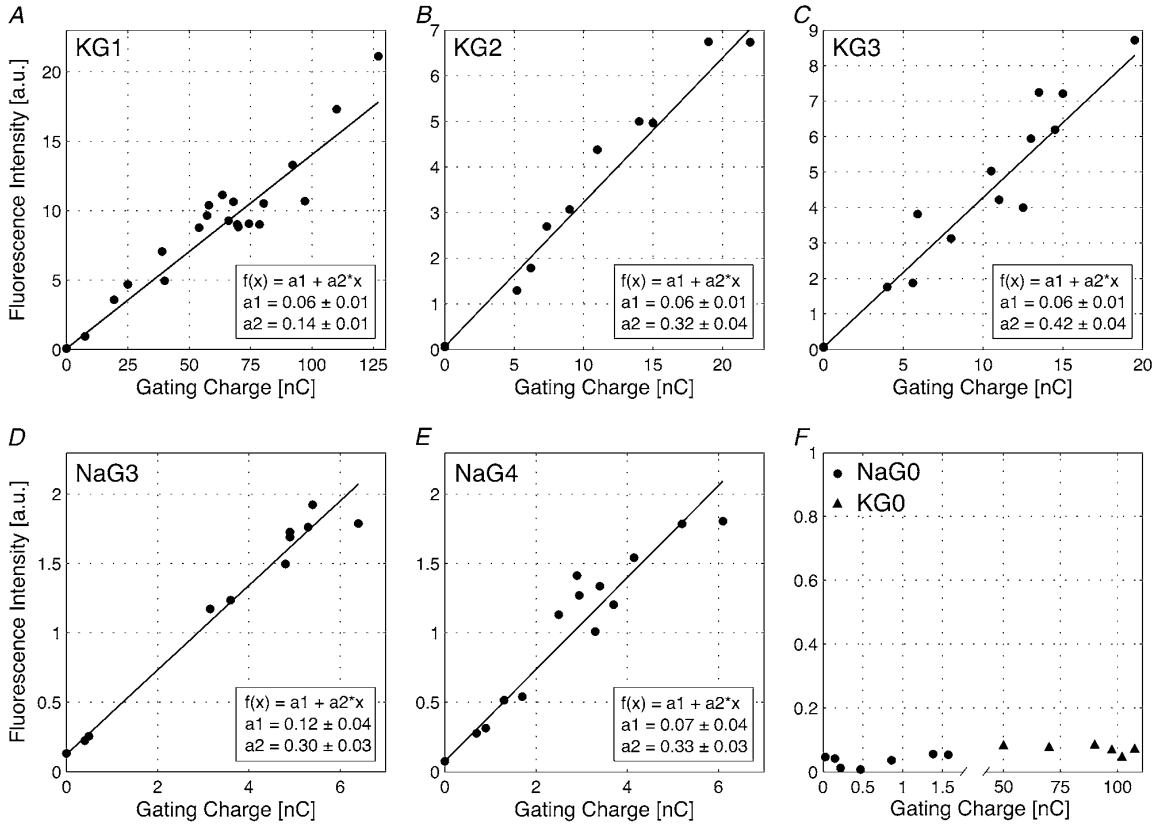


FIGURE 8 Fluorescence intensity as a function of gating charge for all channel constructs. In each of the graphs (*A–E*), the straight line represents the best fit to the data. The first data point in each graph corresponds to a noninjected control cell. These data points are included in the fit, but the fit is not forced to coincide with these points. (*A–C*) Fluorescence intensity as a function of gating charge for $K^+$ channel constructs with four (KG1), eight (KG2), and twelve (KG3) eGFP molecules per channel. (*D–E*) Fluorescence intensity as a function of gating charge for $Na^+$ channel constructs with three (NaG3) and four (NaG4) eGFP molecules per channel. The linear fits of all $K^+$ and $Na^+$ channel constructs only show a small deviation from linearity. (*F*) Fluorescence intensity as a function of gating charge for $K^+$ (*triangles*) and $Na^+$ (*circles*) channel constructs without eGFP molecules. Autofluorescence remains constant over time and expression level (at $\simeq$0.07 for KG0 and at $\simeq$0.04 for NaG0, which is in good agreement with the autofluorescence of the noninjected control cells). All data are normalized to the same illumination and detection properties to allow for a direct quantitative comparison.

where the proportionality factor $c$ depends only on the illumination and detection properties of the setup (and not on the specific channel construct). For this reason, the change of the slope from one construct to another reflects the change in fluorescence intensity due to the presence of different numbers of eGFP molecules per channel in each construct. All linear fits to the data intersect the $y$ axis at the same point which coincides with the autofluorescence found for control cells without eGFP (KG0 and NaG0). Therefore, after rearrangement of Eq. 1, the ratio of the single gating charges can be expressed as

$$\frac{q_K}{q_{Na}} = \frac{\#\,\mathrm{eGFP_K}}{S_K} \div \frac{\#\,\mathrm{eGFP_{Na}}}{S_{Na}}, \qquad (2)$$

where $S_K = F_K/Q_K$ and $S_{Na} = F_{Na}/Q_{Na}$ are the slopes of the correlations.

The ratios between the number of eGFP molecules and the correlation slopes are summarized for all channel constructs in Table 1.

With these numbers and Eq. 2, the ratio of the single gating charges between $K^+$ and $Na^+$ channels was obtained as

$$\frac{q_K}{q_{Na}} = 2.5 \pm 0.4.$$

**TABLE 1 Ratio of the number of eGFP molecules to the slope of the correlations**

| Channel | No. eGFP / F/Q | Weighted mean* |
|---|---|---|
| KG1 | 28.6 ± 2.0 | 27.8 ± 1.4 |
| KG2 | 25.0 ± 3.1 | |
| KG3 | 28.6 ± 2.7 | |
| NaG3 | 10.0 ± 1.0 | 11.0 ± 0.7 |
| NaG4 | 12.1 ± 1.1 | |

*Weighted means are from KG1 to KG3 and from NaG3, NaG4, respectively.

## DISCUSSION

The initial motive behind this study was to examine $Na^+$ channels marked with eGFP fluorophores and expressed in *Xenopus* oocytes. However, when marked with just one eGFP in the C-terminal, their fluorescence is very weak. To improve on this, multiple tandem repeats of eGFP were constructed and tested in $K^+$ channels. These channels have several advantages: 1), ~5–10 times higher expression in oocytes; and 2), Due to their four independent domains—each having a C-terminal—automatically four times more fluorescence was obtained per channel. As shown in this article, it became clear that the channels operate normally even with higher multiples of the fluorophore. The method of obtaining a reliable estimate for the total fluorescence by rotating the oocytes and averaging the integrated fluorescence from tangential sections was developed. And, as shown in this study, the so-obtained fluorescence was strictly proportional to the gating charge and to the number of incorporated eGFP molecules. Furthermore, the contamination by autofluorescence of the cytoplasm was shown to be negligible in this tangential section.

These studies also paved the way for applying the method to the more-difficult $Na^+$ channels. In the course of the study, it became obvious that the results obtained could be used for a new approach to estimate the single gating charge of the $Na^+$ channels. As outlined in the Introduction, in the present literature there are many more estimates of the single gating charge for the *Shaker* $K^+$ channel with figures at ~12–14 elementary charges, but only little is published for the $Na^+$ channel. As shown in this study, the new data provide a ratio between the two single gating charges and, therefore, an estimate from the better-known $K^+$ channels to the less-known $Na^+$ channels. Before discussing this in more detail, some critical points about the method used shall be discussed here.

### Submembranous channels

Most critical is a possible contamination of the fluorescence by submembranous channels which would not produce gating current but fluorescence. These could be channels which are expressed and traveling toward the membrane and are not yet incorporated, or channels which have left the membrane by endocytosis with the eGFP molecules still functioning. Fig. 8 illustrates clearly, that a substantial and changing amount of submembranous channels can be excluded. The data points are close to the linear fit, i.e., in a constant proportion to the number of the membrane-bound channels which produce gating charge. If over the time of the 3–14 days of channel expression the amount of channels resting under the membrane would change substantially, a nonconstant relation to the incorporated channels should be present. However, the two special cases where such contaminating channels would be present in either a constant amount or in a constant percentage relative to the membrane-bound channels shall be discussed in the following.

In the ideal uncontaminated case, the correlation can be described by the equation $F_n(Q_n) = s_nQ_n + b_n$, where $F_n$ is the fluorescence signal, $s_n$ the slope of the correlation, $Q_n$ the gating charge, and $b_n$ the contribution of autofluorescence. The index $n$ denotes the number of incorporated eGFP molecules of the construct under investigation. It seems reasonable to assume that neither the gating charge nor the level of autofluorescence depends on the number of inserted eGFP molecules, which means $Q_n = Q$ and $b_n = b$. The correlation can then be rewritten as

$$F_n(Q) = s_nQ + b. \tag{3}$$

The constant $b$ is the intercept of the correlations with the $y$ axis (see Fig. 8).

### Constant amount of submembranous channels

Assuming a constant amount of submembranous channels, there would be a contribution $c_n$ to the fluorescence signal, which would be constant over time. Equation 3 would then change to $F_n(Q) = s_nQ + b + c_n$. The $c_n$ values are dependent on and proportional to the number of eGFP molecules of the construct, i.e., $c_n = k_1n$, where $k_1$ is the same constant factor for all channel constructs. If this were the case, all correlations would be shifted by $c_n$, which would grow with $n$. As can be seen in Fig. 8, *A–E*, all correlations intercept the $y$ axis—within the error—at the same position (at 0.06 for $K^+$ channels and at ≃0.10 for $Na^+$ channels; see Fig. 8). Measurements on channel constructs without eGFP show fluorescence intensity values which coincide with the intercept of the correlations (see Fig. 8 *F*). Therefore, this type of submembranous channel is either not present, or, if present, its contribution to the fluorescence signal is so low that its effect is not detectable by the presented method.

### Constant percentage of submembranous channels

If the channels under the membrane, within the 13-$\mu$m ring of the evaluated tangential section, would be of a relevant constant percentage relative to the membrane-bound channels, the slope of the correlation would increase. An additional factor $d_n$, which would change the slope of the correlation, would have to be introduced. Equation 3 would be modified as

$$F_n(Q) = (s_n + d_n)Q + b. \tag{4}$$

Again, the $s_n$ and $d_n$ values are proportional to the number of eGFP molecules per channel of the construct under investigation. Therefore, $s_n = k_2n$ and $d_n = k_3n$, where $k_2$ and $k_3$ are the same constant factors for all channel constructs. With Eq. 4 follows

$$s_n = k_2n \quad \Rightarrow \quad \frac{s_n}{s_m} = \frac{k_2n}{k_2m} = \frac{n}{m}$$

$$d_n = k_3n \quad \Rightarrow \quad \frac{s_n + d_n}{s_m + d_m} = \frac{k_2n + k_3n}{k_2m + k_3m} = \frac{n}{m},$$

where $s_m$ is the F/Q slope of a channel construct with $m$ eGFP molecules per channel. The ratio of the slopes of two different channel constructs is therefore independent of the presence of this type of submembranous channel, and Eq. 2 can be applied without modification.

Since such a contamination would still result in a linear relation between $F$ and $Q$, it cannot be safely excluded by our data. However, since the different constructs KG1 to KG3 show slopes which increase according to the number of eGFPs in each construct, it is very likely that such contamination would be of constant percentage across all constructs. Most likely, this argument is valid also for the $Na^+$ channels and then it would not change the obtained ratio of $q_K/q_{Na}$. If this argument does not apply to the $Na^+$ channels, the ratio of submembranous to membrane-bound channels would be greater for $Na^+$ channels than for $K^+$ channels, because the $Na^+$ channel is four times larger and does not express as well in the membrane as the $K^+$ channel. Then the fluorescence intensity of the $Na^+$ channels were overestimated and the real $q_{Na}$ would be larger (see Eq. 1 and 2). Thus, the obtained ratio $q_K/q_{Na}$ represents an upper limit.

## Quenching

Fluorophore-fluorophore quenching can result either from the interaction of eGFP molecules of neighboring channels or from eGFP molecules within the same channel.

The number of expressed channels is $\sim 10^{10}$ per oocyte. The diameter of a typical oocyte is $\simeq$1.2 mm and thus has a spherical surface area of $\simeq$4.5 $mm^2$. Because the surface of the oocyte is not flat but enlarged by microvilli, its effective surface is approximately four times larger. This leads to a channel density of $\simeq$550 channels/$\mu m^2$ and thus to a mean distance of $\simeq$40 nm between neighboring channels. Quenching can only occur when the fluorophore and the quencher (which, in this case, is another eGFP molecule) are in close vicinity. Typical distances for quenching to occur are $\sim$0.2 nm (25). Therefore, fluorophore-fluorophore quenching between eGFP molecules of neighboring channels is very unlikely to occur. Furthermore, fluorescence intensity and gating charge would not be linearly dependent from each other, because fluorescence intensity would be reduced as more channels are expressed. This stands in contradiction to our findings.

Fig. 9 shows a plot of the slopes that were found in the correlation measurements on $K^+$ channels as a function of the number of eGFP molecules per channel. The three data points correspond to $K^+$ channels with 4, 8, and 12 eGFP molecules per channel and are close to the linear fit. If fluorophore-fluorophore quenching between eGFP molecules from within an individual channel were present, a reduced fluorescence intensity would be expected as more eGFP molecules per channel are introduced, i.e., the slopes of the correlations as a function of the number of eGFP molecules per channel would decrease for higher multiples of eGFP, which is not the case. This is in accordance with a study from Chen et al. (26), who measured the fluorescence intensity of oligomerized eGFP molecules and found quenching not to be present for tandem eGFP molecules. For further confirmation, see Saffarian et al. (27).

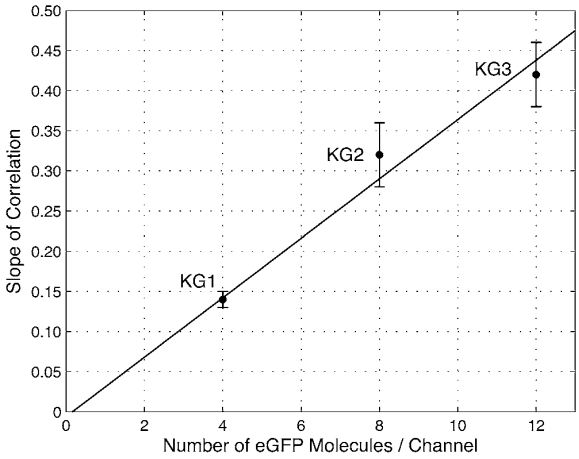


FIGURE 9 Slopes of the correlations of fluorescence intensity versus gating charge (see Fig. 8) of the three $K^+$ channel constructs (KG1, KG2, and KG3) as a function of the number of eGFP molecules per channel. The straight line represents the best fit to the data (see Discussion).

## Concluding remarks

Taking the ratio of $q_K/q_{Na}$ of 2.5 $\pm$ 0.4 and a figure for $q_K$ of $\sim$13 elementary charges which is supported by the many studies quoted in the Introduction, it follows that the single gating charge for activation of the rBIIA $Na^+$ channel would be $\sim$5.2 elementary charges. It has also to be mentioned that the integration for the $Na^+$ gating charge covers the main gating current, which ends shortly after the activation peak. Therefore, it does not include all of the gating charge related to inactivation. Greeff and Forster (28) were able to detect the slow component of the gating current during the inactivation phase of the macroscopic sodium current. They estimated a number of 1.21 elementary charges to be correlated with inactivation. These open-inactivated transitions might have occurred in $\sim$50% of all channels during the integration time for the total gating charge $Q$ used in this study. Thus, $\sim$0.6 elementary charges should be added, resulting in 5.8 elementary charges for $q_{Na}$, including inactivation.

This number is supported by the work of Conti and Stühmer (7), who estimated a value of six-to-eight elementary charges for the rBIIA $Na^+$ channel. Furthermore, Sheets and Hanck (8) estimated a lower limit of the single gating charge of the human cardiac hH1a $Na^+$ channel to be 5.2 elementary charges. In this context, it is also worthwhile to quote the study by Noceti et al. (3). They found 13 elementary charges for the single gating charge of the *Shaker* $K^+$ channel and 8.6 for the $Ca^{2+}$ channel, which has a very similar molecular structure as the $Na^+$ channel. They determined the single gating charges of the *Shaker* $K^+$ channel and the $Ca^{2+}$ channel by using the same method.

At present, it is well accepted that, from the four domains in the $Na^+$ channel, DI and DII are responsible for activation but the function of DIII is under dispute (29) and DIV is related to inactivation (14,30). With respect to the study by Hirschberg et al. (9) that gives a figure of at least 12 elementary charges for $q_{Na}$, it has to be mentioned that it concerned muscle $Na^+$ channels in contrast to the rat brain IIA sodium channels of this study. As a further point, it may be considered that $Na^+$ channels in nerve might be optimized for speed. Such an optimization has been proposed by Hodgkin in 1975 for the propagation speed of the action potential in squid (31); for optimal speed the gating charge should be rather smaller and the single ionic current rather larger. In this context, a recent study by Angelino and Brenner (32) analyzes the presently known $Na^+$ channels with respect to the propagation of the action potential and shows clear differences between the nerve and muscle $Na^+$ channels. Therefore, a figure at approximately six elementary charges for the $Na^+$ channel activation in nerve seems reasonable.

## REFERENCES


1. Hodgkin, A. L., and A. F. Huxley. 1952. A quantitative description of membrane current and its application to conduction and excitation in nerve. *J. Physiol.* 117:500–544.
2. Aggarwal, S. K., and R. MacKinnon. 1996. Contribution of the S4 segment to gating charge in the *Shaker* $K^+$ channel. *Neuron.* 16:1169–1177.
3. Noceti, F., P. Baldelli, X. Wei, N. Qin, L. Toro, L. Birnbaumer, and E. Stefani. 1996. Effective gating charges per channel in voltage-dependent $K^+$ and $Ca^{2+}$ channels. *J. Gen. Physiol.* 108:143–155.
4. Zagotta, W. N., T. Hoshi, J. Dittman, and R. W. Aldrich. 1994. *Shaker* potassium channel gating. II. Transitions in the activation pathway. *J. Gen. Physiol.* 103:279–319.
5. Schoppa, N. E., K. McCormack, M. A. Tanouye, and F. J. Sigworth. 1992. The size of gating charge in wild-type and mutant *Shaker* potassium channels. *Science.* 255:1712–1715.
6. Islas, L. D., and F. J. Sigworth. 1999. Voltage sensitivity and gating charge in *Shaker* and *Shab* family potassium channels. *J. Gen. Physiol.* 114:723–741.
7. Conti, F., and W. Stühmer. 1989. Quantal charge redistributions accompanying the structural transitions of sodium channels. *Eur. Biophys. J.* 17:53–59.
8. Sheets, M. F., and D. A. Hanck. 2005. Charge immobilization of the voltage sensor in domain IV is independent of sodium current inactivation. *J. Physiol.* 563:83–93.
9. Hirschberg, B., A. Rovner, M. Lieberman, and J. Patlak. 1995. Transfer of twelve charges is needed to open skeletal muscle $Na^+$ channels. *J. Gen. Physiol.* 106:1053–1068.
10. Kuzmenkin, A., F. Bezanilla, and A. M. Correa. 2004. Gating of the bacterial sodium channel, NaChBac: voltage-dependent charge movement and gating currents. *J. Gen. Physiol.* 124:349–356.
11. Gamal El-Din, T. M., D. Grögler, H. Heldstab, C. Lehmann, and N. G. Greeff. 2007. Estimation of the number of voltage-gated ion channels by fluorescence-gating charge correlation. *Biophys. J.* 2246-Pos. 470a. (Abstr.).
12. Gamal El-Din, T. M., D. Grögler, H. Heldstab, C. Lehmann, and N. G. Greeff. 2008. eGFP fluorescence as a tool to compare the gating charge per voltage-dependent ion-channel in *Xenopus laevis* oocytes. *Biophys. J.* 94:1363. (Abstr.).
13. Grögler, D., T. M. Gamal El-Din, C. Lehmann, H. Heldstab, and N. G. Greeff. 2008. Relative comparison of the effective gating charge between voltage-gated K- and Na-channels. *Biophys. J.* 94:1862. (Abstr.).
14. Kühn, F. J. P., and N. G. Greeff. 1999. Movement of voltage sensor S4 in domain 4 is tightly coupled to sodium channel fast inactivation and gating charge immobilization. *J. Gen. Physiol.* 114:167–183.
15. Siegel, M. S., and E. Y. Isacoff. 1997. A genetically encoded optical probe of membrane voltage. *Neuron.* 19:735–741.
16. Campbell, R. E., O. Tour, A. E. Palmer, P. A. Steinbach, G. S. Baird, D. A. Zacharias, and R. Y. Tsien. 2002. A monomeric red fluorescent protein. *Proc. Natl. Acad. Sci. USA.* 99:7877–7882.
17. Schreibmayer, W., H. A. Lester, and N. Dascal. 1994. Voltage clamping of *Xenopus laevis* oocytes utilizing agarose-cushion electrodes. *Pflugers Arch.* 426:453–458.
18. Harms, G. S., L. Cognet, P. H. M. Lommerse, G. A. Blab, and T. Schmidt. 2001. Autofluorescent proteins in single-molecule research: applications to live cell imaging microscopy. *Biophys. J.* 80:2396–2408.
19. Sonnleitner, A., L. M. Mannuzzu, S. Terakawa, and E. Y. Isacoff. 2002. Structural rearrangements in single ion channels detected optically in living cells. *Proc. Natl. Acad. Sci. USA.* 99:12759–12764.
20. Bluemink, J. G., W. J. Hage, M. H. F. Van der Hoef, and W. J. A. G. Dictus. 1983. Freeze-fracture changes in progesterone-induced maturing oocytes and eggs of *Xenopus* oocytes. *Eur. J. Cell Biol.* 31:85–93.
21. Yamaguchi, S., J. L. Hedrick, and C. Katagiri. 1989. The synthesis and localization of envelope glycoproteins in oocytes of *Xenopus laevis* using immunocytochemical methods. *Dev. Growth Differ.* 31:85–94.
22. Dumont, J. N. 1972. Oogenesis in *Xenopus laevis* (Daudin): I. Stages of oocyte development in laboratory maintained animals. *J. Morphol.* 136:153–179.
23. Soreq, H., and S. Seidman. 1992. *Xenopus* oocyte microinjection: from gene to protein. *In* Methods in Enzymology, Vol. 207—Ion Channels. B. Rudy, and L. E. Iverson, editors. Academic Press, New York.
24. Bulatko, A. K., and N. G. Greeff. 1995. Functional availability of sodium channels modulated by cytosolic free $Ca^{2+}$ in cultured mammalian neurons (N1E−115). *J. Physiol.* 484:307–312.
25. Lakowicz, J. R. 2006. Principles of Fluorescence Spectroscopy, 3rd Ed. Springer, New York.
26. Chen, Y., L.-N. Wei, and J. D. Müller. 2003. Probing protein oligomerization in living cells with fluorescence fluctuation spectroscopy. *Proc. Natl. Acad. Sci. USA.* 100:15492–15497.
27. Saffarian, S., Y. Li, E. L. Elson, and L. J. Pikey. 2007. Oligomerization of the EGF receptor investigated by live cell fluorescence intensity distribution analysis. *Biophys. J.* 93:1021–1031.
28. Greeff, N. G., and I. C. Forster. 1991. The quantal gating charge of sodium channel inactivation. *Eur. Biophys. J.* 20:165–176.
29. Cha, A., P. C. Ruben, A. L. George, E. Fujimoto, and F. Bezanilla. 1999. Voltage sensors in domains III and IV, but not I and II, are immobilized by $Na^+$ channel fast inactivation. *Neuron.* 22:73–87.
30. Chanda, B., and F. Bezanilla. 2002. Tracking voltage-dependent conformational changes in skeletal muscle sodium channel during activation. *J. Gen. Physiol.* 120:629–645.
31. Hodgkin, A. L. 1975. The optimum density of sodium channels in an unmyelinated nerve. *Philos. Trans. R. Soc. Lond. B Biol. Sci.* 270:297–300.
32. Angelino, E., and M. P. Brenner. 2007. Excitability constraints on voltage-gated sodium channels. *PLoS Comput. Biol.* 3:1751–1760.

## 2.5 Conclusions

The gating charge of a single *Shaker* $K^+$ channel has been determined to be $2.5 \pm 0.4$ times larger than the gating charge of a rBIIA $Na^+$ channel. Based on the repeatedly and consistently reported size of the gating charge of the *Shaker* $K^+$ channel ($13 e_0$), this finding allows to estimate the gating charge of the lesser known rBIIA $Na^+$ channel to be equivalent to $5.2 \pm 0.3$ elementary charges.

The gating process by which voltage gated ion channels control their ionic conductivity in response to changes in the transmembrane voltage is still not fully understood. Most of the gating charge is located on the fourth segment S4 of each subunit of $K^+$ channels and of each domain of $Na^+$ channels. S4 constitutes the central part of the voltage sensor. In addition to functional studies employing site–directed mutations and to the interpretation of X–ray diffraction patterns of crystallized channel proteins, information about the size of the gating charge allows for a more precise understanding of the structure and functioning of voltage gated ion channels.

A new method for the quantification of the number of gating charges in voltage gated ion channels has been developed. The intensity of the fluorescence emission of genetically encoded enhanced green fluorescent proteins (eGFP) has been used in order to quantify the number of channels in the oocytes. The two main difficulties with respect to the determination of eGFP fluorescence intensity of membrane bound ion channels in *Xenopus laevis* oocytes are the large and inhomogeneously distributed autofluorescence of the cell and the uneven distribution of channel proteins on the cell surface.

The cytoplasmatic solution inside the cells is the primary source of autofluoresence. The contribution of autofluorescence to the optical signal was to a large extent excluded from data analysis by taking into account only the fluorescence signal originating from a narrow region along the circumference of the oocyte. The depth of this region was chosen to be $\simeq 13 \mu$m, ensuring a maximum ratio between eGFP fluorescence intensity and the intensity of autofluorescence. To account for inhomogenities of both the distribution of channels and of the sources of autofluorescence, the mean value of three different orientations of the cells was determined. It was found that this method allows for a relative estimation of the number of ion channels with an uncertainty of $\simeq 10\,\%$. The gating characteristics of both the modified *Shaker* $K^+$ channel and the rBIIA $Na^+$ channel were found to be identical to

the constructs without any attached eGFP molecules. This indicates that the functioning of the modified channels is unaltered and that the performed measurements reflect the gating properties of the original channel proteins.

The relevance of the presented method could be further strengthened if the gating charges of voltage gated ion channels could be determined absolutely. For that purpose, the absolute number of channels would have to be determined. In principle, the same method as presented here could be used to quantify the fluorescence intensity of eGFP in absolute terms. The calibration of the fluorescence emission would allow to infer on the number of channels. This procedure has proven to be quite straightforward when applied to a thin layer of fluorophores on a flat surface [94, 95]. However, on the curved and uneven surface on an oocyte with a large and noisy background from the cell, calibration could turn out to be more of a challenge.

Time–resolved measurements could be yet another application of the presented method. It is known that modified channel constructs, as used in this study, change the intensity of their fluorescence emission during activation of the channel [96, 97]. The underlying physical process is still not known; eGFP fluorescence is possibly quenched when the attached eGFP molecule is dragged into direct vicinity of the cellular membrane during the conformational change of the channel protein. The simultaneous recording of the gating current and of changes in fluorescence emission can give valuable information about the kinetics and the structure of the protein.

Without any doubt, the most direct insight into the gating process could be gained if the eGFP fluorescence emission of a single channel could be detected. Even though the electrophysiological measurements would still require a large number of ion channels to reach current signals above the noise level, the optical detection of fluorescence photons could be confined to just a few or even one single channel. Chapter three presents a method to excite only a few fluorophores at a time by making use of optical fibers to excite fluorophores.

# 3 Fluorescence excitation by use of optical fibers

The overwhelming majority of studies in the field of voltage gated ion channels deals with large populations of channel proteins. And indeed, measurements on large populations of ion channel proteins can provide valuable information on the properties of ion channels. However, since the signal of these measurements is a superposition of the signals of many single channels, the exact processes taking place on the molecular level often remain unknown.

Even though the four domains of the $Na^+$ channel are quite similar and its tertiary structure is symmetrical, channel function is not evenly distributed among the four domains. For example, part of the cytoplasmatic linker between the domains III and IV of $Na^+$ channels is known to play a crucial role in the process of inactivation of the $Na^+$ channel [98]. It seems manifest that other functions of the channel could also be connected to specific sites of the protein rather than being the superposition of four identical processes. In contrast to the $Na^+$ channel, the $K^+$ channel is a tetramer of four identical subunits whose tertiary structure is highly symmetrical. Therefore, it seems reasonable to assume that all four subunits play identical roles in the protein. Still, it would be worthwhile to study exactly how these subunits interact. Do the four subunits move simultaneously while the channel activates? Can activation be triggered by the movement of just one of the four S4 segments? Questions such as these could be answered if it were possible to mark individual sites in a single channel protein and observe its reaction upon electrical or optical stimuli.

Indisputably, it would be of great benefit if channel kinetics could be studied on single channels. For the time being, electrophysiological recordings need to be carried out on many channels for the electrical signal to be large enough to be detectable. On the other hand, fluorescence can principally be detected on the single molecule level. In this chapter, a system will be presented that uses optical fibers both to excite fluorophores and to detect their fluorescence emission light.

At an excitation intensity of $13\,\mathrm{kW/cm^2}$ an eGFP molecule emits $\simeq 1500\,\mathrm{photons/ms}$ [99]. In conventional fluorescence microscopes, typical excitation energies are smaller by several orders of magnitude. Single–mode optical fibers have a relatively small numerical aperture (NA) of $\simeq 0.2$–$0.3$. However, with these numbers and a quantum efficiency of the detector system of $\simeq 25\,\%$, count rates of $4-8\,\mathrm{kHz}$ could be achieved.

As was demonstrated in the second chapter, another limitation of fluorescence measurements on biological cells is their intrinsic autofluorescence, which is mainly caused by flavins in the cytoplasm [99–101]. In conventional fluorescence microscopy, the whole sample – not only the part that is imaged, nor only the focal plane – is exposed to strong excitation light. One consequence is image degradation due to the contribution of out–of–focus light to the image. Furthermore, autofluorescence causes a high background signal in fluorescence intensity measurements and can also lead to phototoxic reactions in the sample. It is therefore crucial to suppress the autofluorescence signal either by not exciting autofluorescent proteins in the first place, or by limiting the detection volume. A variety of techniques are potentially suitable for this task. A short overview of the most important techniques will be given in the following sections.

## Confocal microscopy

The main parts of a confocal microscope are a point light source, a dichroic mirror, a microscope objective and a detection system such as a photomultiplier in front of which a pinhole is placed. The excitation light originates from the point source, passes the dichroic mirror undeflected and is focused onto the sample by the microscope objective. The generated fluorescence light is then collected by the same objective and – as the fluorescence emission light is redshifted with respect to the excitation light – reflected by the dichroic mirror onto the detector. The pinhole is placed in a conjugate plane right before the detector, therefore out–of–focus light is blocked. Because only one point of the sample is excited at a time and only the fluorescence emission originating from this point is detected, the system has to scan over the sample point–by–point. Depending on the fluorescence properties of the sample and on the desired spatial resolution, the time resolution can be very low (ms – min). The depth of field is typically in the order of $\simeq 0.6\mu\mathrm{m}$. The acquisition of multiple images from different focal planes allows to generate 3–D images. Marvin Minsky developed one of the first confocal microscopes and patented it in 1961 [102].

## Two photon microscopy

Most fluorophores can be excited by the quasi–simultaneous absorption of two photons of approximately double the wavelength of their excitation maximum. For excitation to occur, the two photons have to arrive within a time frame of about $10^{-15}$–$10^{-18}$s, which is the time the virtual absorption of a non–resonant photon lasts. To raise the probability of this process to practical levels, very high laser intensities have to be used (0.1–10 MW/cm$^2$), which can be achieved by pulsed femtosecond or picosecond lasers. In the microscope, two laser beams are focused onto the sample. Because the probability of two photons arriving at the same time is a function of the square of laser intensity, the system can be fine–tuned in such way that in the focal spot only the photon density is high enough for two–photon absorption to occur. Therefore, nearly no fluorescence emission is generated outside the focal volume.

For typical fluorophores with an excitation maximum around 400–500 nm, the laser has to emit in the infrared at around 900 nm. This has a profound impact on image quality and resolution in comparison to one–photon excitation: the scattering cross section is reduced 16–fold, because the predominant process within cellular structures is Rayleigh scattering, for which the cross section in proportional to the inverse of the fourth power of the wavelength. Not only does this improve image quality, it also allows to excite fluorophores as deep as 1 mm within the sample (which is about 10× deeper than what may be achieved with confocal microscopy). Furthermore, crosstalk is much less of an issue, since excitation and emission light are separated by a few hundred nm as compared to a few tenths of nm – depending on the Stokes shift of the fluorophore – in conventional fluorescence microscopy. Radial and axial resolution is in the order of $\simeq 0.4\,\mu$m and $\simeq 0.8\,\mu$m, respectively. The theoretical possibility of two photon absorption was predicted in 1931 by Maria Göppert–Mayer [103] and experimentally proven in 1961 by Kaiser and Garrett [104] when the first continuous wave lasers were available. Denk and colleagues developed and patented the method in its modern form in the early 1990's [105, 106].

## Total internal reflection microscopy (TIRF)

This technique makes use of the fact that light traveling from an optically dense into an optically less dense medium undergoes total internal reflection at the border of the two media, if the angle of incidence is lower than a critical angle which is dependent on the

refractive indices of the two media. At the border of the two media an evanescent electromagnetic field is built up, which extends into the second medium (the sample). The maximum penetration depth of the field is also dependent on the refractive indices of the two media, and exponentially decays when looked at as a function of the penetration depth. If a fluorophore is in the vicinity of the border of the two media, it then is excited by this evanescent field, leading to fluorescence emission. This is termed *frustrated* total internal reflection and TIRF is sometimes called *frustrated* total internal reflection microscopy or FTIR. The exponential decay of the evanescent field only allows to excite fluorophores which are positioned in close vicinity to the boundary between the sample and the sample holder. This greatly improves the signal to noise ratio because fluorescence from out–of–focus fluorophores is not detected. Consequently, this improves the spatial resolution. The fluorescence light can be detected by CCD cameras and hence a high time resolution can be achieved (depending on the fluorophore 1 – 100 ms). However, only a region whose thickness is in the order of a few hundred nanometer can be imaged. By fine–tuning the angle of incidence, distance measurements and tracking of fluorophores can be performed with a resolution up to a few nm [107, 108]. Excitation light can be directed onto the sample, either through the microscope objective, or by coupling the excitation light through a prism into a glass slide which holds the sample. The theoretical background underlying the processes of total internal reflection was outlined by Elmer Hall in 1902 [109] and the experimental implementation was mainly realized by Daniel Axelrod at the end of the 1980's [110].

### Scanning near–field microscopy

The resolution of conventional far–field microscopy techniques is ultimately limited by the wavelength of the illuminating light. Scanning near–field microscopy (SNOM) allows to increase the resolution beyond this limit up to two orders of magnitude. The excitation light is coupled into a metal coated optical fiber with sub–wavelength diameter. At the tip of the probe an evanescent field is generated. When the probe is placed close enough to the sample (typically a few nm), the evanescent field can excite the sample. Fluorescence emission light can then, for example, be collected by a conventional microscope objective. As in TIRF, SNOM allows to image surfaces only. Additionally, a feedback system is necessary to guarantee that the tip remains at the correct distance from the specimen during

scanning. The working distance is very small which limits the technique to very flat samples. Due to the high spring constants of optical fibers, imaging of soft materials is hard to achieve which makes scanning near field microscopy not suitable for many biological specimen. To use an aperture with sub–wavelength dimension to image objects was proposed already 80 years ago by Synge [111]. In 1984, SNOM was demonstrated for the first time independently by the groups of Pohl [112] and Lewis [113].

### Excitation and detection of fluorescence by use of optical fibers

This method uses optical fibers to guide the excitation light to the fluorophore and to collect the fluorescence emission. Through the use of thin glass fibers ($\varnothing \simeq 10-30\,\mu$m), the excitation volume can be kept sufficiently small. Furthermore, this setup is very flexible and easy to install. The details of this approach and experimental results will be outlined in the following sections.

## 3.1 Fiber optics

Single–mode step–index fibers – as were used in this study – are cylindrical waveguides that allow to transmit light over large distances with very low attenuation (distances of km with losses of a few percent only). Once light has been coupled into the fiber, it can easily be directed to the sample for fluorescence excitation or to other parts of a setup without the need of additional optical components. Step–index fibers have an inner part (called the *core*), that has a high refractive index, surrounded by an outer part (called the *cladding*) of lower refractive index (see figure 3.1). In many cases fused silica, or quartz ($SiO_2$), is the material of choice, because it has a high transmission over a wide range of the visible spectrum and even into the infrared and UV, a range where many other glasses are not transparent. $SiO_2$ has a refractive index of 1.46 and is chemically and mechanically very stable. In order to change the refractive index, $SiO_2$ can be doped with germanium dioxide ($GeO_2$), which is less stable than $SiO_2$ but has a a higher refractive index ($n = 1.7$). Additionally – and even more importantly in the context of this study –, quartz glass has a very low autofluorescence.

If light propagates inside the core of the fiber and approaches the core–cladding boundary under an angle that is larger than the critical angle $\theta_c$, it will undergo total internal reflection at the boundary and will therefore stay confined within the core of the fiber. If

$n_1$ and $n_2$ are the refractive indices of the core and the cladding, respectively, applying Snell's law at the boundaries air–core and core–cladding leads to:

$$\begin{aligned} \sin\theta_c &= \frac{n_2}{n_1} \\ \sin\alpha_c &= n_1 \sin(90-\theta_c) \end{aligned} \tag{3.1}$$

where $\alpha_c$ is the acceptance angle, which is the largest angle under which incoming light will still be confined within the fiber. $\theta_c$ is the angle under which the light approaches the core–cladding boundary. The refractive index of air is assumed to be equal to 1. Light that approaches the fiber under an angle that is larger than $\alpha_c$ will loose a fraction of its intensity each time it reaches the core–cladding boundary because of its refraction into the cladding. In figure 3.1, these phenomena are illustrated by the thick and thin solid lines, respectively. Both the acceptance angle and the numerical aperture (NA) of an optical fiber are functions of the refractive indices of the core and cladding material only. In analogy to other optical systems such as microscope objectives, the numerical aperture of an optical fiber is defined as the sine of the acceptance angle. Together with equation 3.1 the numerical aperture and the acceptance angle of the fiber can be determined:

$$\begin{aligned} \mathrm{NA} := \sin\alpha_c &= n_1 \sin(90-\theta_c) = n_1 \left[1-\cos^2(90-\theta_c)\right]^{1/2} \\ &= n_1 \left[1-\sin^2\theta_c\right]^{1/2} = n_1 \left[1-\frac{n_2^2}{n_1^2}\right]^{1/2} = \sqrt{n_1^2-n_2^2} \\ \Longrightarrow \qquad \alpha_c &= \sin^{-1}\sqrt{n_1^2-n_2^2} \end{aligned} \tag{3.2}$$

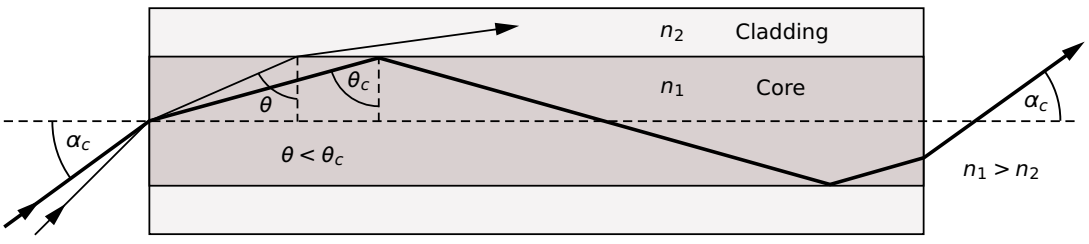


Figure 3.1: Schematic of a step–index optical fiber. $n_1$ and $n_2$ are the refractive indices of the core and the cladding, respectively. $\alpha_c$ is the acceptance angle, and $\theta_c$ is the critical angle for total reflection to occur at the core–cladding boundary.

It seems advantageous to maximize the numerical aperture by choosing core and cladding materials with large differences in refractive indices, in order to increase the acceptance angle and thereby to maximize the coupling and the detection efficiency. Unfortunately, with this approach, the single–mode property of the fiber is lost[1]. For this reason, refractive indices of core and cladding differ only slightly in practice. Typically, refractive indices are $\simeq 1.46$ and $\simeq 1.48$ for the core and the cladding, respectively, which leads to a numerical aperture of $\simeq 0.24$.

A critical part of a fiber optical setup is the point at which the light is coupled into the fiber. The coupling efficiency is dependent on the numerical aperture – or the acceptance angle – and on the optical properties of the surface of the fiber end. With a given power and beam profile of the light source, the coupling efficiency determines the maximum intensity with which fluorophores at the other end of the fiber can be excited. Obviously, impinging light should have an angle of incidence lower than the acceptance angle. Under experimental conditions, the fiber will never be as ideal as pictured in figure 3.1. More specifically, the fiber fronts will not be completely flat, which can dramatically change the coupling efficiency due to scattering and reflection of the incident light beam (see sections 3.2.4 and 3.3).

The angle upon which light enters the fiber tends to be preserved while the light propagates through the fiber core. Therefore, the maximum angle under which light leaves the fiber core is equal to the acceptance angle, if the maximum angle of the impinging light is larger or equal to the acceptance angle, and smaller if the maximum angle of the impinging light is smaller than the acceptance angle. For this reason and because $90° \geq \alpha \geq \beta$, it follows that:

$$\mathrm{NA} = \sin\alpha \geq \sin\beta \tag{3.3}$$

where $\beta$ is the angle under which the light leaves the fiber. This allows to calculate a lower limit of the numerical aperture if the maximum angle $\beta$ under which light leaves the fiber is known.

[1] The number of modes an optical fiber can guide is dependent on the numerical aperture and on the fiber dimensions. If single–mode fibers are needed, the numerical aperture is limited by $NA < 2.405\,\lambda/(\pi d)$, where $d$ is the diameter of the fiber and $\lambda$ the wavelength of the light source (see for example [114]).

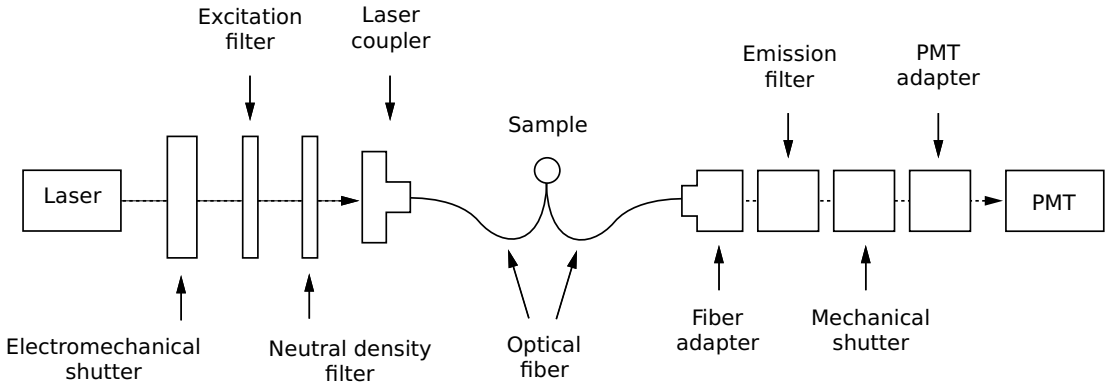


Figure 3.2: Fiber optical setup.

## 3.2 Fiber optical setup

Figure 3.2 schematically illustrates the fiber optical setup. The excitation light is supplied by a dual line (491 nm and 532 nm) continuous wave solid state laser (Cobolt Dual Calypso, Cobolt SA, Sweden), which is focused onto a fused silica fiber by the laser coupler to couple the laser light into the fiber. The fiber is then directed onto the sample by micromanipulators (Narishige, Japan). A second fiber can be positioned close to the first one to collect the emission light. The other end of the detection fiber is held in place by the fiber adaptor. The fluorescence emission light then passes the emission filter to block any excitation light that managed to enter the fiber before it is detected by a photomultiplier. An electromechanical shutter (Uniblitz LS 2, USA) allows to block the excitation light in synchronization with the experiment to reduce bleaching effects and phototoxic reactions of the sample. Opening and closing times of the shutter are in the order of a few ms. To select the desired laser line, appropriate bandpass filters can be placed into the beam path (excitation filters z488/10 for the 491 nm line and z532/10 for the 532 nm line, respectively; emission filter HQ510/20; all from Chroma Technology, USA). To adjust the laser intensity to optimum levels, a variable neutral density filter (Newport, USA) is placed in the beam path. Laser intensities were measured either with a CCD camera (Basler 102f, Germany) or with a power meter (Advantest TQ 8210, Japan).

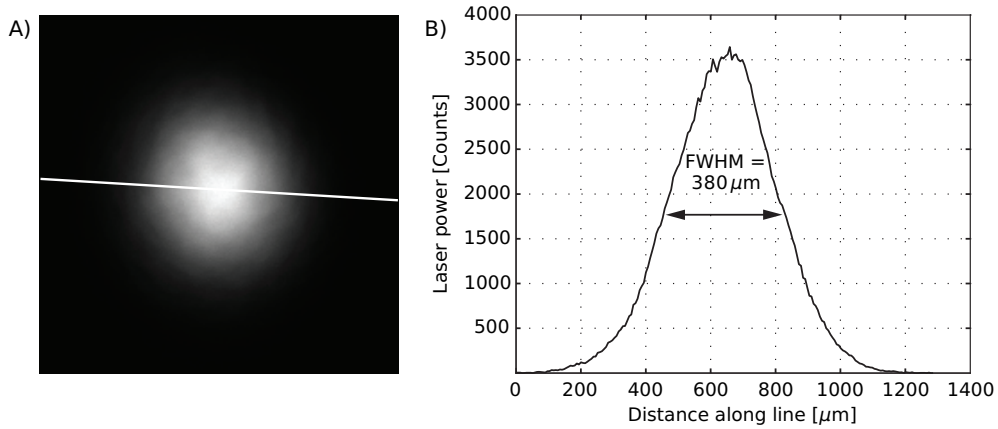


Figure 3.3: Beam profile of the laser at 491 nm. A) Image of the laser beam that was pointed directly onto the CCD chip. B) Beam profile along the white line in A.

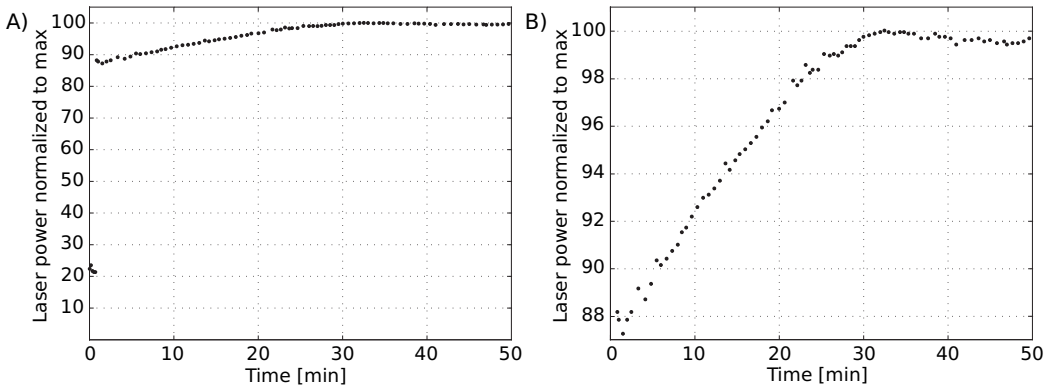


Figure 3.4: Laser power at 491 nm as a function of time. A) Laser power between 0 and 100 % over a time course of 50 min. B) Same data as in A, but cut out between 87 and 100 %.

## 3.2.1 The laser

The continuous wave laser simultaneously emits two lines. One at 491 nm and one at 532 nm with a power of 50 mW per line. The beam thickness at the aperture is 380 $\mu$m FWHM with a beam divergence $\leq$ 1.2 mrad (see figure 3.3 for the gaussian beam profile of the 491 nm line). For the measurement of the beam profile, the laser was maximally attenuated by the circular neutral density filter, and an additional neutral density filter with a transmission of 0.002 % was placed in the beam path before the light was detected by the CCD camera.

After switching on the laser, its output power slowly increases with time and reaches a stable state after about 30 min. Stability is then within $\simeq$ 4 % (see figure 3.4). With active cooling of the laser, stability could probably be further increased. All subsequent measurements were carried out after the laser had reached its stable state.

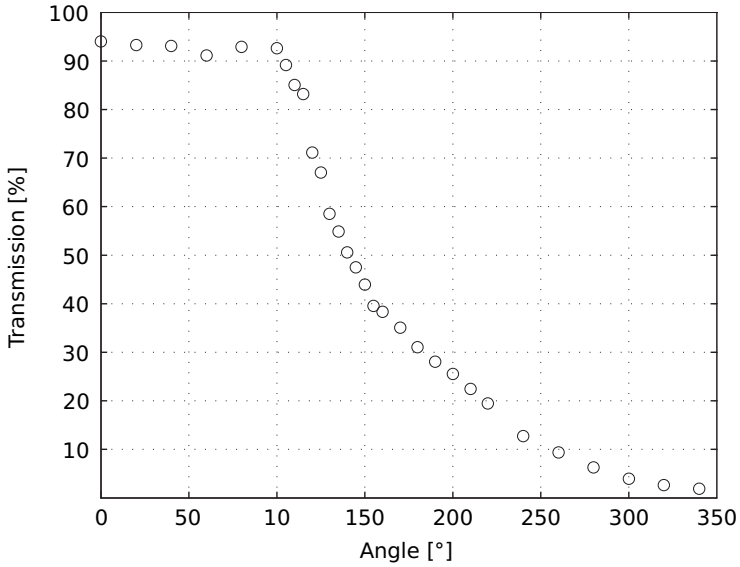


Figure 3.5: Transmission spectrum of the neutral density filter at 491 nm as a function of angular filter position.

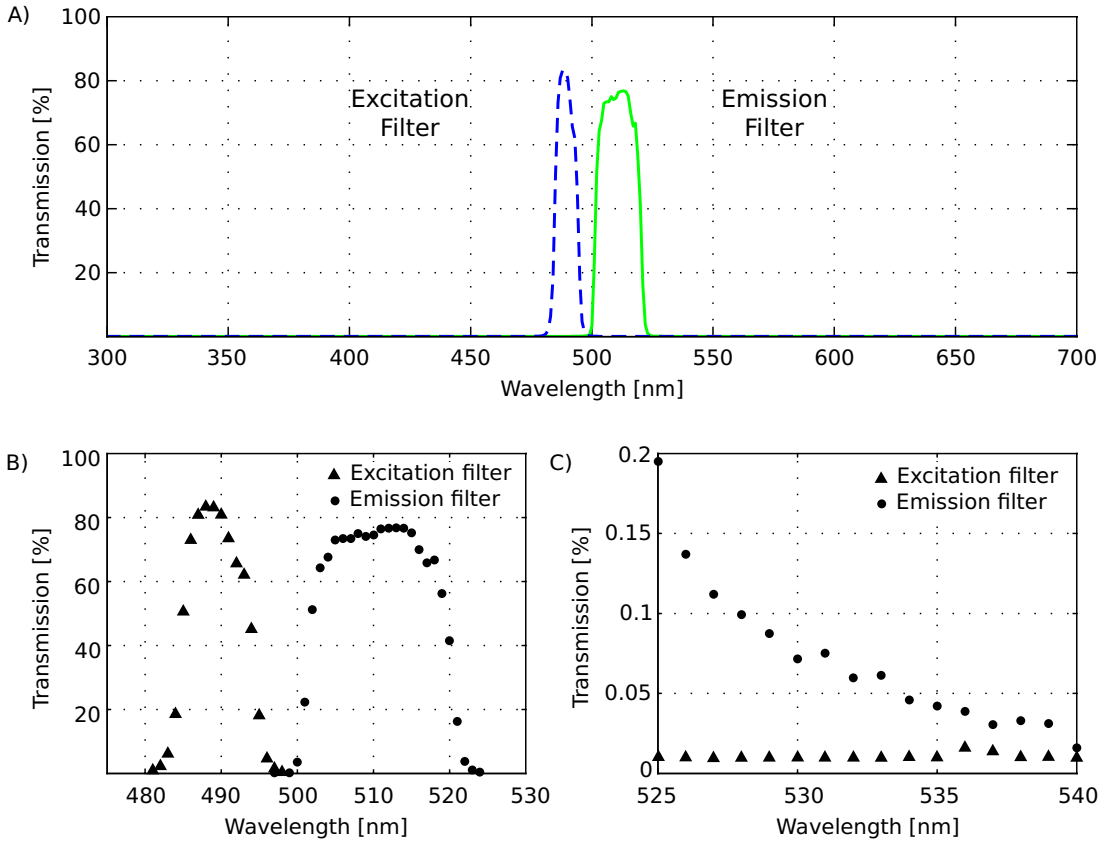


Figure 3.6: Transmission spectra of the excitation and emission filters used in the fiber optical setup. A) Transmission between 300 nm and 700 nm. B) Transmission between 475 nm and 530 nm. C) Transmission between 525 nm and 540 nm. Note the different scaling of the ordinate.

### 3.2.2 The filters

The neutral density filter is a circular aluminum coated reflective filter that allows to adjust the laser intensity continuously between 1 % and 95 % over an angular range of 220° (see figure 3.5 for transmission characteristics).

The transmission spectra of the excitation filter which is used to select the 491 nm line, as well as the transmission spectra of the emission filter are shown in figure 3.6. Because of the high laser power and the fact that the laser simultaneously emits at 491 nm and at 532 nm, it is crucial that both the excitation and the emission filter sufficiently block the 532 nm line. Separate measurements with higher resolution have been performed to specify the transmission of both filters at 532 nm and at 488 nm for the emission filter. At 532 nm the transmission was found to be in the order of 0.01 % and of 0.06 % for the excitation and emission filters, respectively. Therefore, even if the 491 nm line directly passes both filters, only $6 \times 10^{-4}$ % of the incident light is transmitted, which corresponds to a power of 0.12 mW at the position of maximum transmission of the neutral density filter. The transmission of the emission filter at 488 nm was found to be 0.04 %, which is sufficient to block any excitation light that is reflected into the detection fiber (data not shown).

### 3.2.3 The laser coupler

The point at which the laser light impinges the fiber is one of the most critical parts of the setup, as it determines how much light can be coupled into the fiber. The laser coupler consists of an objective (magnification 20×, focal length 8 mm, NA = 0.4), that focuses the laser beam onto the front of the fiber. Additionally, it provides a mechanism, which holds the fiber firmly in place and allows to move the fiber front precisely into and along the focal plane of the objective. Correct alignment of the fiber is not only important to maximize the transmitted laser intensity, but also to optimize the beam profile (see figure 3.8, A and B, page 88). The holding mechanism consists of a plastic pipe into which the fiber is inserted. The plastic pipe can be compressed by a jaw chuck which fixes the fiber inside the plastic pipe. It was found that the plastic gives rise to a large autofluorescence signal which is a typical feature of many plastics. For this reason it was replaced by a stainless steel pipe which the fiber was glued into with polyvinylalcohol. This reduced the autofluorescence of the system by 15 %.

In figure 3.14, page 91, the full angle under which the light leaves the fiber is $\simeq 27°$. The acceptance angle is then at least 13.5°, and following equation 3.3 the lower limit of the numerical aperture calculates to $\simeq 0.23$. Because the laser has a beam waist of approximately 800 $\mu$m and the focal length of the focusing objective is 8 mm, the maximum angle under which light impinges onto the fiber is 2.9°, a value well below the acceptance angle.

### 3.2.4 Optical fibers

Four different fibers were evaluated for use in the setup (fiber #1–#3 from Fiberoptic, Switzerland, and fiber #4 from Fibertech, Germany, see table 3.1 for specifications). All fibers were made of fused silica.

In order to characterize the autofluorescence properties of the optical fibers, they were mounted on a fused silica glass slide with their axis running parallel to the glass surface. In this configuration the fibers were imaged with the fluorescence microscopy setup as described in figure 2.6, page 52. Excitation light was in the spectral region from 450 nm to 490 nm and the fluorescence emission was detected between 500 nm and 550 nm by a CCD camera.

The level of autofluorescence of fibers #1 and #2 was just slightly above the background signal, while fibers #3 and #4 showed a very large autofluorescence signal (see figure 3.7). The origin of the peak in figure 3.7C is unclear.

During the initial measurements the fibers were excited from the outside by the internal Hg lamp of the microscope. In a second experiment, the 491 nm laser line was coupled into the fiber and the fiber fronts were imaged by the same microscope without using the internal Hg lamp of the microscope (see figure 3.8). These images reveal even more relevant information about the fluorescence originating from the setup, because this is the

| | Core diameter [$\mu$m] | Cladding thickness [$\mu$m] |
|---|---|---|
| Fiber #1 | 18 | 1.0 |
| Fiber #2 | 27 | 1.5 |
| Fiber #3 | 63 | 3.5 |
| Fiber #4 | 50 | 9.0 |

Table 3.1: Core and cladding dimensions of the tested fibers.

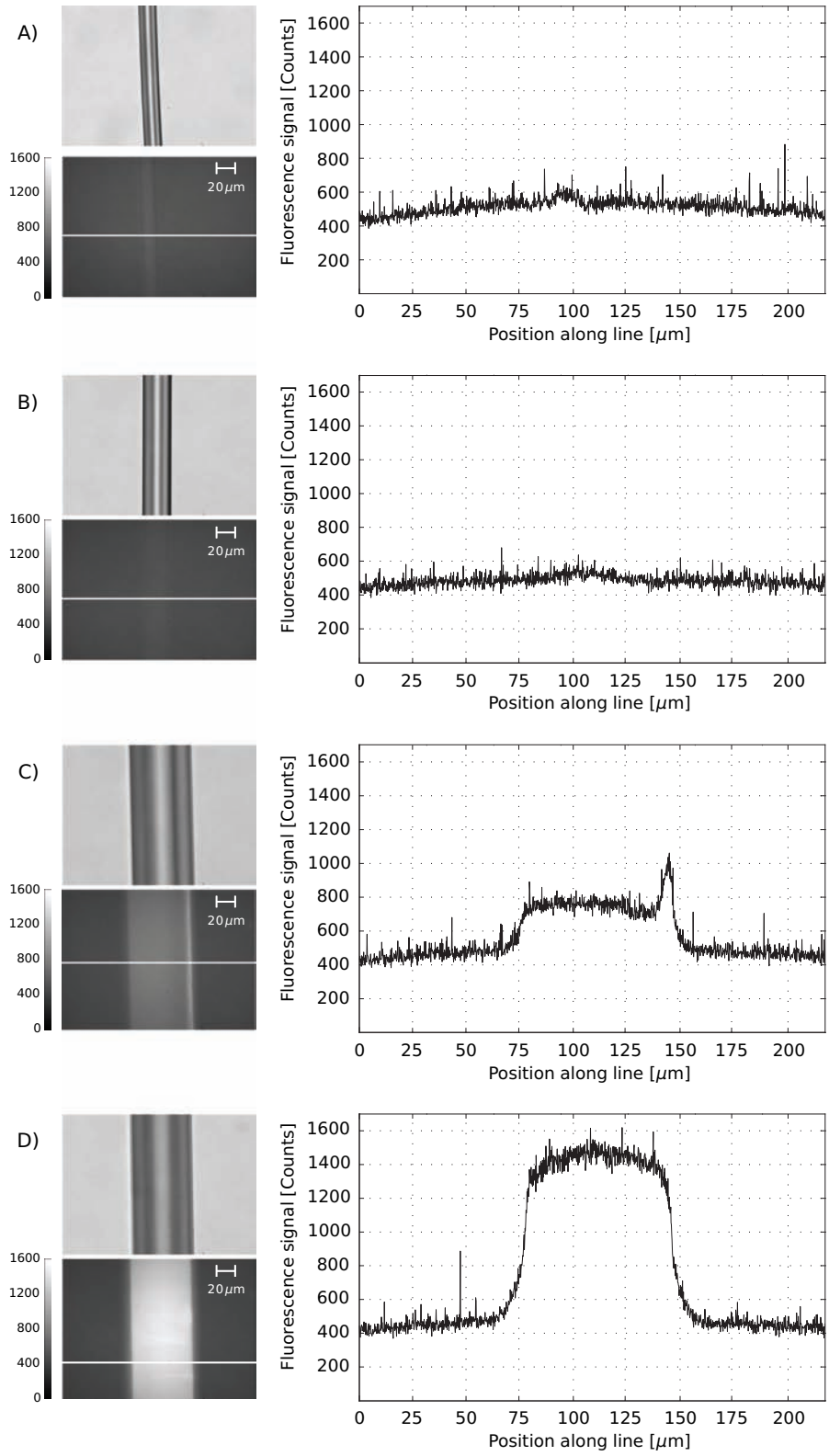


Figure 3.7: Autofluorescence of fibers as seen by fluorescence microscopy with eGFP filter block #41017 (see figure 2.7, page 54, for transmission characteristics). For each fiber two images are shown: 1) a transmission light microscopy image and 2) a fluorescence image. The intensity profile along the white line in the fluorescence image is shown on the right. A) Fiber #1: $\varnothing = 20\,\mu$m; B) Fiber #2: $\varnothing = 30\,\mu$m; C) Fiber #3: $\varnothing = 70\,\mu$m; D) Fiber #4: $\varnothing = 70\,\mu$m.

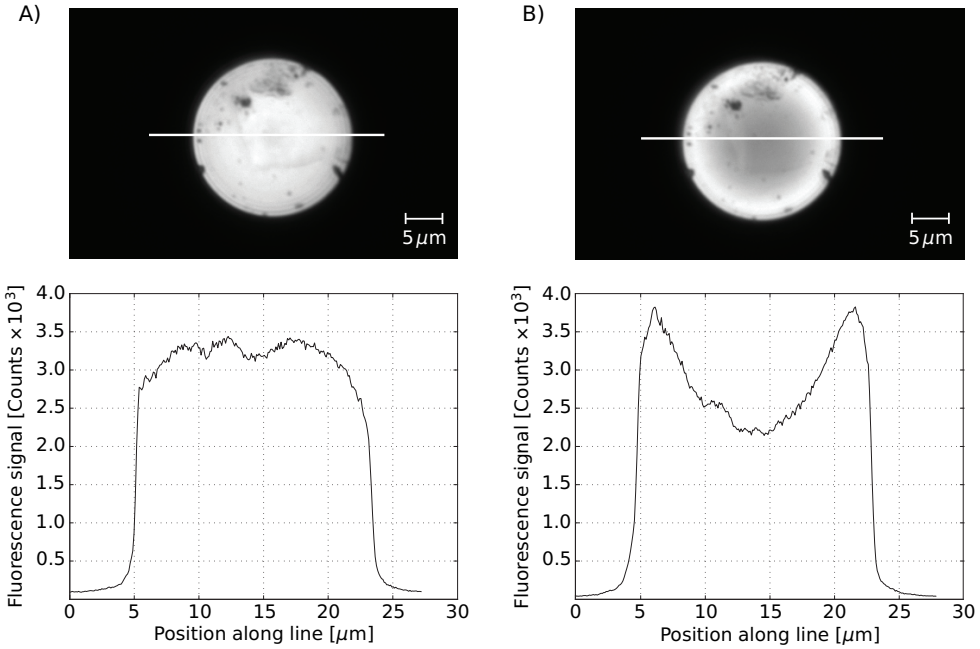


Figure 3.8: Autofluorescence of fiber fronts as seen by fluorescence microscopy with eGFP filter block #41017 (see figure 2.7, page 54). Upper section: fluorescence microscopy images of fiber fronts; lower section: intensity profiles along the white line drawn on the fluorescence images. Both images show the same fiber. A) Laser axis and fiber axis in–line. B) Laser axis and fiber axis off–line. (see text for explanation)

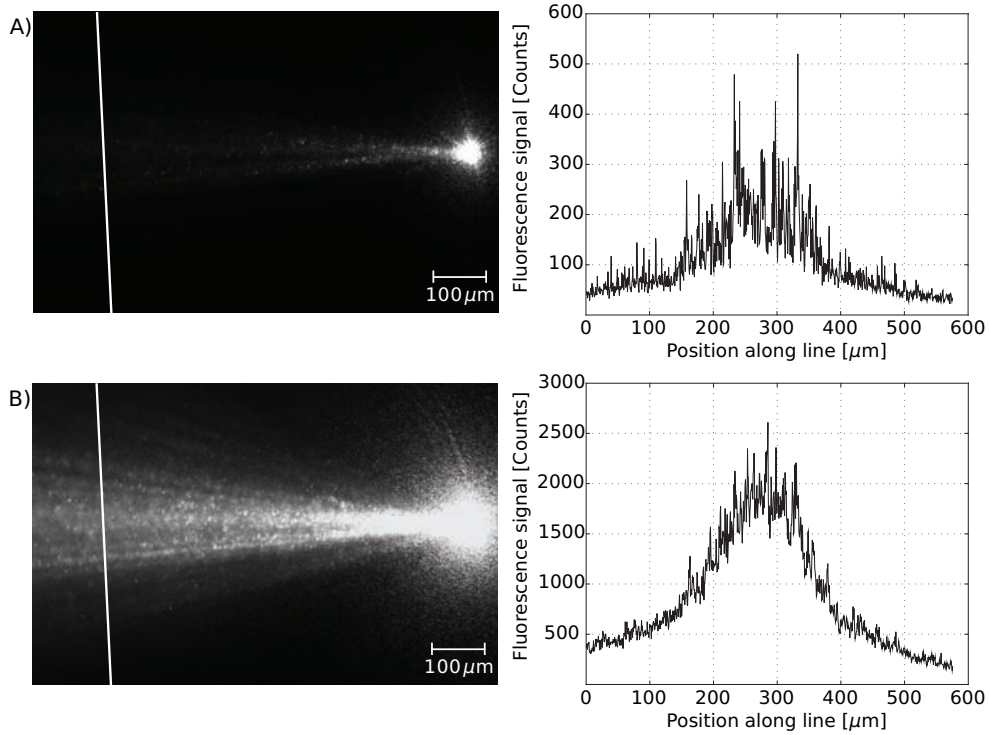


Figure 3.9: Beam profile of broken fiber. The fiber end is immersed into a strongly diluted milk emulsion. The fiber axis runs parallel to the image plane. A) Low illumination intensity; B) High illumination intensity. Note the different scaling of the ordinate.

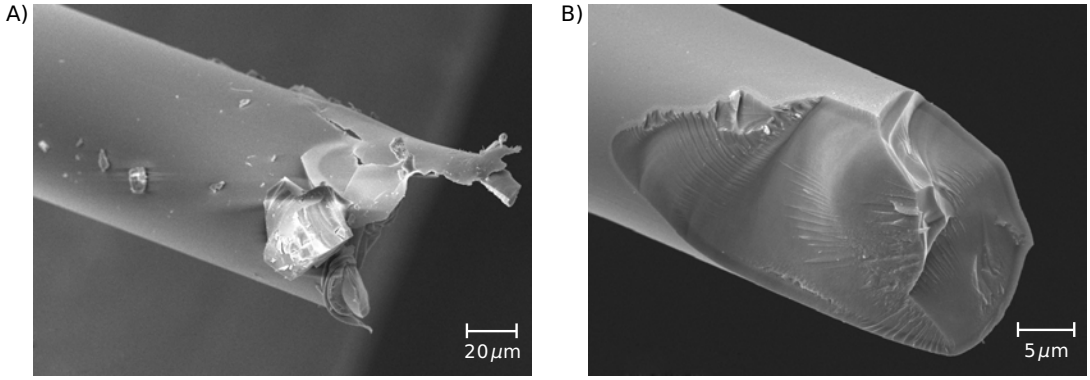


Figure 3.10: Scanning electron microscope images of broken fiber ends. A) Fiber with diameter $\varnothing = 70\,\mu$m; B) Fiber with diameter $\varnothing = 20\,\mu$m.

configuration the system is normally operating in. As before, fiber #4 gave rise to the highest level of autofluorescence and fiber #1 to the lowest level. Normalized to the value obtained for fiber #4, the values were: fiber #1: 6%; fiber #2: 14%; fiber #3: 40%; fiber #4: 100% (data not shown). Consequently, in all subsequent measurements fibers of type #1 were used.

The images in figure 3.8 also reveal that correct alignment of the laser beam is critical: The intensity distribution of the autofluorescence at the fiber front changes dramatically when the beam axis and the fiber axis are not perfectly in–line.

In order to characterize the shape of the light beam exiting the fiber end, images of the light emitting fiber were taken without employing any fluorescence filters in the beam path. Fibers were mounted on a glass slide and immersed into a strongly diluted milk emulsion with their axis parallel to the image plane. The scattered light makes the beam path visible (see figure 3.9). As the light exits the fiber, it is strongly scattered and only a small fraction transverses in a narrow cone along the fiber axis. It should be noted that in the images shown in figure 3.9 the CCD chip is saturated in the region close to the fiber end. This is due to the extremely uneven surface of the fiber front (see 3.10 for scanning electron microscopy (SEM) images of fiber fronts). Because of the high autofluorescence of the fibers, their length was minimized as far as the setup allowed ($\simeq 10-20\,$cm). Different methods to adjust their length were tried (cutting with scissors or scalpels, pulling, breaking), all of them resulted in highly uneven surfaces similar to the ones seen in figure 3.9. Only about 25% of the total laser intensity could be coupled into the fiber with this method. Therefore, a method was developed to flatten the fiber fronts.

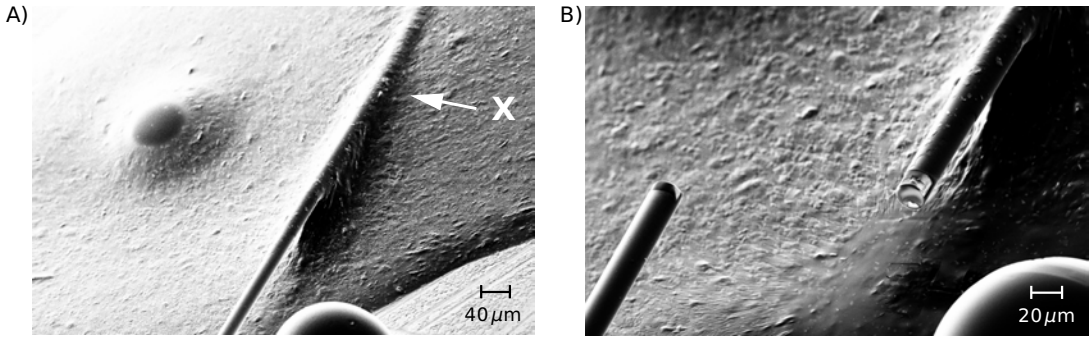


Figure 3.11: Scanning electron microscope images of the fiber on the holder. The fiber was set under tension with a copper wire and glued onto the holder (see text and figure 3.12). A) Before cutting the fiber with the focused ion beam. The position indicated with X corresponds to the position marked with X in figure 3.12. B) Fiber after it was cut with the focused ion beam.

## 3.3 Flattening of fiber fronts by use of a focused ion beam

In order to optimize the coupling efficiency and the profile of the exiting beam, the fiber fronts were manipulated with a *focused ion beam*[2] (FIB). A FIB is typically used to modify the surface of specimen at the $\mu$m– or nm–scale. To cut the relatively thick fibers ($\varnothing = 20\,\mu$m) normal to its axis, a simple spring mechanism was used to set it under tension: one end of a thin copper wire was welded onto a stainless steel plate in such way that the wire axis ran parallel to the plate surface (see figures 3.11 and 3.12). Then, the fiber was fixed to the free end of the copper wire with a drop of conductive silver. Once the conductive silver had dried out, the fiber was set under tension by pulling the fiber and thereby bending the wire. Another drop of conductive silver allowed to fix the fiber and thereby to retain the tension which was applied to the fiber. The mounted fiber was coated with gold before the ion beam was focused on the fiber in a region between the two mounting points X and Z indicated in figure 3.12. The focused ion beam was then scanned over

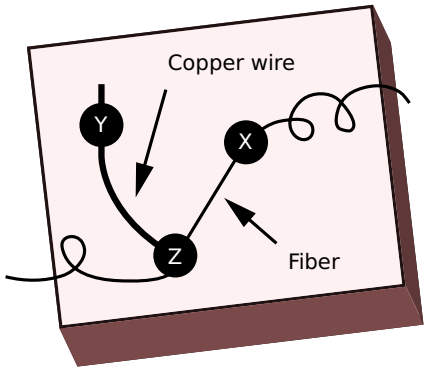


Figure 3.12: Fiber mount as seen from the top. The black spots at positions X, Y and Z indicate drops of conductive silver. At positions X and Y the wire and the fiber are fixed onto the holder. At point Z the fiber is fixed to the copper wire. Point X corresponds to point X in figure 3.11.

[2]The principle of a focused ion beam is identical to a scanning electron microscope but instead of electrons, ions are used to image the sample. In the present study $Ga^+$ ions were used. Because these ions are much heavier than electrons, the deposited energy is much greater and consequently the radiation damage will be more severe than if electrons were used. Upon hitting the surface the $Ga^+$ ions will sputter atoms from the surface of the sample. This effect can be used to apply fine structures on the sample.

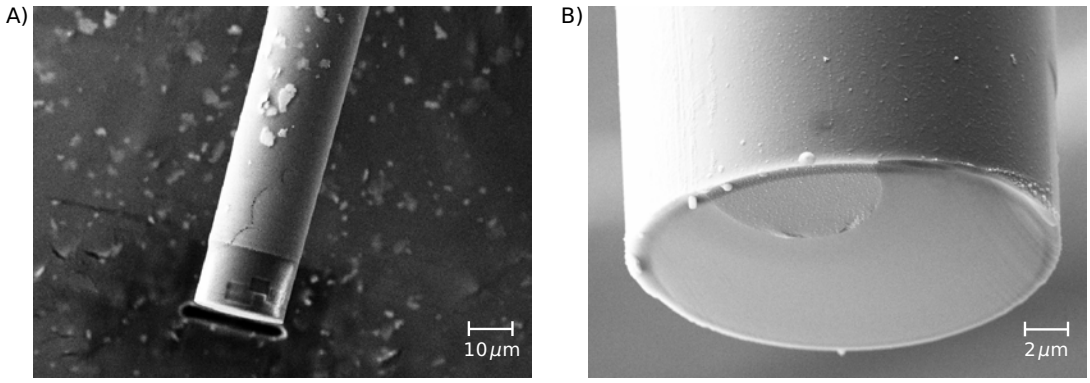


Figure 3.13: Scanning electron microscope images of a fiber cut with focused ion beam ($\varnothing = 20\,\mu$m). A) The dark shading at the front of the fiber is an artifact due to charging effects and to the loss of the gold coating. B) Same fiber as in A which was coated with gold once more before imaging. The rough region in the upper part of the fiber is the point of rupture.

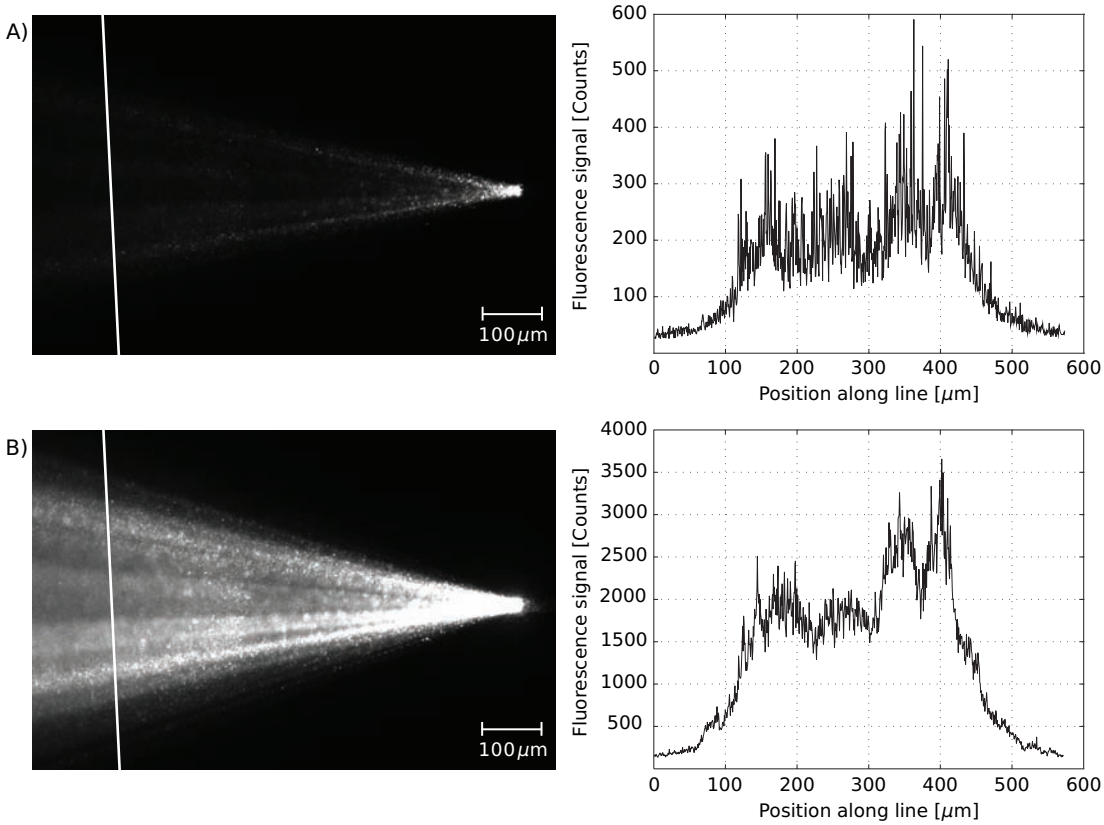


Figure 3.14: Beam profile of fiber cut with a focused ion beam. A) Low illumination intensity; B) High illumination intensity. Note the different scaling of the ordinate. See figure 3.9, page 88, for comparison with broken fiber.

the whole width of the fiber normal to its axis. The thickness of the scan region in the direction of the fiber axis was $\simeq 1\,\mu$m. As more and more atoms are sputtered from the fiber, the fiber weakens until at some point it cannot withstand the tension applied by the wire spring. At this point, the fiber breaks apart, leaving behind relatively even fiber front surfaces (see 3.13 for SEM images).

Just as with the broken fibers, the quality of the light beam exiting the fiber end was characterized by taking images of the light emitting fiber without placing any fluorescence filters into the beam path. Again, the fibers were mounted on a glass slide and immersed into a strongly diluted milk emulsion with their axis parallel to the image plane (see figure 3.14). Close to the fiber front, scattering of the exiting light is now much weaker and most of the light transverses in a narrow cone with an opening angle of $\simeq 27°$ along the fiber axis. It should be noted, that in the image presented in figure 3.14 the CCD chip is saturated in the region close to the fiber end.

Fibers whose fronts were flattened by use of the focused ion beam showed an increased coupling efficiency. The laser light was coupled into the fiber and the intensity of the transmitted light was measured at the other end. This intensity was determined to be $\simeq 35\,\%$ of the total laser power when the entrance front only was flattened and $50\,\%$ when both ends were flattened. This corresponds to an increase of factor 1.4 and 2, respectively, when compared to a fiber with broken fiber end.

## 3.4 Fluorescence saturation

In wide–field microscopy, fluorescence saturation is rarely a problem, because the excitation intensity is relatively small. However, as the excitation power increases, the ground state $S_0$ of fluorophores can become depleted. This effectively limits the maximum photon emission rate.

In a good approximation, the energy states of a fluorophore can be characterized by the ground state $S_0$, the first excited singlet state $S_1$ and the first excited triplet state $T_1$ (see

figure 2.5, page 51). The transition rates $\omega_{ij}$ may be specified as follows:

| | | |
|---|---|---|
| $\omega_{01}$ | for the transition | $S_0 \rightarrow S_1$ |
| $\omega_{10}$ | for the transition | $S_1 \rightarrow S_0$ |
| $\omega_{12}$ | for the transition | $S_1 \rightarrow T_1$ |
| $\omega_{20}$ | for the transition | $T_1 \rightarrow S_0$ |

With this nomenclature, the relation between the occupation numbers $N_0$, $N_1$ and $N_2$ of the states $S_0$, $S_1$ and $T_1$, respectively, and the transition rates $\omega_{01}$, $\omega_{10}$, $\omega_{12}$ and $\omega_{20}$ may be described in a set of differential equations:

$$\begin{aligned} \frac{\mathrm{d}N_0}{\mathrm{d}t} &= -\omega_{01} N_0 + \omega_{10} N_1 + \omega_{20} N_2 \\ \frac{\mathrm{d}N_1}{\mathrm{d}t} &= \omega_{01} N_0 - (\omega_{10} + \omega_{12}) N_1 \\ \frac{\mathrm{d}N_2}{\mathrm{d}t} &= \omega_{12} N_1 - \omega_{20} N_2 \end{aligned} \tag{3.4}$$

It seems reasonable to assume that fluorescence emission dominates over intersystem crossing and phosphorescence in a typical fluorophore. As a consequence, it holds true that $\omega_{10} \gg \omega_{12}$ and $\omega_{10} \gg \omega_{20}$. Under these conditions, a solution of equations 3.4 for the occupation number of the first excited singlet state is given by [115]:

$$\begin{aligned} N_1(t) = \frac{\omega_{01}\beta}{\omega_{01}+\beta\omega_{10}} - \frac{\omega_{01}}{\omega_{01}+\omega_{10}} \Bigg( & \exp\left[-(\omega_{01}+\omega_{10})\,t\right] + \\ & \frac{\omega_{01}(1-\beta)}{\omega_{01}+\beta\omega_{10}} \exp\left[-\frac{\omega_{01}(\omega_{12}+\omega_{20})+\omega_{10}\omega_{20}}{\omega_{01}+\omega_{10}}\,t\right] \Bigg) \\ \text{with } \beta := \frac{\omega_{20}}{\omega_{20}+\omega_{12}} & \end{aligned} \tag{3.5}$$

The pathway of bleaching processes typically originates from the triplet state $T_1$ (see section 2.3.2, page 52). Therefore, the transition rate $\omega_{20}$ vanishes if bleaching effects can be neglected. If additionally the observation time is kept between $1/\omega_{10} < t < 1/\omega_{12}$ then equation 3.5 takes the simple form:

$$N_1(t) \simeq \frac{\omega_{01}}{\omega_{01}+\omega_{10}} \tag{3.6}$$

The fluorescence rate is the ratio between the occupation number $N_1$ of the first excited state $S_1$ and the excited state lifetime $\tau$. If the cross section of the absorption process is $\sigma$, the energy of the incident photons $E_\gamma$ and the intensity of the incident light beam $I$, then $\omega_{01} E_\gamma = I\sigma$. Together with equation 3.6 the fluorescence rate can then be written as:

$$F = \frac{N_1}{\tau} \simeq \frac{1}{\tau} \frac{I\sigma}{I\sigma + \omega_{10} h\nu} = \frac{1}{\tau} \frac{1}{1 + \omega_{10} h\nu / I\sigma} \tag{3.7}$$

If the excitation intensity reaches sufficiently large values, the fluorescence emission approaches a constant value, the saturation fluorescence $F_\infty$:

$$F_\infty := \lim_{I \to \infty} F = \frac{1}{\tau}$$

The saturation intensity $I_s$ is defined as the intensity for which the fluorescence emission reaches half of the saturation value. Using equation 3.7, the fluorescence rate can be expressed as a function of the saturation fluorescence and the saturation intensity:

$$F = \frac{F_\infty}{1 + I_s / I} \tag{3.8}$$

In order to further characterize the present fiber optical setup a preliminary experiment on the saturation of eGFP was performed.

## 3.5 Bleaching and saturation of eGFP

A fused silica glass slide was mounted flat on the microscope. A second glass slide was placed on top of the first, separated by 20 $\mu$m from the first slide. The volume between the two glass slides was filled with an eGFP containing solution of a concentration of 25 $\mu$M. In order to excite the fluorophores, laser light of a wavelength of 491 nm was coupled into an optical fiber. The other end of the fiber was directed between the two glass slides with the fiber axis parallel to the plane of the glass slides. The fluorescence emission light was collected by a 40× objective, NA = 0.6, and imaged onto a CCD camera. An emission filter was used to select for the appropriate region of the spectrum between 500 nm and 550 nm (see figure 2.7 C, page 54, for transmission characteristics).

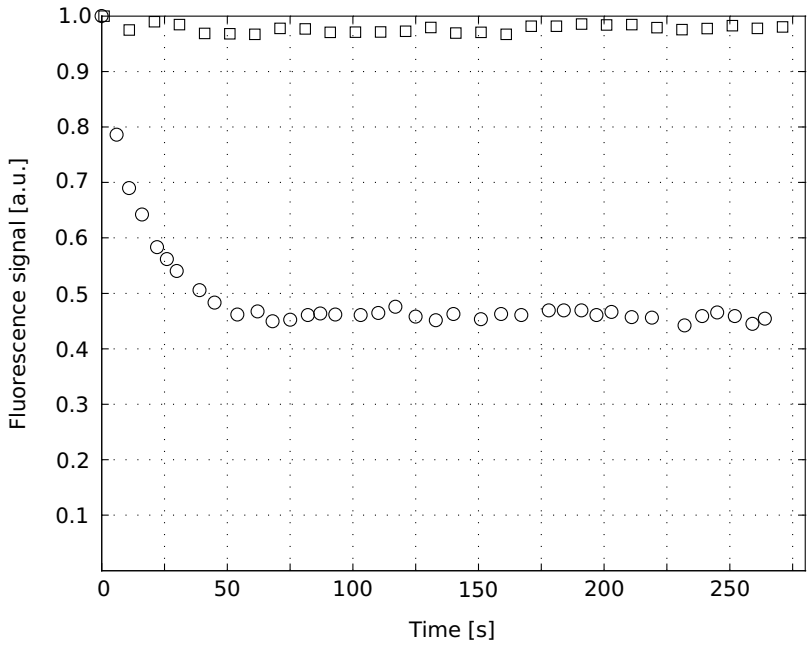


Figure 3.15: Bleaching of an eGFP containing solution excited at 491 nm with an excitation intensity of $\simeq 3\,\mathrm{kW/cm^2}$; continuous irradiation (circles); irradiation every 10 s for a duration of 10 ms (squares).

## Bleaching of eGFP

Initial tests were performed to find out whether or not bleaching effects are significant. The mean excitation intensity as measured directly at the fiber front was $\simeq 3\,\mathrm{kW/cm^2}$. When the eGFP solution was excited continuously with this excitation intensity, a typical fluorescence decay as seen in figure 3.15 was observed. The plateau that is reached after $\simeq 50$ s is due to the autofluorescence of the fiber and to reflections of the excitation light at the surfaces of the glass slides.

In a second experiment the eGFP solution was excited every 10 s for a duration of 10 ms. In this case, the fluorescence signal stayed constant for at least 5 min (see figure 3.15). The 10 s of darkness between the excitation pulses allow for non–bleached eGFP molecules to diffuse into the excitation volume. Therefore, the concentration of non–bleached eGFP molecules barely changes over time.

## Saturation of eGFP

The experiment on the saturation of eGFP was performed in the same manner as the second experiment described in the last section: the eGFP containing solution between the

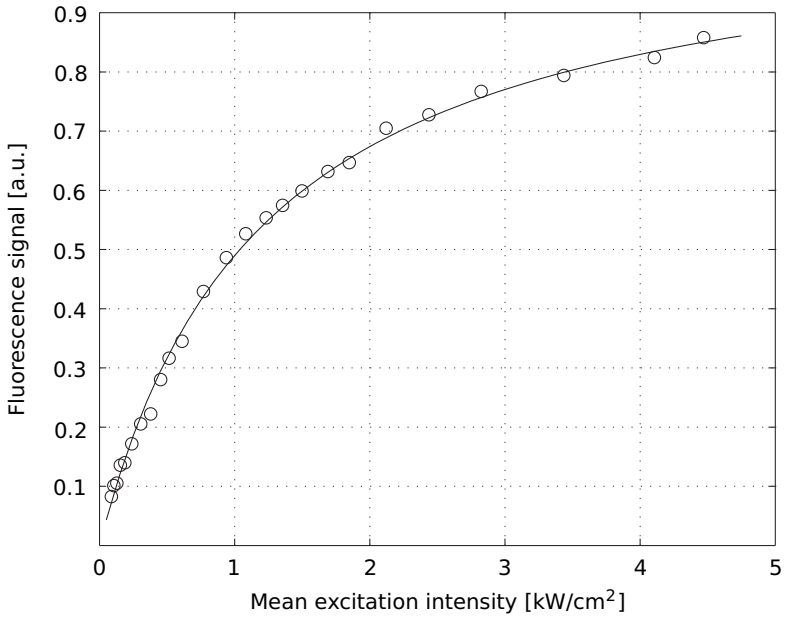


Figure 3.16: eGFP fluorescence as a function of mean excitation intensity. The solid line is a $\chi^2$ fit of function 3.9 to the data.

two glass slides was excited for a duration of 10 ms every 10 s. For this reason, bleaching effects could be neglected. Equation 3.8 describes the fluorescence emission as a function of the excitation intensity if additionally the detection efficiency of the system is taken into account. Due to unknown reasons the beam profile of excitation light leaving the fiber was very irregular (see figure 3.17). Therefore, mean excitation intensities only could be determined. The saturation curve for eGFP fluorescence is shown in figure 3.16. The solid line in figure 3.16 is a $\chi^2$ fit to the raw data of the function:

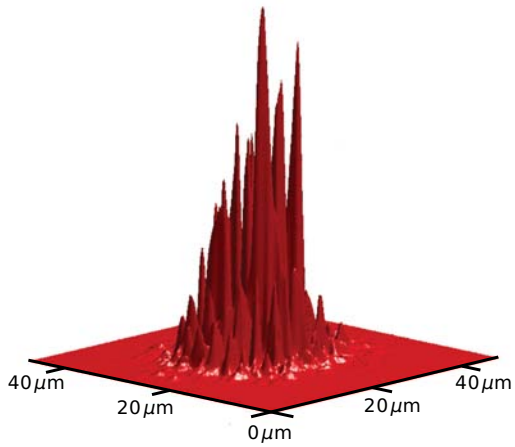


Figure 3.17: Relative intensity of the excitation light at the fiber front.

$$F = \frac{c_1}{1 + c_2/I} \tag{3.9}$$

rather than a fit of the function described in equation 3.8. The obtained fitting parameters are $c_1 = 1.1$ and $c_2 = 1.2\,\mathrm{kW/cm^2}$ with a reduced $\chi^2 = 1.1$.

Because the mean excitation intensity only could be determined and because the detection efficiency of the fiber optical system was not taken into account, the obtained value of $1.2\,\mathrm{kW/cm^2}$ does not reflect the intrinsic saturation intensity of enhanced green fluorescent proteins. However, it characterizes a property of the setup. For further experiments on the fluorescence characteristics of eGFP, the beam profile has to be optimized and the detection efficiency of the system has to be determined.

In the context of the present fiber optical system, it could be established that saturation effects of eGFP play a significant role even at relatively low mean excitation intensities in the order of $\simeq 1\,\mathrm{kW/cm^2}$.

## 3.6 Conclusions

It has been demonstrated that even rather large objects can readily be manipulated with a focused ion beam. It has been possible to cut an optical fiber with a diameter of 20$\mu$m normal to its axis. The optical properties of the obtained surface is by far superior to a surface obtained by breaking or pulling the fiber: the coupling efficiency could be doubled. Light that leaves the fiber stays confined within a solid angle of $\simeq 0.17\,\mathrm{sr}$, if the surface of the fiber end is manipulated with the focused ion beam. The corresponding solid angle of a fiber with a broken surface is about 30 times larger. The present approach aiming at the modification of optical fiber ends could further be expanded to improve the fiber properties: it could be possible to manufacture fiber ends with special lens geometries. The acceptance angle could supposably be further enlarged, thereby improving the coupling efficiency. Furthermore, with a different geometry, light exiting the fiber could be collimated or focused to increase the intensity in the excitation volume.

The detection of the fluorescence emission of single green fluorescent proteins was not possible because of the high level of autofluorescence of the used fibers. For the further development of the present setup, it is necessary to test and characterize the autofluorescence of other fiber types. Besides eGFP, there are many other fluorescent proteins with different spectral properties. It would thus be of interest to classify fibers by their spectral properties and to check whether other fluorophores are compatible with them.

Fluorescence saturation can be a limiting factor in fluorescence microscopy. The present fiber optical setup holds the capacity to deliver mean intensities of $\simeq 5\,\mathrm{kW/cm^2}$ at 491nm in close vicinity to the fiber end. As has been shown, even with this relatively low intensity, significant saturation effects arise which have to be taken into account for quantitative measurements.

Optical fibers provide a fairly simple means to locally excite fluorophores. However, for the setup to be able to detect single fluorophores, suitable fibers have first to be found or developed.

# A The multi–state model of channel gating

In the following pages the two–state and the multi–state models of channel gating are discussed. The logarithmic potential sensitivity (LPS) and the fraction of opened states as a function of membrane potential are determined.

## The two–state model

In the most simple approach a channel can be described as having one closed and one open state:

$$A \overset{\Delta\mu}{\rightleftharpoons} B$$

Assuming that the channel protein sits firmly in the lipid (i.e., can not move as a whole), it must change its overall dipole moment when it switches from the closed to the open state. $\Delta\mu$ is the component of this change normal to the membrane.

In equilibrium, the channel has a certain (and constant) conductivity which is dependent on the membrane potential. From thermodynamic principles it follows that the fraction of opened to closed channels $K$ (the equilibrium constant) is equal to:

$$\frac{\mathrm{d}}{\mathrm{d}E}\Big[\ln K\Big] = \frac{\Delta\mu(E)}{k_B T} \tag{A.1}$$

where $E$ is the electric field, $k_B$ is Boltzmann's constant and $T$ the absolute temperature.

The distance over which the electric field spans is not known and hence neither is the electric field. With the definition

$$\Delta\overline{\mu}(V) := \frac{\Delta\mu(E)}{\delta}$$

where $\delta$ is the distance over which the electric field spans, equation (A.1) can be reformulated:

$$\frac{\mathrm{d}}{\mathrm{d}V}\Big[\ln K\Big] = \frac{\Delta\overline{\mu}(V)}{k_B T} \tag{A.2}$$

This is an expression for the LPS which depends on the potential rather than on the electric field. The potential can be determined experimentally whereas the electric field is not known. $\Delta\mu$ is a component of a dipole moment, and therefore $\Delta\overline{\mu}$ is a charge. It is the charge that has to be moved across the membrane for the channel to switch from the closed to the open state.

May $a$ and $b$ be the fractions of channels in the closed and open state, respectively. If we assume for the sake of simplicity that $\Delta\overline{\mu}(V)$ is constant over the range of relevant voltages ($\Delta\overline{\mu}(V) = \Delta\overline{\mu} = q$), equation (A.2) can be rearranged and integrated:

$$\begin{aligned} \ln K &= \int \mathrm{d}\left[\ln K\right] = \int \frac{q}{k_B T}\,\mathrm{d}V = \frac{q}{k_B T}\int \mathrm{d}V = \frac{q}{k_B T}V + c \\ \Longrightarrow \quad K &= \exp\left[\frac{q}{k_B T}V + c\right] \end{aligned} \tag{A.3}$$

where c is a constant. If we set $\overline{V}$ as the potential where the number of closed and opened channels is equal ($\rightarrow K(\overline{V}) = b/a = 1$) it follows:

$$\begin{aligned} K\left(\overline{V}\right) &= \exp\left[\frac{q}{k_B T}\overline{V} + c\right] \stackrel{!}{=} 1 \\ \Longrightarrow \quad \frac{q}{k_B T}\overline{V} + c = 0 \quad &\Longrightarrow \quad c = -\frac{q}{k_B T}\overline{V} \\ \Longrightarrow \quad K &= \exp\left[\frac{q}{k_B T}\left(V - \overline{V}\right)\right] \end{aligned} \tag{A.4}$$

With equation (A.3) and the fact that $a + b = 1$, the fraction of opened channels can be expressed as:

$$b = \frac{1}{1 + \exp\left[-\frac{q}{k_B T}\left(V - \overline{V}\right)\right]}$$

## The multi–state model

In the multi–state model it is assumed that various closed states can be occupied by the channel, each associated by the movement of some charge. Upon membrane depolarization the channel undergoes various closed states $A_0, A_1, \ldots, A_n$, each changing the dipole moment equivalent to a charge movement $q_0, q_1, \ldots, q_n$ through the whole potential drop across the membrane until it reaches the open state $B$:

$$A_0 \overset{q_0}{\longleftrightarrow} A_1 \overset{q_1}{\longleftrightarrow} A_2 \cdots\cdots A_n \overset{q_n}{\longleftrightarrow} B$$

The total gating charge is the sum of the individual charges:

$$q = q_0 + q_1 + \cdots + q_n$$

If the fraction of channels in the closed states $A_i$ is $a_i$ and the fraction of channels in the open state $B$ is $b$, then with equation (A.4) it holds true that:

$$\frac{a_{i+1}}{a_i} = e^{w_i} \quad \Longrightarrow \quad a_i = a_{i+1} e^{-w_i}, \qquad i = 1, 2, \ldots, n-1 \tag{A.5}$$

$$a_n = b\, e^{-w_n}, \qquad i = n \tag{A.6}$$

$$\text{with } w_i := \frac{q_i \left[ V - \overline{V}_i \right]}{k_B T}, \quad i = 1, 2, \ldots, n \tag{A.7}$$

where $w_i$ is the work required to move the charge $q_i$ across the membrane. The sum of all fractions must be equal to unity:

$$\sum_{i=0}^{n} a_i + b = a_0 + a_1 + \cdots + a_n + b = 1 \tag{A.8}$$

With equations (A.5) and (A.6) the individual fractions of the closed states $a_i$ can be written as follows:

$$\begin{aligned}
a_n &= b\, e^{-w_n} \\
a_{n-1} &= a_n e^{-w_{n-1}} = b\, e^{-(w_{n-1} + w_n)} = b \exp \sum_{i=n-1}^{n} -w_i \\
a_{n-2} &= a_{n-1} e^{-w_{n-2}} = b \exp \sum_{i=n-2}^{n} -w_i \\
&\vdots \\
a_0 &= b \exp \sum_{i=0}^{n} -w_i
\end{aligned}$$

Therefore the sum of all $a_i$ is:

$$\begin{aligned}\sum_{i=0}^{n} a_i &= b\left[e^{-[w_0+w_1+\cdots+w_n]} + e^{-[w_1+w_2+\cdots+w_n]} + \cdots + e^{-w_n}\right] \\ &= b\left[\exp\sum_{i=0}^{n} -w_i + \exp\sum_{i=1}^{n} -w_i + \cdots + \exp(-w_n)\right] = bD \\ &\text{with } D := \exp\sum_{i=0}^{n} -w_i + \exp\sum_{i=1}^{n} -w_i + \cdots + e^{-w_n}\end{aligned}$$

With equation (A.8) and the definition of $D$ it holds true that:

$$bD + b = 1 \quad \Longrightarrow \quad b = \frac{1}{D+1}$$

The fraction of channels which occupy the open state can now be calculated:

$$\begin{aligned}b &= \frac{1}{D+1}\,\frac{e^{w_0+w_1+\cdots+w_n}}{e^{w_0+w_1+\cdots+w_n}} = \frac{e^{w_0+w_1+\cdots+w_n}}{De^{w_0+w_1+\cdots+w_n} + e^{w_0+w_1+\cdots+w_n}} \\ &= \frac{e^{w_0+w_1+\cdots+w_n}}{1 + e^{w_0} + e^{w_0+w_1} + \cdots + e^{w_0+w_1+\cdots+w_n}}\end{aligned} \tag{A.9}$$

For very negative potentials (which is a prerequisite for the limiting slope analysis) the exponential terms of the denominator approach zero, and the denominator approaches one:

$$b \simeq e^{w_0+w_1+\cdots+w_n} \qquad \text{with } V \ll 0$$

Together with equation (A.7) this can be rewritten:

$$\begin{aligned}b &\simeq \exp\left[q_0\frac{V-\overline{V}}{k_BT} + q_1\frac{V-\overline{V}}{k_BT} + \cdots + q_n\frac{V-\overline{V}}{k_BT}\right] \\ &= \underbrace{\exp\left[-\left[q_0\overline{V}_0 + q_1\overline{V}_1 + \cdots + q_n\overline{V}_n\right]\frac{1}{k_BT}\right]}_{=\text{const}=:C} \exp\left[\underbrace{[q_0+q_1+\cdots+q_n]}_{=:q}\frac{V}{k_BT}\right] \\ &= C\exp\left[\frac{qV}{k_BT}\right] \qquad \text{with } V \ll 0\end{aligned}$$

As in the two–state model, $K$ is defined as the fraction of opened to closed channels

$K := b/(1-b)$. If we furthermore define:

$$x := e^{w_0+w_1+\cdots+w_n} \tag{A.10}$$
$$y := 1+e^{w_0}e^{w_0+w_1}+\cdots+e^{w_0+w_1+\cdots+w_n}$$

$$\Longrightarrow \quad y-x = 1+e^{w_0}+e^{w_0+w_1}+\cdots+e^{w_0+w_1+\cdots+w_{n-1}} \tag{A.11}$$

$$\underset{\text{(A.9)}}{\Longrightarrow} \quad K = \frac{x}{y-x} \quad \Longrightarrow \quad \ln K = \ln x - \ln[y-x] \tag{A.12}$$

The equivalent of equation (A.2) of the two–state model can then be formulated:

$$\begin{aligned}\frac{\mathrm{d}}{\mathrm{d}V}\Big[\ln K\Big] &\underset{\text{(A.12)}}{=} \frac{\mathrm{d}}{\mathrm{d}V}\Big[\ln x\Big] + \frac{\mathrm{d}}{\mathrm{d}V}\Big[\ln(y-x)\Big] \\ &= \frac{\mathrm{d}}{\mathrm{d}V}\Big[\ln x\Big] + \frac{1}{y-x}\frac{\mathrm{d}}{\mathrm{d}V}\Big[y-x\Big]\end{aligned} \tag{A.13}$$

According to equation (A.7) the derivative of $w_i$ is the charge $q$ times $k_B T$:

$$\frac{\mathrm{d}}{\mathrm{d}V} w_i = \frac{q_i}{k_B T} \tag{A.14}$$

With equation (A.10) the logarithm of $x$ is:

$$\ln x = w_0 + w_1 + \cdots + w_n$$

$$\begin{aligned}\Longrightarrow \quad \frac{\mathrm{d}}{\mathrm{d}V}\Big[\ln x\Big] &= \frac{\mathrm{d}}{\mathrm{d}V}\Big[w_0+w_1+\cdots+w_n\Big] \\ &= \frac{1}{k_B T}\big[q_0+q_1+\cdots+q_n\big] = \frac{q}{k_B T}\end{aligned} \tag{A.15}$$

Equation (A.11) leads to:

$$\begin{aligned}\frac{\mathrm{d}}{\mathrm{d}V}\Big[y-x\Big] &= 0+\frac{\mathrm{d}}{\mathrm{d}V}\Big[e^{w_0}\Big]+\frac{\mathrm{d}}{\mathrm{d}V}\Big[e^{w_0+w_1}\Big]+\cdots+\frac{\mathrm{d}}{\mathrm{d}V}\Big[e^{w_{n-1}}\Big]\\ &= e^{w_0}\frac{\mathrm{d}}{\mathrm{d}V}\Big[w_0\Big]+e^{w_0+w_1}\frac{\mathrm{d}}{\mathrm{d}V}\Big[w_0+w_1\Big]+\cdots\\ &\quad\cdots+e^{w_0+w_1+\cdots+w_{n-1}}\frac{\mathrm{d}}{\mathrm{d}V}\Big[w_0+w_1+\cdots+w_{n-1}\Big]\\ &\underset{(A.14)}{=}\frac{1}{k_BT}\Big[q_0e^{w_0}+(q_0+q_1)\,e^{w_0+w_1}+\cdots\\ &\quad\cdots+(q_0+q_1+\cdots+q_{n-1})\,e^{w_0+w_1+\cdots+w_{n-1}}\Big]\end{aligned}\tag{A.16}$$

Repeating equation (A.13):

$$\begin{aligned}\frac{\mathrm{d}}{\mathrm{d}V}\Big[\ln(y-x)\Big] &= \frac{1}{y-x}\frac{\mathrm{d}}{\mathrm{d}V}\Big[\ln(y-x)\Big]\\ &\underset{(A.16)}{\overset{(A.11)}{=}}\frac{1}{k_BT}\,\frac{q_0\,e^{w_0}+(q_0+q_1)\,e^{q_0+q_1}+\cdots+\sum_{j=0}^{n-1}q_j\exp\sum_{i=0}^{n-1}w_i}{1+e^{w_0}+e^{w_0+w_1}+\cdots+e^{w_0+w_1}+\cdots+e^{w_0+w_1+\cdots+w_{n-1}}}\end{aligned}$$

Together with equations (A.13) and (A.15), the final expression of the derivative of the logarithm of $K$ can be written:

$$\begin{aligned}\frac{\mathrm{d}}{\mathrm{d}V}\Big[\ln K\Big] &= \frac{1}{k_BT}\left[q-\frac{q_0\,e^{w_0}+(q_0+q_1)\,e^{q_0+q_1}+\cdots+\sum_{j=0}^{n-1}q_j\exp\sum_{i=0}^{n-1}w_i}{1+e^{w_0}+e^{w_0+w_1}+\cdots+\exp\sum_{i=0}^{n-1}w_i}\right]\\ &= \frac{1}{k_BT}\left[\frac{q+qe^{w_0}+qe^{w_0+w_1}+\cdots+q\exp\sum_{i=0}^{n-1}w_i+\cdots}{1+e^{w_0}+e^{w_0+w_1}+\cdots+\exp\sum_{i=0}^{n-1}w_i}\cdots\right.\\ &\quad\left.\cdots\,\frac{\cdots-q_0\,e^{w_0}-(q_0+q_1)\,e^{w_0+w_1}-\cdots-\sum_{j=0}^{n-1}q_j\exp\sum_{i=0}^{n-1}w_i}{1+e^{w_0}+e^{w_0+w_1}+\cdots+\exp\sum_{i=0}^{n-1}w_i}\right]=\end{aligned}$$

$$= \frac{1}{k_B T} \left[ \frac{q + (q - q_0) e^{w_0} + (q - q_0 - q_1) e^{w_0 + w_1} + \cdots + q_n \exp \sum_{i=0}^{n-1} w_i}{1 + e^{w_0} + e^{w_0 + w_1} + \cdots + \exp \sum_{i=0}^{n-1} w_i} \right]$$

$$= \frac{q}{k_B T} \left[ \frac{1 + \sum_{i=1}^{n} \frac{q_i}{q} e^{w_0} + \sum_{i=2}^{n} \frac{q_i}{q} e^{w_0 + w_1} + \cdots + \frac{q_n}{q} \exp \sum_{i=0}^{n-1} w_i}{1 + e^{w_0} + e^{w_0 + w_1} + \cdots + \exp \sum_{i=0}^{n-1} w_i} \right]$$

Looking again at very negative potentials ($V \ll \overline{V}$), it can be shown that the logarithmic potential sensitivity reduces to:

$$\frac{\mathrm{d}}{\mathrm{d}V} \Big[ \ln K \Big] = \frac{q}{k_B T}$$

which is the same as in equation (2.5), page 35 in the two–state model.

The strength of this method lies in the fact that it is model independent: independently from the exact states the channel occupies during its transition from the closed to the open state, the logarithmic potential sensitivity as determined in the preceding section is equal to $q/k_B T$. Further details can be found in [116].

# Bibliography


1. A. Galvani. De viribus electricitatis in motu musculari commentarius. *De bononiensi scientarium et atium instituto atque academia Commentarii.*, 7:363–418, 1791.

2. W. Bernardi. The controversy over animal electricity in 18th–century Italy: Galvani, Volta, and others. *Rev. Hist. Sci. Paris*, 54(1):53–70, 2001.

3. A. L. Hodgkin and A. F. Huxley. A quantitative description of membrane current and its application to conduction and excitation in nerve. *J. Physiol.*, 117(4):500–544, 1952.

4. B. L. Tempel, D. M. Papazian, T. L. Schwarz, Y. N. Jan, and L. Y. Jan. Sequence of a probable potassium channel component encoded at *Shaker* locus of *Drosophilia*. *Science*, 237:770–775, 1987.

5. B. Hille. *Ion Channels of Excitable Membranes.* Sinauer Associates, Sunderland, Mass., 3rd edition, July 2001.

6. C. M. Armstrong and F. Bezanilla. Currents related to movement of the gating particles of the sodium channels. *Nature*, 242:459–461, 1973.

7. E. Neher and B. Sakmann. Single–channel currents recorded from membrane of denervated frog muscle fibres. *Nature*, 260(5554):799–802, 1976.

8. W. S. Agnew, A. C. Moore, S. R. Levinson, and M. A. Raftery. Identification of a large molecular weight peptide associated with a tetrodotoxin binding protein from the electroplax of electrophorus electricus. *Biochem. Biophys. Res. Commun.*, 92(3):860–866, 1980.

9. D. A. Beneski and W. A. Catterall. Covalent labeling of protein components of the sodium channel with a photoactivable derivative of scorpion toxin. *Proc. Natl. Acad. Sci. USA*, 77(1):639–643, 1980.

10. M. Noda, T. Ikeda, H. Suzuki, H. Takeshima, T. Takahashi, M. Kuno, and S. Numa. Expression of functional sodium channels from cloned cDNA. *Nature*, 322(6082):826–828, 1986.

11. M. Noda, S. Shimizu, T. Tanabe, T. Takai, T. Kayano, T. Ikeda, H. Takahashi, H. Nakayama, Y. Kanaoka, and N. Minamino. Primary structure of electrophorus electricus sodium channel deduced from cDNA sequence. *Nature*, 312(5990):121–127, 1984.

12. N. Yang, A. L. George Jr., and R. Horn. Molecular basis of charge movement in voltage–gated sodium channels. *Neuron*, 16(1):113–122, 1996.

13. L. M. Mannuzzu, M. M. Maronne, and E. Y. Isacoff. Direct physical measure of conformational rearrangement underlying potassium channel gating. *Science*, 271:213–216, 1996.

14. H. P. Larsson, O. S. Baker, D. S. Dhillon, and E. Y. Isacoff. Transmembrane movement of the *Shaker* $K^+$ channel S4. *Neuron*, 16(2):387–397, 1996.

15. S. B. Long, X. Tao, E. B. Campbell, and R. MacKinnon. Atomic structure of a voltage–dependent $K^+$ channel in a lipid membrane–like environment. *Nature*, 450(7168):376–382, 2007.

16. N. Yang and R. Horn. Evidence for voltage–dependent S4 movement in sodium channels. *Neuron*, 15(1):213–218, 1995.

17. A. Cha and F. Bezanilla. Structural implications of fluorescence quenching in the *Shaker* $K^+$ channel. *J. Gen. Physiol.*, 112(4):391–408, 1998.

18. K. S. Glauner, L. M. Mannuzzu, C. S. Gandhi, and E. Y. Isacoff. Spectroscopic mapping of voltage sensor movement in the *Shaker* potassium channel. *Nature*, 402(6763):813–817, 1999.

19. Y. Jiang, V. Ruta, J. Chen, A. Lee, and R. MacKinnon. The principle of gating charge movement in a voltage–dependent $K^+$ channel. *Nature*, 423:42–48, 2003.

20. V. Ruta, J. Chen, and R. MacKinnon. Calibrated measurement of gating charge arginine displacement in the KvAP voltage–dependent $K^+$ channel. *Cell*, 123:463–475, 2005.

21. D. A. Doyle, J. Morais Cabral, R. A. Pfuetzner, A. Kuo, J. M. Gulbis, S. L. Cohen, B. T. Chait, and R. MacKinnon. The structure of the potassium channel: Molecular basis of $K^+$ conduction and selectivity. *Science*, 280(5360):69–77, 1998.

22. Y. Jiang, A. Lee, J. Chen, V. Ruta, M. Cadene, B. T. Chait, and R. MacKinnon. X–ray structure of a voltage–dependent $K^+$ channel. *Nature*, 423:33–41, 2003.

23. S. B. Long, E. B. Campbell, and R. Mackinnon. Crystal structure of a mammalian voltage–dependent *Shaker* family $K^+$ channel. *Science*, 309:897–903, 2005.

24. F. Tombola, M. M. Pathak, and E. Y. Isacoff. Voltage–sensing arginines in a potassium channel permeate and occlude cation–selective pores. *Neuron*, 45:379–388, 2005.

25. F. Tombola, M. M. Pathak, P. Gorostiza, and E. Y. Isacoff. The twisted ion–permeation pathway of a resting voltage–sensing domain. *Nature*, 445(7127):546–549, 2007.

26. C. A. Ahern and R. Horn. Focused electric field across the voltage sensor of potassium channels. *Neuron*, 48:25–29, 2005.

27. D. J. Posson, P. Ge, C. Miller, F. Bezanilla, and P. R. Selvin. Small vertical movement of a $K^+$ channel voltage sensor measured with luminescence energy transfer. *Nature*, 436:848–851, 2005.

28. B. Chanda, O. K. Asamoah, R. Blunck, B. Roux, and F. Bezanilla. Gating charge displacement in voltage–gated ion channels invloves limited transmembrane movement. *Nature*, 436:852–856, 2005.

29. L. R. Phillips, M. Milescu, Y. Li-Smerin, J. A. Mindell, J. I. Kim, and K. J. Swartz. Voltage–sensor activation with a tarantula toxin as cargo. *Nature*, 436:857–860, 2005.

30. H. C. Lee, J. M. Wang, and K. J. Swartz. Interaction between extracellular Hanatoxin and the resting conformation of the voltage–sensor paddle in Kv channels. *Neuron*, 40:527–536, 2003.

31. A. A. Alabi, M. I. Bahamonde, H. J. Jung, J. Il Kim, and K. J. Swartz. Portability of paddle motif function and pharmacology in voltage sensors. *Nature*, 450:370–375, 2007.

32. C. A. Ahern and R. Horn. Specificity of charge–carrying residues in the voltage sensor of potassium channels. *J. Gen. Physiol.*, 123:205–216, 2004.

33. B. Chanda and F. Bezanilla. A common pathway for charge transport through voltage–sensing domains. *Neuron*, 57:345–351, 2008.

34. C. A. Villalba–Galea, W. Sandtner, D. M. Starace, and F. Bezanilla. S4–based voltage sensors have three major conformations. *Proc. Natl. Acad. Sci. USA*, 105(46):17600–17607, 2008.

35. L. J. DeFelice. Fluctuation analysis in neurobiology. *Int. Rev. Neurobiol.*, pages 169–208, 1977.

36. E. Neher and Charles F. Stevens. Conductance fluctuations and ionic pores in membranes. *Ann. Rev. Biophys. Bioeng.*, 6:345–381, 1977.

37. O. Alvarez, C. Gonzalez, and R. Latorre. Counting channels: A tutorial guide on ion channel fluctuation analysis. *Advances in Physiology Education*, 26(4):327–341, 2002.

38. F. J. Sigworth. The variance of sodium current fluctuations at the node of ranvier. *J. Physiol.*, 307:97–129, 1980.

39. N. E. Schoppa, K. McCormack, M. A. Tanouye, and F. J. Sigworth. The size of gating charge in wild–type and mutant *Shaker* potassium channels. *Science*, 255:1712–1715, 1992.

40. T. Hoshi, W. N. Zagotta, and R. W. Aldrich. Biophysical and molecular mechanisms of *Shaker* potassium channel inactivation. *Science*, 250:533–538, 1990.

41. W. N. Zagotta, T Hoshi, J. Dittman, and R. W. Aldrich. *Shaker* potassium channel gating. II. Transitions in the activation pathway. *J. Gen. Physiol.*, 103:279–319, 1994.

42. F. Noceti, P. Baldelli, X. Wei, N. Qin, L. Toro, L. Birnbaumer, and E. Stefani. Effective gating charges per channel in voltage–dependent $K^+$ and $Ca^{2+}$ channels. *J. Gen. Physiol.*, 108(3):143–155, 1996.

43. S. K. Aggarwal and R. MacKinnon. Contribution of the S4 segment to gating charge in the *Shaker* $K^+$ channel. *Neuron*, 16(6):1169–1177, 1996.

44. L. D. Islas and F. J. Sigworth. Voltage sensitivity and gating charge in *Shaker* and *Shab* family potassium channels. *J. Gen. Physiol.*, 114:723–741, 1999.

45. E. R. Liman, P. Hess, F. Weaver, and G. Koren. Voltage–sensing residues in the S4 region of a mammalian $K^+$ channel. *Nature*, 353:752–756, 1991.

46. F. Conti and W. Stühmer. Quantal charge redistributions accompanying the structural transitions of sodium channels. *Eur. Biophys. J.*, 17(2):53–59, 1989.

47. B. Hirschberg, A. Rovner, M. Lieberman, and J. Patlak. Transfer of twelve charges is needed to open skeletal muscle $Na^+$ channels. *J. Gen. Physiol.*, 106:1053–1068, 1995.

48. M. F. Sheets and D. A. Hanck. Charge immobilization of the voltage sensor in domain IV is independent of sodium current inactivation. *J. Physiol.*, 563:83–93, 2005.

49. A. Kuzmenkin, F. Bezanilla, and A. M. Correa. Gating of the bacterial sodium channel, NaChBac: Voltage–dependent charge movement and gating currents. *J. Gen. Physiol.*, 124:349–356, 2004.

50. R. F. Clark, S. R. Williams, S. P. Nordt, and A. S. Manoguerra. A review of selected seafood poisonings. *Undersea Hyper. Med.*, 26(3):175–184, 1999.

51. W. M. Bonner. Protein migration into nuclei. I. Frog oocyte nuclei in vivo accumulate microinjected histones, allow entry to small proteins, and exclude large proteins. *J. Cell. Biol.*, 64(2):421–430, 1975.

52. W. M. Bonner. Protein migration into nuclei. II. Frog oocyte nuclei accumulate a class of microinjected oocyte nuclear proteins and exclude a class of microinjected oocyte cytoplasmic proteins. *J. Cell. Biol.*, 64(2):431–437, 1975.

53. S. F. Gilbert. *Developmental Biology.* Sinauer Associates, Sunderland, Mass., 8th ed edition, 2006.

54. M. F. Romero, Y. Kanai, H. Gunshin, and M. A. Hediger. Expression cloning using *Xenopus laevis* oocytes. In S. G. Amara, editor, *Methods in Enzymology*, volume 296, pages 17–52. Academic Press, San Diego, CA, 1998.

55. J. B. Gurdon, C. D. Lane, H. R. Woodland, and G. Marbaix. Use of frog eggs and oocytes for the study of messenger rna and its translation in living cells. *Nature*, 233:177–182, 1971.

56. C. A. Wagner, J. Friedrich, I. Setiawan, F. Lang, and S. Bröer. The use of *Xenopus laevis* oocytes for the functional characterization of heterologously expressed membrane proteins. *Cell. Physiol. Biochem.*, 10:1–12, 2000.

57. T. W. Schultz and D. A. Dawson. Housing and husbandry of *Xenopus* for oocyte production. *Lab Animal*, 32(2):34–39, 2003.

58. J. N. Dumont. Oogenesis in *Xenopus laevis* (Daudin) I. Stages of oocyte development in laboratory maintained animals. *J. Morph.*, 136:153–180, 1972.

59. W. Baumgartner, L. Islas, and F. J. Sigworth. Two–microelectrode voltage clamp of *Xenopus* oocytes: Voltage errors and compensation for local current flow. *Biophys. J.*, 77:1980–1991, 1999.

60. J. R. Lakowicz. *Principles of Fluorescence Spectroscopy.* Springer, New York, 3rd edition, 2006.

61. G. G. Stokes. On the change of refrangibility of light. *Phil. Trans. R. Soc. (London)*, 142:463–562, 1852.

62. O. Shimomura, F. H. Johnson, and Y. Saiga. Extraction, purification and properties of aequorin, a bioluminescent protein from the luminous hydromedusan, *Aequorea*. *J. Cell. Comp. Physiol.*, 59:223–239, 1962.

63. F. H. Johnson, O. Shimomura, and Y. Saiga. Quantum efficiency of *Cypridina* luminescence, with a note on that of *Aequorea*. *J. Cell. Comp. Physiol.*, 60:85–103, 1962.

64. H. Morise, O. Shimomura, F. H. Johnson, and J. Winant. Intermolecular energy transfer in the bioluminescent system of *Aequorea*. *Biochemistry*, 13(12):2656–2662, 1974.

65. F. G. Prendergast and K. G. Mann. Chemical and physical properties of aequorin and the green fluorescent protein isolated from *Aequorea forskalea*. *Biochemistry*, 17(17):3448–3453, 1978.

66. D. C. Prasher, V. K. Eckenrode, W. W. Ward, F. G. Prendergast, and M. J. Cormier. Primary structure of the *Aequorea victoria* green–fluorescent protein. *Gene*, 111(2):229–233, 1992.

67. S. Inouye and F. I. Tsuji. *Aequorea* green fluorescent protein. Expression of the gene and fluorescence characteristics of the recombinant protein. *FEBS Lett.*, 341(2-3):277–280, 1994.

68. M. Chalfie, Y. Tu, G. Euskirchen, W. W. Ward, and D. C. Prasher. Green fluorescent protein as a marker for gene expression. *Science*, 263(5148):802–805, 1994.

69. W. Arber, D. Nathans, and H. O. Smith.
Nobel prize in medicine or physiology 1970: for the discovery of restriction enzymes and their application to problems of molecular genetics. Website: `http://nobelprize.org/nobel_prizes/medicine/laureates/1978/index.html`.

70. S. N. Cohen, A. C. Chang, H. W. Boyer, and R. B. Helling. Construction of biologically functional bacterial plasmids in vitro. *Proc. Natl. Acad. Sci. USA*, 70(11):3240–3244, 1973.

71. R. Heim, D. C. Prasher, and R. Y. Tsien. Wavelength mutations and posttranslational autoxidation of green fluorescent protein. *Proc. Natl. Acad. Sci. USA*, 91(26):12501–12504, 1994.

72. G. H. Patterson, S. M. Knobel, W. D. Sharif, S. R. Kain, and D. W. Piston. Use of the green fluorescent protein and its mutants in quantitative fluorescence microscopy. *Biophys. J.*, 73(5):2782–2790, 1997.

73. R. Y. Tsien. The green fluorescent protein. *Annu. Rev. Biochem.*, 67:509–544, 1998.

74. R. Heim, A. B. Cubitt, and R. Y. Tsien. Improved green fluorescence. *Nature*, 373(6516):663–664, 1995.

75. T. T. Yang, L. Cheng, and S. R. Kain. Optimized codon usage and chromophore mutations provide enhanced sensitivity with the green fluorescent protein. *Nucleic Acids Res.*, 24(22):4592–4593, 1996.

76. R. B. Robey, O. Ruiz, A. V. Santos, J. Ma, F. Kear, L. J. Wang, C. J. Li, A. A. Bernardo, and J. A. Arruda. pH–dependent fluorescence of a heterologously expressed *Aequorea* green fluorescent protein mutant: In situ spectral characteristics and applicability to intracellular pH estimation. *Biochemistry*, 37(28):9894–9901, 1998.

77. M. Kneen, J. Farinas, Y. Li, and A. S. Verkman. Green fluorescent protein as a noninvasive intracellular pH indicator. *Biophys. J.*, 74(3):1591–1599, 1998.

78. N. Klonis, O. Zan, K. Jackson, D. Goldberg, M. Klemba, and L. Tilley. Evaluation of pH during endocytosis and vacuolar catabolism of haemoglobin in *Plasmodium falciparum*. *Biochem. J.*, 407:343–354, 2007.

79. J. D. Pedelacq, S. Cabantous, T. Tran, T. C. Terwilliger, and G. S. Waldo. Engineering and characterization of a superfolder green fluorescent protein. PDB ID: 2b3q. *Nature Biotechnol.*, 24(1):79–88, 2006.

80. L. A. Deschenes and D. A. Vanden Bout. Single molecule photobleaching: increasing photo yield and survival time through suppression of two–step photolysis. *Chem. Phys. Lett.*, 365:387–395, 2002.

81. G. Donnert, C. Eggeling, and S. W. Hell. Major signal increase in fluorescence microscopy through dark–state relaxation. *Nature Methods*, 4(1):81–86, 2007.

82. C. Eggeling, J. Widengren, L. Brand, J. Schaffer, S. Felekyan, and C. A. M. Seidel. Analysis of photobleaching in single–molecule multicolor excitation and Förster resonance energy transfer measurements. *J. Phys. Chem. A.*, 110(9):2979–2995, 2006.

83. E. K. L. Yeow, S. M. Melnikov, T. D. M. Bell, F. C. De Schryver, and J. Hofkens. Characterizing the fluorescence intermittency and photobleaching kinetics of dye molecules immobilized on a glass surface. *J. Phys. Chem. A.*, 110(5):1726–1734, 2006.

84. P. P. Mondal. Minimizing photobleaching in fluorescence microscopy by depleting triplet states. *App. Phys. Lett.*, 92(1):id 013902 (3 pages), 2008.

85. J. Lippincott–Schwartz, N. Altan-Bonnet, and G. H. Patterson. Photobleaching and photoactivation: following protein dynamics in living cells. *Nature Cell Biol.*, Suppl.:S7–14, 2003.

86. J. White and E. Stelzer. Photobleaching GFP reveals protein dynamics inside live cells. *Trends Cell Biol.*, 9(2):61–65, 1999.

87. R. Swaminathan, C. P. Hoang, and A. S. Verkman. Photobleaching recovery and anisotropy decay of green fluorescent protein GFP–S65T in solution and cells: Cytoplasmic viscosity probed by green fluorescent protein translational and rotational diffusion. *Biophys. J.*, 72(4):1900–1907, 1997.

88. A. Jimenez–Banzo, S. Nonell, J. Hofkens, and C. Flors. Singlet oxygen photosensitization by EGFP and its chromophore HBDI. *Biophys. J.*, 94(1):168–172, 2008.

89. R. Dixit and R. Cyr. Cell damage and reactive oxygen species production induced by fluorescence microscopy: Effect on mitosis and guidelines for non–invasive fluorescence microscopy. *Plant J.*, 36(2):280–290, 2003.

90. B. Halliwell and J. M. C. Gutteridge. *Free Radicals in Biology and Medicine.* Oxford University Press, Oxford, 4th ed. edition, 2007.

91. M. Ormö, A. B. Cubitt, K. Kallio, L. A. Gross, R. Y. Tsien, and S. J. Remington. Crystal structure of the aequorea victoria green fluorescent protein. *Science*, 273(5280):1392–1395, 1996.

92. F. Yang, L. G. Moss, and G. N. Phillips. The molecular structure of green fluorescent protein. *Nature Biotechnol.*, 14(10):1246–1251, 1996.

93. R. MacKinnon. Determination of the subunit stoichiometry of a voltage–activated potassium channel. *Nature*, 350:232–235, 1991.

94. J. M. Zwier, G. J. Van Rooij, J. W. Hofstraat, and G. J. Brakenhoff. Image calibration in fluorescence microscopy. *J. Microsc.*, 216(Pt 1):15–24, 2004.

95. J. M. Zwier, L. Oomen, L. Brocks, K. Jalink, and G. J. Brakenhoff. Quantitative image correction and calibration for confocal fluorescence microscopy using thin reference layers and SIPchart–based calibration procedures. *J. Microscopy*, 231(1):59–69, 2008.

96. M. S. Siegel and E. Y. Isacoff. A genetically encoded optical probe of membrane voltage. *Neuron*, 19(4):735–741, 1997.

97. G. Guerrero, M. S. Siegel, B. Roska, E. Loots, and E. Y. Isacoff. Tuning FlaSh: Redesign of the dynamics, voltage range, and color of the genetically encoded optical sensor of membrane potential. *Biophys. J.*, 83(6):3607–3618, 2002.

98. A. L. Goldin. Mechanisms of sodium channel inactivation. *Curr. Opin. Neurobiol.*, 13(3):284–290, 2003.

99. G. S. Harms, L. Cognet, P. H. Lommerse, G. A. Blab, and T. Schmidt. Autofluorescent proteins in single–molecule research: Applications to live cell imaging microscopy. *Biophys. J.*, 80(5):2396–2408, 2001.

100. T. M. Gamal El–Din, D. Grögler, C. Lehmann, H. Heldstab, and N. G. Greeff. More gating charges are needed to open a *Shaker* $K^+$ channel than are needed to open a rBIIA $Na^+$ channel. *Biophys. J.*, 95(3):1165–1175, 2008.

101. D. B. Murphy. *Fundamentals of light microscopy and electronic imaging*. Wiley–Liss, New York, 2001.

102. M. Minsky. Microscopy Apparatus. U.S. patent 301467, 1961.

103. M. Göppert–Mayer. Über Elementarakte mit zwei Quantensprüngen. *Annalen der Physik*, 401(3):273–294, 1931.

104. W. Kaiser and C. G. B. Garrett. Two–photon excitation in $CaF_2$: $Eu^{2+}$. *Phys. Rev. Lett.*, 7(6):229–231, 1961.

105. W. Denk, J. H. Strickler, and W. W. Webb. Two–photon laser scanning fluorescence microscopy. *Science*, 248(4951):73–76, 1990.

106. W. Denk, J. P. Strickler, and W. W. Webb. Two–Photon Laser Scanning Microscopy. International patent publication number WO9107651 (A1), 1991.

107. H. Ewers, A. E. Smith, I. F. Sbalzarini, H. Lilie, P. Koumoutsakos, and A. Helenius. Single–particle tracking of murine polyoma virus–like particles on live cells and artificial membranes. *Proc. Natl. Acad. Sci. USA*, 102(42):15110–15115, 2005.

108. G. E. Snyder, T. Sakamoto, J. A. Hammer 3rd, J. R. Sellers, and P. R. Selvin. Nanometer localization of single green fluorescent proteins: Evidence that myosin V walks hand–over–hand via telemark configuration. *Biophys. J.*, 87(3):1776–1783, 2004.

109. E. E. Hall. The penetration of totally reflected light into the rarer medium. *Phys. Rev. (Series I)*, 15(2):73–106, 1902.

110. A. L. Stout and D. Axelrod. Evanescent field excitation of fluorescence by epi–illumination microscopy. *Applied Optics*, 28(24):5237–5242, 1989.

111. E. H. Synge. A suggested method for extending the microscopic resolution into the ultramicroscopic region. *Phil. Mag.*, 6:356–362, 1928.

112. D. W. Pohl, W. Denk, and M. Lanz. Optical stethoscopy: Image recording with resolution $\lambda/20$. *App. Phys. Lett.*, 44(7):651–653, 1984.

113. A. Lewis, M. Isaacson, A. Harootunian, and A. Muray. Development of a 500 Å spatial resolution light microscope: I. light is efficiently transmitted through $\lambda/16$ diameter apertures. *Ultramicroscopy*, 13(3):227–231, 1984.

114. B. E. A. Saleh and M. C. Teich. *Fundamentals of Photonics.* John Wiley & Sons, New York, 1991.

115. J. B. Pawley, editor. *Handbook of Biological Confocal Microscopy.* Plenum Press, New York, 1990.

116. W. Almers. Gating currents and charge movements in excitatory membranes. *Rev. Physiol. Biochem. Pharmac.*, 82:96–190, 1978.

# Physical constants & abbreviations

| | | | |
|---|---|---|---|
| Avogadro's Number | $N_A$ | = | $6.0221 \times 10^{23}\,\mathrm{mol}^{-1}$ |
| Elementary charge | $e$ | = | $1.6022 \times 10^{-19}\,\mathrm{C}$ |
| Boltzmann's constant | $k_B$ | = | $1.3807 \times 10^{-23}\,\mathrm{JK}^{-1}$ |
| Gas constant | $R$ | = | $8.3145\,\mathrm{Jmol}^{-1}\mathrm{K}^{-1}$ |

| | |
|---|---|
| $T$ | Absolute temperature |
| $I_g$ | Gating current of channel populations |
| $i_g$ | Gating current of a single ion channel |
| $Q_g$ | Gating charge of channel populations |
| $q_g$ | Gating charge of a single ion channel |
| $V_{eq}$ | Membrane potential difference in the resting state |
| DI–DIV | The four domains of the $Na^+$ channel |
| S1–S6 | $\alpha$–helical segments of $K^+$ and $Na^+$ channels |
| R1–R7 | Arginines on the voltage sensor S4 |
| TEVC | Two electrode voltage clamp |

Für die großzügige Unterstützung, welche mir während der letzten Jahre in Bezug auf diese Arbeit zuteil wurde, möchte ich mich bei den folgenden Personen bedanken:

Conrad Escher

Hans–Werner Fink

Tamer Gamal El–Din

Klaus Greeff

Sophie Hengl

Hanspeter Meyer

Peter Robmann